DEFORMABLE MEDIA FOR VISUAL AND TACTILE INTERFACES

A Dissertation

Presented to the Faculty of the Graduate School

of Cornell University

in Partial Fulfillment of the Requirements for the Degree of

Doctor of Philosophy

by

Chris Larson

May 2017

DEFORMABLE MEDIA FOR VISUAL AND TACTILE INTERFACES

Chris Larson, Ph.D.

Cornell University 2017

We experience a variety of natural touch surfaces in our daily lives. These surfaces range in compliance from hard to soft, and in texture from smooth to rough. Human computer interfaces, on the other hand, have largely been of the rigid type; surfaces that don't deform under the forces of touch. In the last 15 years, we have experienced technological paradigm shifts (e.g., VR, wearable computing) that have introduced a need for a more capable physical interface. Soft computer interfaces offer another dimension to touch interaction, and a medium with which to create better abstractions of natural surfaces. This dissertation explores the use of soft membranes as a medium for human computer interaction. Specifically, I address three questions: (i) how do we incorporate visual display into a soft haptic interface, (ii) how do we recognize human touch in a deforming medium, and (iii) how ought we quantify information in a deforming medium? I address these questions through three threads. First, I present stretchable displays, based on hyperelastic light-emitting capacitors (HLEC's), that can be embedded in an elastomer to actively display information under large deformations. The HLEC system stretches to >500 percent strain in uniaxial tension, which as of this writing, exceeds other systems by >4X. Secondly, I present OrbTouch, a soft touch interface that interprets human touch. This system uses embedded arrays of capacitance sensors in combination with a convolutional neural network-based signal processing layer to learn touch patterns from human users. Finally, I provide information theoretic arguments that

relate information produced in capacitance signals to the underlying deformations that cause them.

BIOGRAPHICAL SKETCH

Chris Larson was on October 2nd, 1983 in Iowa City, Iowa. Prior to attending Cornell, Chris received his B.A. in Physics from Coe College in 2006, and his M.S. in Materials Science from the University of Missouri-Rolla in 2008. He went on to work at NASA Kennedy Space Center supporting both the Constellation and Space Shuttle programs, where he supported several International Space Station missions, including STS-119, 127, 128, 129, 130, 131, and 133, as well as the Hubble Space Telescope repair mission STS-125. Following the Space Shuttle Program, he spent two years working at Corning Incorporated, where he led project teams in the development of predictive failure models for glass products and manufacturing equipment. He entered his PhD program at Cornell in August 2013, completing his qualifying exam in January, 2014, and receiving his M.S. in Mechanical Engineering in December, 2015.

ACKNOWLEDGEMENTS

I thank my PhD advisor, Professor Rob Shepherd, for his technical guidance, inspiration, and endless creativity. He gave me an optimal balance of direction and freedom during my doctoral work, which allowed me to thrive intellectually and academically. I also thank my two committee members, Professor Ross Knepper, a roboticist from the Computer Science department at Cornell, and Professor Meredith Silberstein, a mechanician from the Mechanical Engineering department at Cornell, for their domain expertise in the topics that comprise this thesis.

I also thank my group members for their support and encouragement throughout my time at Cornell. I will miss the free exchange of ideas, intellectual banter, and camaraderie that we developed over the last four years. My group members include Bryan Peele, Simon Dunham, Shuo Li, Ben MacMurray, Ilse van Meerbeek, Kevin O'Brien, James Pikul, Sanlin Robinson, and Thomas Wallin. Additionally, I would like to thank Justin Choi, Wanying Li, Kevin Kruemplestaedter, Gabe Pesco, and Max Westwater for their assistance with computer aided design and lab experiments.

I am also grateful to the professors here at Cornell who have given me formal instruction; the ideas and concepts that comprise this thesis, without exception, originated from class discussions and course projects. To that end, I sincerely thank my advisor Rob Shepherd, Nicholas Zabaras, formerly of Theoretical and Applied Mechanics, and Killian Weinberger and Bart Selman, both from Computer Science.

Most importantly, I thank my wife, Caroline Walker Larson, for her endless love, support, and encouragement. She has inspired and motivated me in so many ways; I am forever grateful that our paths happened to cross back in

2009. Additionally, I thank mother Mary, sister Margaret, and father Warren for being so supportive throughout my life, #*bestfamilyever*! Although my father has passed, his spirit continues to guide me. Finally, I thank my previous graduate advisor, Professor Richard Brow, and undergraduate advisor, Professor Steve Feller, for their advice, guidance, and unwavering support earlier in my life.

CONTENTS

LIST OF TABLES

LIST OF FIGURES

CHAPTER 1

INTRODUCTION

We experience a variety of natural touch surfaces in our daily lives. These surfaces range in compliance from hard to soft, and in texture from smooth to rough. Human computer interfaces, on the other hand, have largely been of the rigid type; surfaces that don't deform under the forces of touch. In the last 15 years, we have experienced two technological paradigm shifts that have introduced a need for a more capable physical interface. First, we have undergone a transition from desktop computers to pocket-sized ones; the next generation of devices will be of the wearable type; ones that fit on the body. Wearable technology introduces a need for electronic devices that can deform as the body moves. Secondly, the trend towards virtual reality as an interactive gaming solution, and augmented reality as a mobile computing solution, has further introduced a need for non-visual, haptic feedback that provides a level of physical immersion not offered by current systems (which rely on vibration as a feedback mechanism). Shape changing human computer interfaces are of interest to both of these technological trends, as they offer another dimension to touch interaction, and a route to create better abstractions of natural surfaces.

Recent advances in the field of soft robotics offer strategies to achieve shape changing surfaces. These devices use pneumatically powered elastomers with internal fluidic circuitry [1, 2, 3]. This dissertation explores the use of these inflatable membranes as a medium for human computer interaction. Specifically, I address three questions: (i) how do we incorporate visual display into a soft haptic interface, (ii) how do we recognize human touch in a deforming medium, and (iii) how ought we quantify information in a deforming medium? I address these questions through two threads: (i) stretchable displays, based on hypere-

lastic light-emitting capacitors, that can be embedded in an elastomer to actively display information under large deformations, and (ii) OrbTouch, a deformable touch surface that provides an interactive touch medium. The primary contributions of this work are, first, a visual display that stretches to >500% strain, which as of this writing, exceeds other systems by >4X. This interface triples as a sensor, display, and actuator. Secondly, I introduce a learning-based signal processing layer for stretchable sensors. I demonstrate this with OrbTouch, and highlight its ability to learn user-specific touches. Finally, I provide information theoretic arguments that explain how information is encoded in deformation. Given that a stretchable membrane can occupy a continuum of deformed states, it follows that there are as many information states. If one has full knowledge of its shape, and a means to encode shape, then deformation potentially provides an information-rich medium for communication. The factors that would enable such a system are the ability to embed arrays of sensors into the membrane at relevant resolutions, and the ability to efficiency encode shape; this dissertation addresses both questions.

1.1 Related Work

My research draws from several fields including solid mechanics, stretchable electronics, materials science, soft materials fabrication, soft robotics, wearable devices and sensors, information theory, machine learning, and human computer interaction. Here I summarize the pieces that were most central to my research direction.

1.1.1 Deformable Interfaces

Shape changing surfaces add another dimension to touch interaction. The systems that have been developed to date vary widely in design, mechanism, and capability. At one extreme, there are rigid mechanical devices with integrated software that enable shape modulation and compliance (both passive and active). inFORM [4] does this using a 2D array of linearly actuating pins in combination with a top-down projector to produce dynamic surfaces with visual and physical texture in three dimensions (Fig. 1.1). It utilizes dynamic physical affordances and constraints, in addition to being able to actuate objects on its surface. TableHop [5] is a conceptually similar system that replaces discrete pins with a conductive fabric touch medium (Fig 1.2.). It uses a upward facing projector to cast images onto the touch surface (thereby eliminating screen occlusion), which has embedded dielectric elastomer actuators that provide haptic feedback. This system does not actively modulate its shape.

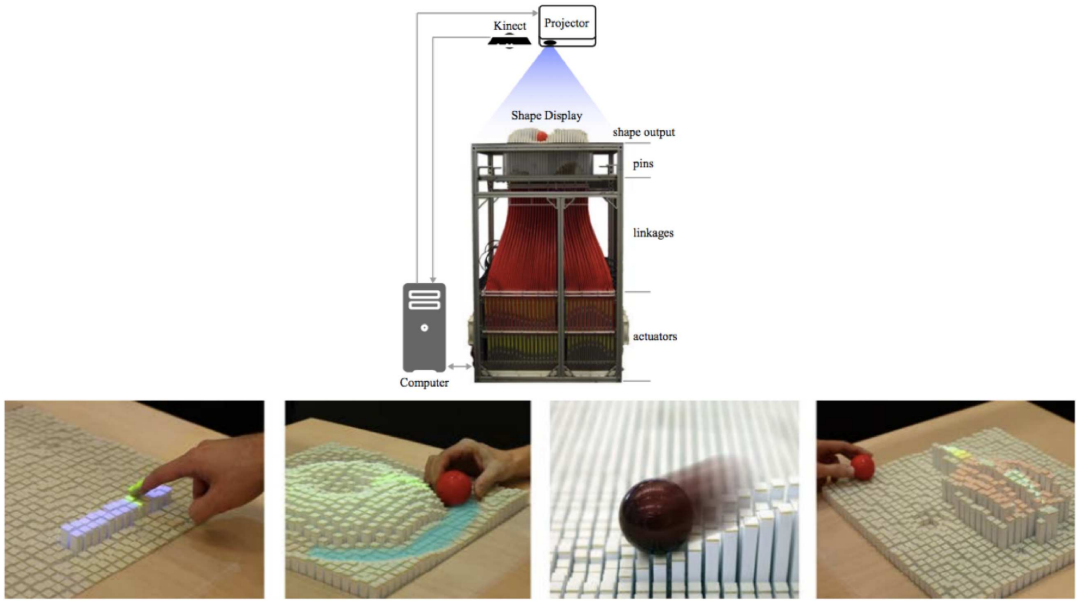

Figure 1.1: **inFORM, by Follmer and Leithinger.** Adapted from [4].

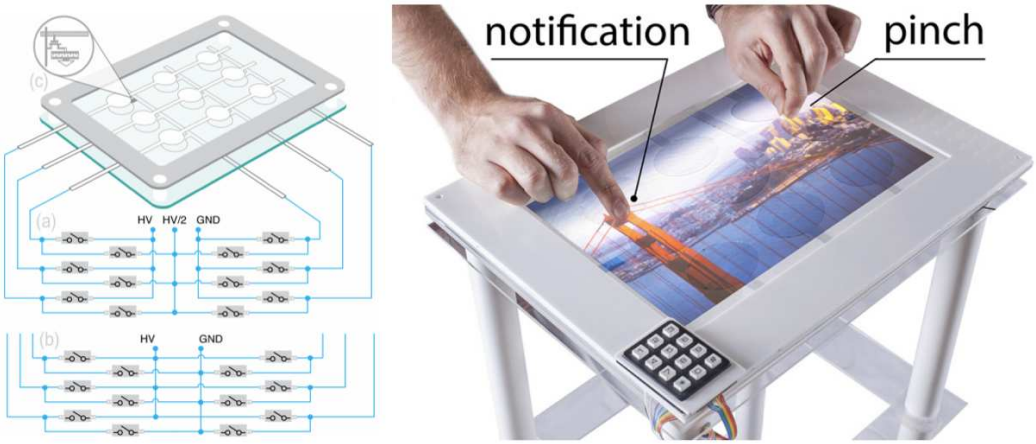

Figure 1.2: **TableHop, by Sahoo.** Adapted from [5].

A different approach to shape changing interfaces is the use of soft components that can both passively deform under human touch [6, 7], as well as actively deform through pneumatic actuation. Figure 1.3 shows the primary differences between interaction with deformable and inflatable surfaces. Although an inflatable touch surface does not modulate shape with the same level of complexity as inFORM, elastomer-based surfaces are conceptually simple, compatible with a variety of sensing modalities, and in general are a more consumer-friendly technology on the basis cost, size, power consumption, portability, and complexity.

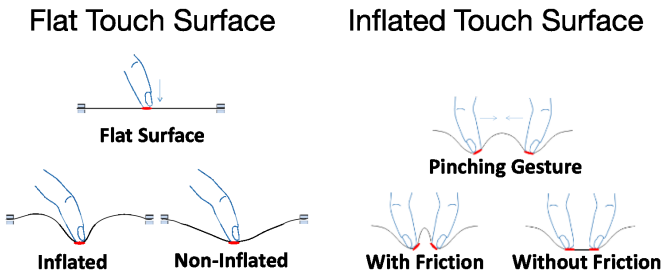

Figure 1.3: **Soft surface interaction modes.** Adapted from [8].

An important area of research in recent years has combined visual displays with soft interfaces. Harrison [8] was the first to demonstrate this by overlaying translucent elastomer actuators onto a perforated acrylic sheet and back-projecting images onto the membrane to display information. Figure 1.2 shows an example of this system. The device can be fabricated using a simple lamination process. The disadvantages of this system are that it uses a projector, which is not portable; however, integration of a display system into the membrane would enable this system to be portable.

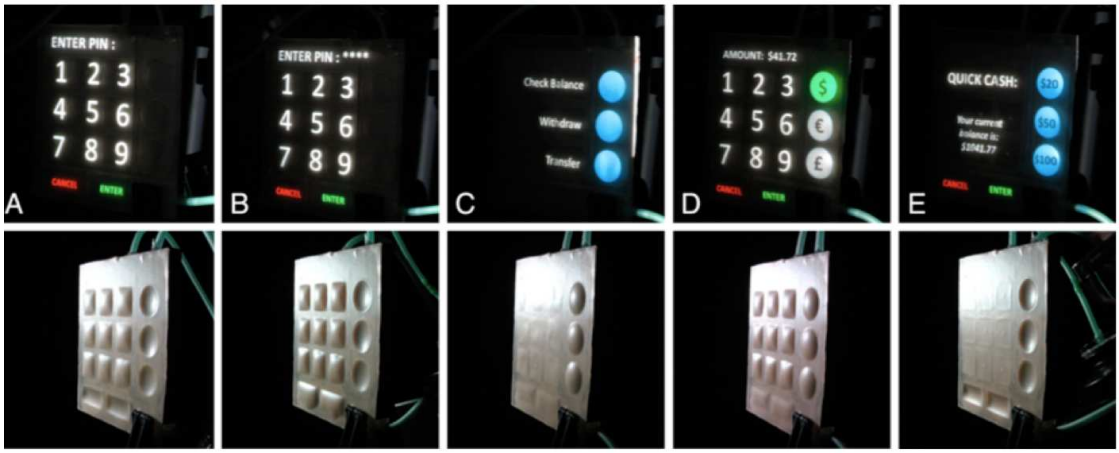

Figure 1.4: **Soft tactile display by Harrison [9].**

Yao et al. [9] has used optical waveguides to achieve a similar functional result; their system was a coupled actuator-display. Figure 2.3 shows the device; optical fibers are oriented normal to the translucent touch surface to project light through it. Interestingly, deformations in these fibers reduce optical transmission through Snell's law; this has been harnessed to create embedded curvature sensors that can be used to sense touch [10].

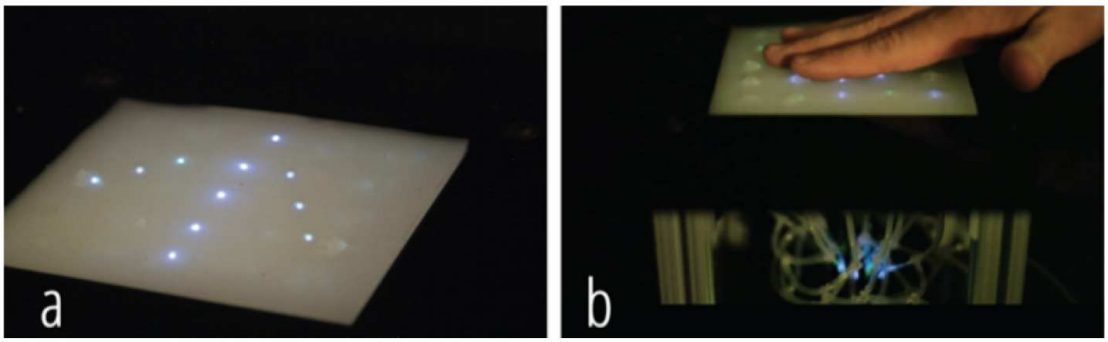

Figure 1.5: **optiElastic by Yao.** Adapted from Yao [10].

Collectively, the body of work comprising this area of research highlights a general need for an embedded sensing capability, as well as an integrated sensor-display system. Arrays of stretchable sensors and light emitting elements, embedded in the touch surface, are appropriate for this application because they offer (i) a route to shape changing displays, (ii) a route to portability, and (iii) sensing that captures non-uniform deformations over the touch surface. The drawback of using stretchable sensors, though, is that they are not commercially available, they require sophisticated fabrication methods, and they are prone to higher levels of noise (and in some cases hysteresis) than traditional off-the-shelf sensors. I expound on the opportunities and challenges related to this in the following section.

1.1.2 Stretchable Electronics and Displays

To integrate sensing and light-emission into a touch interface, I turn to the field of stretchable electronics. Our choice of material system is informed by two requirements: (i) charge conduction at high strains, and (ii) translucent conductors. Touch displays require the combination of these attributes, whereas

stretchable sensors require only conduction at high strains.

Previous displays, based on elastomeric polymer light-emitting devices (EPLEDs), have demonstrated strains of 120% prior to failure [11]. Figure 1.6 shows the design and performance of the EPLED system. This system uses composite electrodes based on percolated networks of Ag-nanowires in a rubbery poly (urethane acrylate) matrix. The electrodes form PIN junctions with a sandwiched electroluminescent layer that consists of a blend of SuperYellow, ethoxylated trimethylolpropanetriacrylate, polyethylene oxide, and lithium trifluoromethane sulphonate. Although the EPLED system exhibits a level of compliance that is suitable for stretchable display applications, it is not adequate for soft actuators, which commonly undergo areal strains of >600% [12].

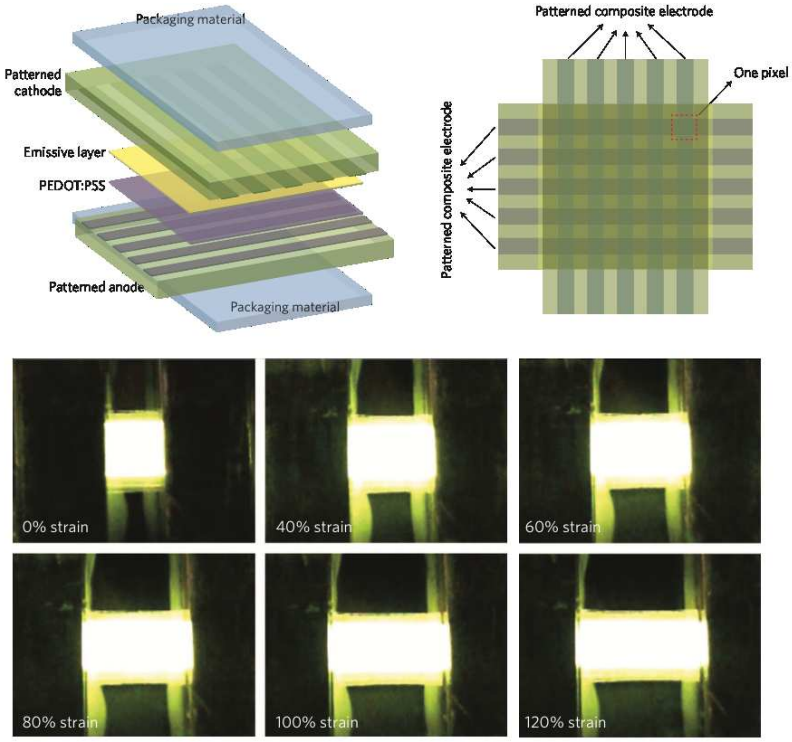

Figure 1.6: **Elastomeric Polymer Light-Emitting Device (EPLED).** Adapted from [12].

For sensing and display applications, ionic hydrogels have several attractive properties including high ultimate strain (Fig. 1.7a) [13] and high transparency (Fig. 1.7b) [14]. They are also used extensively in dielectric elastomer actuators (DEA's) and as dielectric elastomer sensors (DES's). Figure 1.7c shows the DEA/DES architecture, which typically consists of two ionic hydrogel electrodes that sandwich an elastomer dielectric layer.

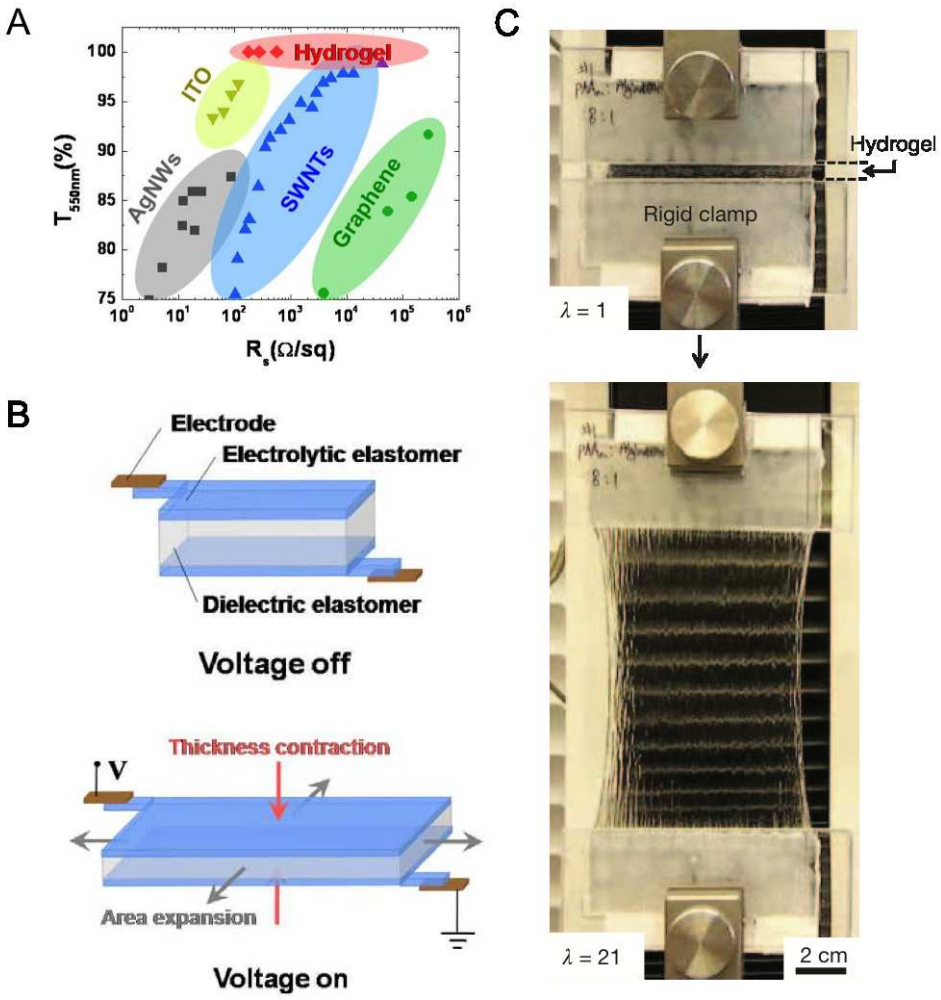

Figure 1.7: **Ionic Hydrogels.** (A) Acrylamide-alginate cogels exhibit extreme ultimate strain and toughness. Adapted from [14]. (B) Dielectric elastomer actuator (DEA) design. Adapted from [15]. (C) Plot of optical transmittance versus resistivity of several stretchable conductors. Adapted from [15].

One disadvantage of hydrogels is that they are incompatible with light emitters that are used in LEDs, such as the one shown in Figure 1.6. High-field electroluminescence (ACEL), however, uses transition metal-doped ZnS phosphor powder under an AC-electric field for emission, and thus is compatible with a ionically conducting electrode. While LEDs offer high brightness, efficiency, and low power consumption, ACEL-based light emission is driven by an electric field, and thus is well suited for integration with dielectric sensors because they can be embedded directly in the dielectric layer and driven electrically in the same way as a DEA.

Another electrode material that is well suited for DESs is multi-walled carbon nanotube (MWCNT) and single-walled carbon nanotube (SWCNT) films [15]. These systems, while not as stretchable as hydrogels, offer mixed mode electronic conduction, thermodynamic stability, and can be patterned easily using solution based processing in combination with aerosol spray deposition. Figure 1.8 shows as example of a stretchable SWCNT film that is both conductive and optically translucent.

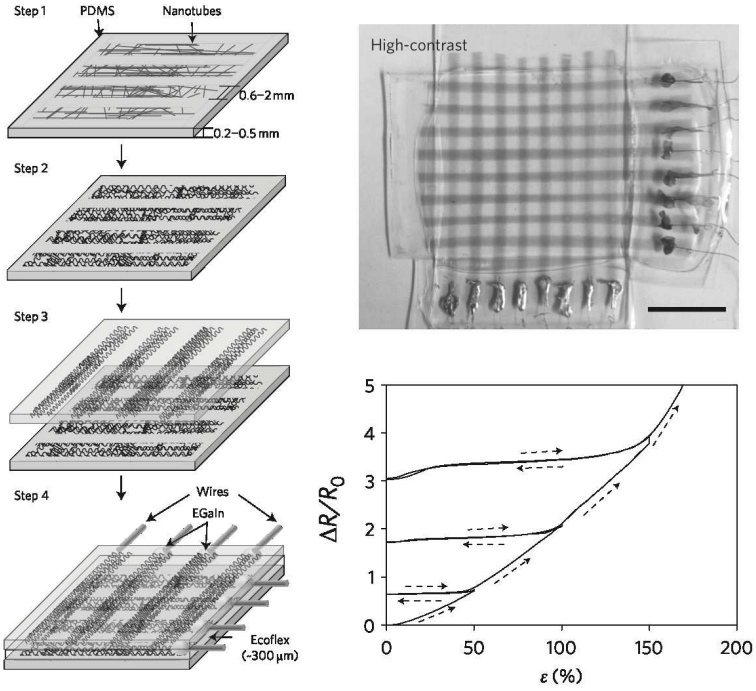

Figure 1.8: **Stretchable, Transparent CNT Capacitance Sensors.** Adapted from [16].

1.2 Scope and Organization

This dissertation is comprised of three independent journal articles: (i) Chapter 2 presents the HLEC system, discussing its design, fabrication, and applications, (ii) Chapter 3 focuses on the application of the HLEC for the popular game Simon, covering the system design, gameplay, and sensing characteristics, and (iii) Chapter 4 presents OrbTouch, a device the learns human inputs through deformation from labelled examples using convolutional neural networks.

In addition to the main text, two related journal articles are provided in the appendices. Appendix A covers a new fabrication method, based on photopatterning and transfer printing, that offers a potential route to pattern a higher resolution, multicolor version of the HLEC system presented in Chapter 2. Ap-

pendix B presents a dielectric elastomer sensor that has a similar construction to the HLEC (but without electroluminescent phosphors in its dielectric layer); this system was used as a touch sensor and provided a foundation for my later work.

REFERENCES

[1] Ilievski F. Choi W. Morin S. A. Stokes A. A. Mazzeo A. D. Whitesides G. M. Shepherd, R. F. Multigait soft robot. *Proceedings of the National Academy of Sciences*, 108(51):20400–20403, 2011.

[2] Gwilliam J. Okamura A. Stanley, A. A deformable geometry, variable stiffness tactile display using pneumatics and particle jamming. *IEEE World Haptics Conference*, 2013.

[3] Chen T. Hoskinson R. Fels S. Vogt, F. A malleable surface touch interface. *ACM SIGGRAPH Sketches*, page 36, 2004.

[4] Leithinger D. Olwal A. Hogge A. Ishii H. Follmer, S. inform: Dynamic physical affordances and constraints through shape and object actuation. *ACM UIST*, 13:417–426, 2013.

[5] Hornbæk K. Subramanian S. Sahoo, D. R. *ACM CHI*, pages 3767–3780, 2016.

[6] Sinclair M. Benko H. Bacim, F. Understanding touch selection accuracy on flat and hemispherical deformable surfaces. *Proceedings of Graphics Interface*, pages 197–204, 2013.

[7] Pedersen E. W. Hornbæk K. Troiano, G. M. User-defined gestures for elastic, deformable displays. *Proc. for International Working Conference on Advanced Visual Interfaces*, pages 2–8, 2014.

[8] Hudson S. E. Harrison, C. Providing dynamically changeable physical buttons on a visual display. *Proceedings of the SIGCHI Conference on Human Factors in Computing Systems*, pages 299–308, 2009.

[9] Ou J. Tauber D. Ishii H. Yao, L. Integrating optical waveguides for display and sensing on pneumatic soft shape changing interfaces. *Proceedings of the adjunct publication of the 27th annual ACM symposium on User interface software and technology*, pages 117–118, 2014.

[10] O'Brien K. Li S. Shepherd R. F. Zhao, H. Optoelectronically innervated soft prosthetic hand via stretchable optical waveguides. *Science Robotics*, 1(1), 2016.

[11] Li L. Niu X. Yu Z. Pei Q. Liang, J. Elastomeric polymer light-emitting devices and displays. *Nature Photonics*, 7(10):817–824, 2013.

[12] Peele B. Li S. Robinson S. Totaro M. Beccai L. Mazolai B. Shepherd R. Larson, C. Highly stretchable electroluminescent skin for optical signaling and tactile sensing. *Science*, 351(6277):1071–1074, 2016.

[13] Zhao X. Illeperuma W. R. Chaudhuri O. Oh K. H. Mooney D. J. Suo Z. Sun, J. Y. Highly stretchable and tough hydrogels. *Nature*, 489(7414):133–136, 2012.

[14] Sun J. Y. Foo C. C. Rothemund P. Whitesides G. M. Suo Z. Keplinger, C. Stretchable, transparent, ionic conductors. *Science*, 341(6149):984–987, 2013.

[15] Vosgueritchian M. Tee B. C. Hellstrom S. L. Lee J. A. Fox C. H. Bao Z. Lipomi, D. J. Skin-like pressure and strain sensors based on transparent elastic films of carbon nanotubes. *Nature nanotechnology*, 6(12):788–792, 2011.

CHAPTER 2

HIGHLY STRETCHABLE ELECTROLUMINESCENT SKIN FOR OPTICAL SIGNALING AND TACTILE SENSING

2.1 Abstract

Cephalopods such as octopuses have a combination of a stretchable skin and color tuning organs to control both posture and color for visual communication and disguise. We present an electroluminescent material that is capable of large uniaxial stretching and surface area changes while actively emitting light. Layers of transparent hydrogel electrodes sandwich a ZnS phosphor-doped dielectric elastomer layer, creating thin rubber sheets that change illuminance and capacitance under deformation. Arrays of individually controllable pixels in thin rubber sheets were fabricated using replica molding and were subjected to stretching, folding, and rolling to demonstrate their use as stretchable displays. These sheets were then integrated into the skin of a soft robot, providing it with dynamic coloration and sensory feedback from external and internal stimuli.

2.2 Background

Biological systems employ a host of strategies for visual display and camouflage. Cephalopods, for example, can mimic their environment by changing skin color and texture, as well as posture [16]. Recent developments in soft robotics [17, 18], bioinspired design [19, 20], and stretchable electronics [21] reveal strategies that enable us to engineer some of the functions of cephalopod skin synthetically. For example, microfluidic networks filled with liquid dyes have been used as active camouflage and displays for soft mobile robots, giv-

ing them the ability to change their appearance via color, texture, and luminescence [22]. More recently, electromechano-chemically responsive films were exploited to render fluorescent patterns under the control of electric fields [23], and adaptive optoelectronic camouflage systems have been used to mimic the visual appearance of cephalopod skin [24]. Another approach is the use of active display technologies, such as polymeric light-emitting devices (PLEDs) and organic light-emitting diodes (OLEDs), which use stretchable transparent electrodes based on indium tin oxide (ITO) films [25], graphene [26], single or multi-walled carbon nanotubes (SWNTs or MWNTs) ([27], [28]), polyethylene-dioxythiophene: polystyrene-sulfonate (PEDOT:PSS) [29], or other percolated networks of conductive colloids or nanowires [30]. Despite the broad applicability of LED-based systems for consumer displays, their electrical function is limited to ultimate strains, $\epsilon_{ult} < 120\%$ [31], well below the ultimate strain of elastomers (such as silicones; $\epsilon_{ult} \sim 400$ to 700%) that are used in soft robotics to mimic the movements of animals.

Biological skin also enables animals to sense their environments. A number of approaches have been used to create pressure-sensitive electronic skins, including arrays of organic field-effect transistors (FETs) deposited on flexible parylene-polyamide substrates [32, 33] and inside stretchable rubber [34], as well as thin Au films and liquid metal embedded in polydimethylsiloxane (PDMS) [34, 35]. More recently, dielectric elastomer transducers (DETs), which are stretchable capacitors composed of highly extensible ionic hydrogels, have been used. These hydrogels are intrinsically soft, highly transparent in the visible spectrum (extinction coefficient $\mu_{ext} \sim 10^{-6}$ mm^{-1} [36], can exhibit very high ultimate strain ($\epsilon_{ult} \sim 2000\%$) and toughness ($U \sim$ 9 kJ m^{-2}) [37], and have relative changes in resistivity with strain that are orders of magnitude less than

those of electrodes based on percolated networks of conductive particles (such as metal nanoparticles, carbon powder, or nanotubes) [38].

Presently, soft robots are primarily used because their low mechanical compliance enables safe human-robot interaction; however, their potential is limited by a lack of suitable electronics that can stretch continuously with their bodies. No soft robot can dynamically display information on its body, and there are relatively few examples that can sense external and internal stimuli. Here we present a hyperelastic light-emitting capacitor (HLEC) that enables both light emission and touch sensing in a thin rubber sheet that stretches to >480% strain (Fig. 2.1A). These HLECs are composed of ionic hydrogel electrodes and composites of doped ZnS phosphors embedded in a dielectric matrix of silicone elastomer. We used electroluminescent (EL) phosphor powders that emit light via excitations within intrinsic heterojunctions under an AC electric field; unlike current-driven LEDs, which require lithography to form p-n junctions, this material system can be processed using replica molding. Application of an AC electric field causes luminescence within the semiconducting phosphor at wavelength centers corresponding to the dopants in the ZnS lattice. Green and blue centers are typically produced using low (~ 0.01 wt %) and high (~ 0.1 wt %) concentrations of Cu, whereas yellow is produced using Mn (~ 1 wt %) [39]. White light can be achieved using combinations of these dopants.

2.3 HLEC Design and Fabrication

The HLEC (Fig. 2.1B) is a five-layer structure consisting of an electroluminescent dielectric layer that is sandwiched between two electrodes and encapsulated in low elastic modulus ($E \sim$ 30 kPa) [40] silicone (Ecoflex 00-30, Smooth-on Inc.). Our hydrogel electrodes are designed with a balance of high mechanical tough-

ness, low volatility, and low electrical resistance under deformation (fig. 2.5 and data table 2.1). Aqueous lithium chloride (LiCl) is used as the ionic conductor because of its high conductivity ($\sim$ 10 Sm^{-1}), ionic strength, and hygroscopic nature, whereas polyacrylamide (PAM) is used as the elastomeric matrix because of its high toughness [41] and optical transparency. Electrodes are synthesized by first dissolving acrylamide monomer (AAm), polyacrylamide, and N,N-methylenebisacrylamide crosslinker in aqueous LiCl and casting the solution onto an ultraviolet (UV)–ozone–treated silicone (Ecoflex 00-30) substrate. The aqueous PAM-AAm solution is then crosslinked under UV light [42], producing a highly stretchable and transparent electrode. The EL layer is formed by mixing commercially available phosphor powders (Global Tungsten and Powders) (25 mm, $\sim$ 8% by volume) into silicone (Ecoflex 00-30) and then molding the dispersion into a 1-mm-thick sheet. Finally, we bond the EL layer between the two electrode-patterned silicone substrates and encapsulate the capacitor in an insulating layer of silicone.

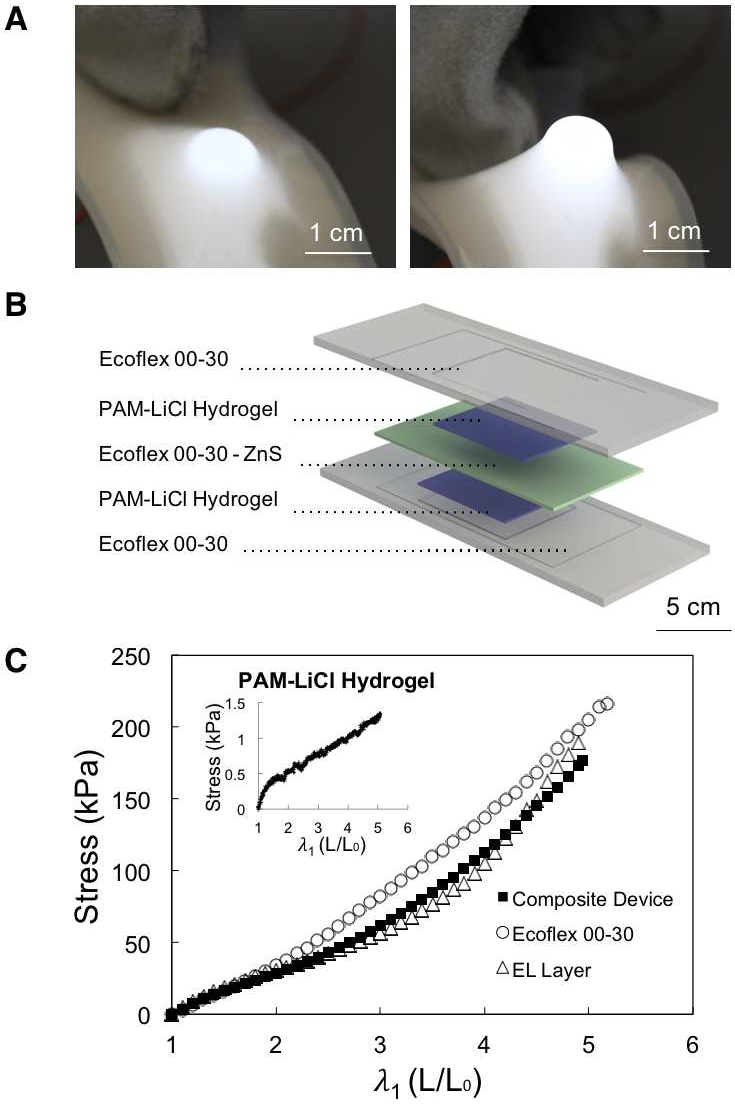

Figure 2.1: **Hyperelastic light emitting capacitor (HLEC)**. (A) Image of the HLEC conforming to the end of a pencil. (B) Exploded view of the HLEC showing its five-layer structure consisting of a 1 mm thick electroluminescent layer (ZnS-Ecoflex 00-30) that is sandwiched between two PAM-LiCl hydrogel electrodes and encapsulated in Ecoflex 00-30. (C) Stress-stretch curves of Ecoflex 00-30, the electroluminescent layer, and the composite device. The hydrogel data is shown in the inset due to its much lower elastic modulus.

2.4 HLEC Characterization

2.4.1 Mechanical Properties

The stress-strain curves of the HLEC and its silicone-containing layers (Ecoflex and Ecoflex-EL composite) are all coincident, whereas the elastic modulus of the hydrogel is two orders of magnitude lower, allowing the HLEC to stretch freely without delaminating. Mechanical testing data (Fig. 2.1C and data table S2) and images (Fig. 2.2A, data table S3, and movie S1) show the excellent adhesion between the layers. The HLEC achieved a mean strain of 487 ± 59% (SD), as measured at five locations across the width of the illuminated section, with portions exceeding 500% before the external copper leads lost contact with the hydrogel electrodes. For these tests, the HLECs were operated at 700 Hz under a nominal electric field of 25 kV cm^{-1}, with a power consumption of 0.2 W and a luminous efficacy of 43.2 millilumens per watt (mlm W^{-1}) [43]. We used this same replica molding technique to form an 8-by-8 array of 4-mm pixels (Fig. 2.3A). This HLEC display can undergo many deformation modes, including stretching, rolling, folding, and wrapping (Fig. 2.3, B to E, and movie S2). Dynamic control of the pixels is shown in Fig. 2.3, F to I.

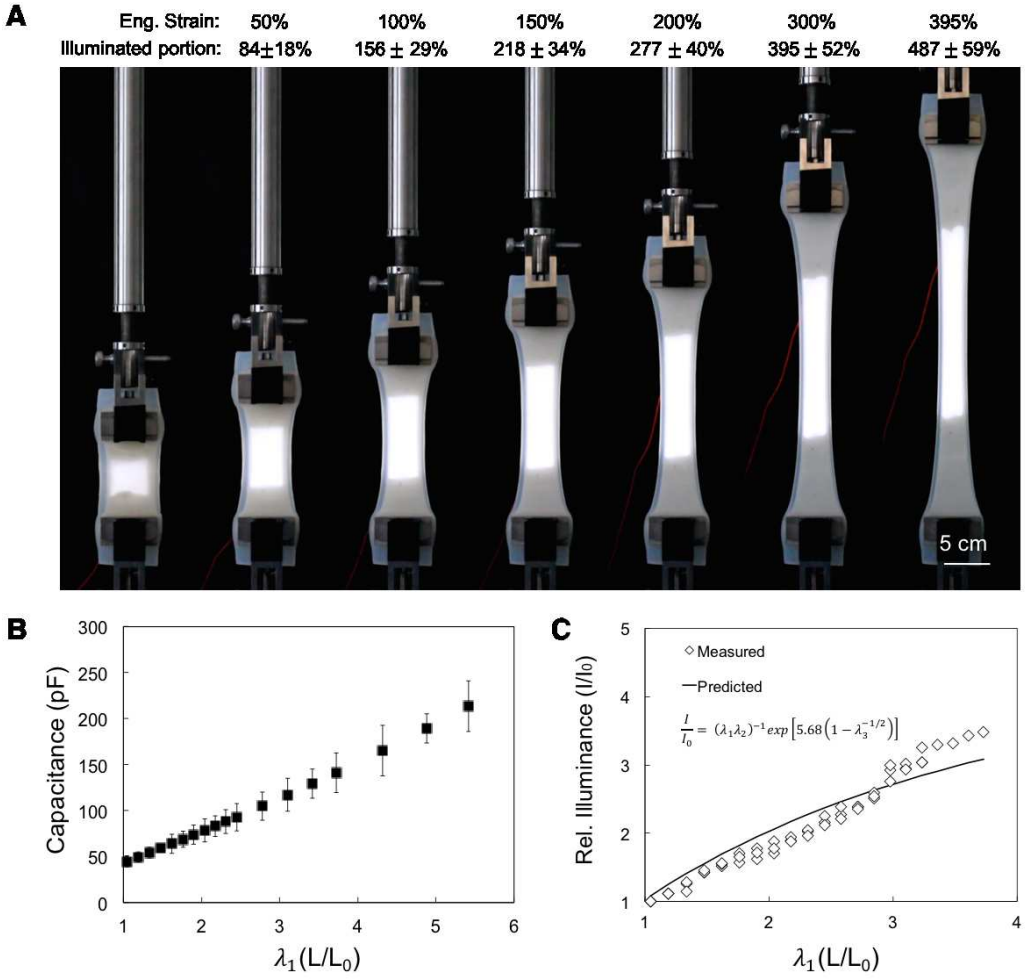

Figure 2.2: **The capacitive and luminescent behavior of the HLEC display under uniaxial stretching.**. A nominal electric field of 25 kV cm^{-1} was applied to the HLEC at the start of the uniaxial test. Five lengths were measured using image analysis software to obtain λ_1 across the width of the illuminated portion of the tensile bar. We report the mean and standard deviation of those measurements. At an engineering strain (grip-to-grip) of 395%, we measured the mean strain of the illuminated portion to be 487%, with a range of 420 - 549%. (B) The capacitance of the HLEC as a function of its uniaxial stretch (n = 4). (C) The relative illuminance of the HLEC versus its uniaxial stretch (n = 4) plotted alongside predicted values (supplementary online text).

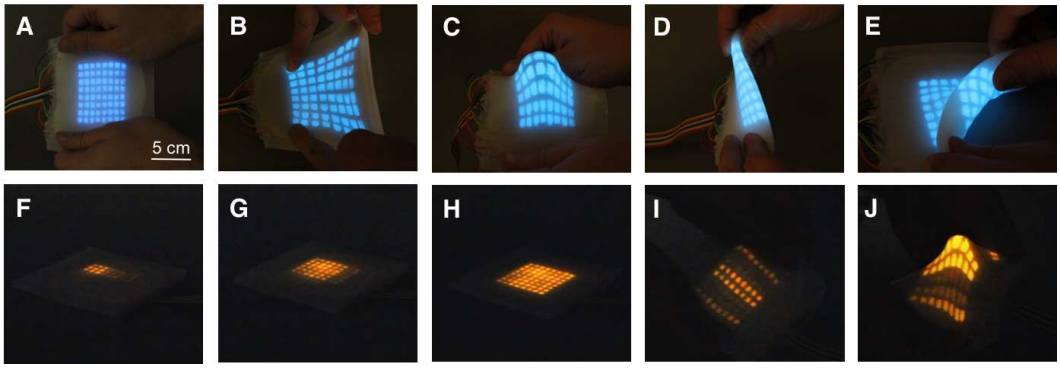

Figure 2.3: **Multi-pixel electroluminescent displays fabricated via replica molding**. The device measures 5 mm thick, with each of the 64 pixels measuring 4 mm. We show the devices in various states of deformation and illumination: (A) undeformed, (B) stretched, (C) wrapped.

2.4.2 Capacitance Sensing

In addition to emitting light, the HLEC also serves as a dielectric elastomer sensor (DES), due to its construction as a parallel-plate capacitor. Changes in the electrode area (A) and separation distance (d) cause the capacitance (C) to change according to $C/C_0 \propto Ad^{-1}$, allowing the HLEC to sense deformations from pressure and stretching. The capacitance of the HLEC changes as it is stretched under uniaxial (Fig. 2.2B and data S4) and biaxial (fig. 2.6 and data S5) tension [43]. We model the capacitance by expressing A and d in terms of the principal stretches, λ_1, λ_2, and λ_3, which represent the axial, transverse, and out-of-plane orientations, respectively (supplementary text). For uniaxial boundary conditions, we observe that the relative capacitance increases linearly as the sample is stretched (eq. 2.12). For biaxial test conditions, we observe that the relative change in capacitance follows $C/C_0 = \lambda_1^4$ (eq. 2.13); however, at higher strains, the measured values are slightly lower, due to a decrease in the permittivity of the dielectric [38].

2.4.3 Luminescent Behavior

The illuminance of the HLEC also increases as the device is stretched. We attribute this change to two interrelated phenomena: (i) the increase in electric field (E) as d decreases and (ii) the decrease in areal number density of phosphor particles (h) as A increases. Starting with the Alfrey-Taylor equation (eq. 2.14, fig. 2.7, and data table S6) [44], we predict the scaling law in Eq. 2.1 by expressing E/E_0 as a function of the principal stretches and by correcting for the change in h with stretching ($h/h_0 \propto A_0/A$) (supplementary text). The predicted trend is shown alongside luminescence measurements in Fig. 2.2C (data table S7).

$$\frac{I}{I_0} = (\lambda_1\lambda_2)^{-1} \exp\left[5.68\left(1 - \lambda^{1/2}\right)\right], \tag{2.1}$$

2.5 HLEC Displays that Actively Change Shape

To demonstrate the ability to monolithically integrate the HLEC into soft systems, we embedded three HLEC panels in a crawling soft robot by bonding six layers together. The top four layers make up the electroluminescent skin, whereas the bottom two are used for pneumatic actuation (Fig. 2.4A). Inspired by architectures developed for mobile soft robots [45], our pneumatic actuator uses a series of inflatable chambers embedded in silicone, with a bottom layer composed of an inextensible fiber-elastomer composite [43]. The inextensible layer induces a net bending moment as the pneumatic chambers are inflated; the resulting curvature is exploited to create an undulating gait.

The crawling robot uses its HLEC skin to sense its physical state and environment (i.e., proprioception and exteroception). The capacitance of the HLEC

changes with pneumatic actuation (Fig. 2.4B and data S8) and externally applied pressure (Fig. 2.4, C and D, and data table S9) [25]. Actuation of the three underlying pneumatic chambers results in capacitance changes (DC) of up to 1000% when the chambers are fully inflated. Additionally, each HLEC panel is largely decoupled from the state of the surrounding pneumatic chambers (Fig. 2.8 and data table S11) [43]. The ability to identify the actuated state of the robot using the capacitive sensor readings enables proprioception. To demonstrate the tactile sensing capabilities of the electronic skin, we pressed each of the HLEC panels on the robot and measured the capacitive response (Fig. 2.4C). A firm finger press resulted in a ~25% increase in capacitance. The relative capacitance versus applied pressure, ranging from 0.9 to 30.9 kPa, remained nearly constant over a period of 120 hours (Fig. 2.4D). Arrays of these tactile sensors enable exteroception in soft robotic systems. An array of three HLEC panels patterned into the three-chambered crawling robot enables eight distinct illuminated states (Fig. 2.4E). The embedded HLEC remains functional as the robot is actuated through its crawling sequence (Fig. 2.4F and movie S3). During actuation, the embedded HLEC undergoes stretches of $\lambda_1 = 2.63$ and $\lambda_2 = 2.42$ in the longitudinal (front to rear) and transverse (side to side) directions, respectively, to produce a ~635% increase in the skin's surface area (Fig. 2.9). Similar to the single-panel HLEC (movie S1), the luminescence of the embedded skin increases during actuation as its thickness is decreased.

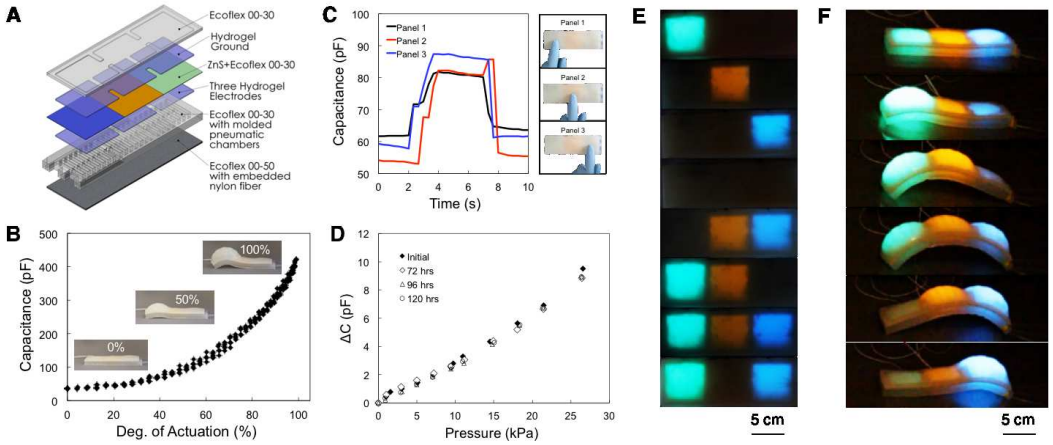

Figure 2.4: **HLEC skins endow soft robots with the ability to sense their actuated state, environment, and communicate optically**. (A) Schematic of a three-chambered soft robot. A series of three independently actuated pneumatic chambers are embedded between the HLEC skin (top) and a strain limiting layer (bottom). (B) Capacitance plotted versus the actuation amplitude, defined as the relative change in deflection between the uninflated and fully inflated states (n = 5). (C) A firm finger press induces a ~ 25% increase in capacitance. (D) Change in capacitance versus applied pressure. We observe a negligible change in the capacitive response of the sensors over a period of 120 hours. (E) Array of three HLEC panels, each emitting a different wavelength through selective doping of the EL phosphor layer. Each HLEC panel is activated independently. (F) An undulating gait is produced by pressurizing the chambers in sequence along the length of the crawler. This sequence produces forward locomotion at a speed of ~4.8 m hr^{-1} (~32 body lengths hr^{-1}). As each pneumatic chamber is pressurized, the outer electroluminescent skin is stretched, increasing the electric field across the EL layer and thus the luminescence.

2.6 Conclusions

Integrating these highly stretchable and compliant displays into soft actuators enables two new capabilities in soft electronics: (i) displays that actively change their shape and (ii) robots that actively change their color. Using replica mold-

ing, we fabricated a multipixel array of individually addressable HLECs, and we used the same process to monolithically integrate these displays into a soft robot capable of changing posture. The HLEC array imparts both dynamic coloration and the potential for feedback control, which would be useful in epidermal electronics (31) and robotics [46]. Although the luminous efficacy of our HLEC (43.2 mlm W^{-1}) is not as high as that of commercial AC powder electroluminescent devices (~4 lm W^{-1}) [46], it can be greatly improved by tuning the materials system and device architecture (such as higher transmissivity encapsulation layers, reduced thickness, and optimized particle size). For applications requiring higher display resolution, HLECs could be made compatible with photolithography and other microfabrication techniques by using photopolymerizable polymers. These techniques would also allow us to decrease the thickness of the electroluminescent layer, thereby reducing the voltage required to power the HLEC.

2.7 Supplementary Information

Materials. The hyperelastic light emitting capacitor (HLEC) and crawling robot are composed of intrinsically soft materials: silicones (Ecoflex 00-30; Smooth-On Inc.), polyacrylamide based LiCl hydrogel electrodes, and transition metal-doped ZnS phosphors (Global Tungsten & Powders Corp.) embedded in Ecoflex 00-30 as the active display material. Hydrogels are synthesized using acrylamide (AAm; Sigma-Aldrich) and polyacrylamide (PAM, M_W ~5x10^6) (92560; Sigma-Aldrich) swelled in aqueous LiCl (LiCl; Alfa Aesar) along with a crosslinker (N,N'-methylenebisacrylamide, or MBAA; Sigma-Aldrich) and a photoinitiator (Irgacure 1173; BASF). AAm and LiCl are dissolved in deionized water at a concentration of 1.75 M and 8 M, respectively, followed by PAM at a

weight ratio of 0.142 PAM:AAm. The solution is mixed on a magnetic stirrer at 60 °C for 4 hours, and then MBAA and Irgacure 1173 are added at a weight ratio of 0.01 and 0.016 :AAm, respectively. Mixing for two additional hours yields the uncured hydrogel electrode material.

Hyperelastic Light-Emitting Capacitor (HLEC) fabrication. The synthetic skin is fabricated using replica molding. The outer layers (see Fig. 2.1B) are formed by casting Ecoflex 00-30 into 3D printed molds (Objet 30; Stratasys Ltd.) followed by curing at 80 °C for 20 minutes. We treated the bonding surfaces with UV-ozone for 10 minutes. We poured the uncured hydrogel into the 1 mm electrode relief pattern and cured it for 15 seconds under UV light (320-500 nm, 200 W) (Model S1500; Lumen Dynamics) to create the top and bottom electrodes. We formed the electroluminescent (EL) layer by mixing EL phosphor powders with Ecoflex 00-30 (7.8 wt. % phosphor), and then casting the dispersion into the 1 mm relief pattern (cured at 80°C). We use orange (GGL11X), green (GG41X), blue (GGL61X), and white (GGL71X) phosphor powders (Global Tungsten & Powder Corp.) to produce the colors shown in this manuscript. The entire structure is encapsulated in Ecoflex 00-30. The resulting device has a total thickness of 8 mm with staggered electrodes that enable connection to an external power source using stranded copper wire inserted through the silicone.

Integration of HLEC into a crawling soft robot. HLECs are molded into the body of the soft robotic crawler as shown in (Fig. 2.4A, Fig. 2.10). Plastic molds were 3D printed for each layer (Objet 30; Stratasys Ltd.). Three independently controlled inflatable chambers actuate the front, middle, and rear sections of the robot. The extensible top layer of the robot contains separate reservoirs for each of the three electrodes, while the bottom is bonded to an inextensible elastomeric composite consisting of a woven nylon sheet (9318T18, McMaster-Carr

Supply Co.) embedded in silicone (Ecoflex 00-50; Smooth-On Inc.). The top electrodes and encapsulation layers are then added using general HLEC fabrication methods.

Capacitance and luminescence of HLEC v. stretching. Capacitance was measured under uniaxial stretch by connecting a capacitance meter (830C; BK Precision) to the hydrogel electrodes using stranded copper wires (Data S1). Luminescence of the HLEC was observed and measured under uniaxial stretching using a mechanical tester (Z010; Zwick Roell) and a portable light meter (HHLM 1337; Omega Engineering Inc.). Specimens were mounted on the machine, connected to an alternating current (AC) voltage source (2.5 kV, 700 Hz), and subjected to uniaxial tension. We used a high-voltage amplifier (610 D; TREK Inc.) coupled with a function generator (3312 A; Hewlett Packard) to power the HLEC. A strain rate of 100% min^{-1} was used in all tests. The engineering strain (grip-to-grip) was recorded using the controller software, while the strain within the luminescent area was measured from recorded video using Image-J. The illuminance was measured by placing the light-meter ~5 mm from the center of the luminescent area with a shield to block interference from ambient light (Data S2).

Biaxial stretching of HLEC. Biaxial stretching was performed using a radially folding acrylic frame (Fig. 2.7B, C) [47]. Circular test specimens (50 mm diameter) were fabricated using replica molding with 3D printed molds (UP Plus 2; Beijing TierTime Technology Co. Ltd). Each test specimen contained a 20 mm HLEC. The test samples were bonded to the frame (Sil-Poxy; Smooth-On Inc.) and their capacitance was measured (830C; BK Precision) at set intervals as the frame was expanded. The collected data (Data S3) is plotted in (Fig. 2A).

Exteroception and proprioception of electroluminescent skin. Capacitance mea-

surements were taken on the electroluminescent skin embedded in the soft robot. The top and bottom hydrogel electrodes were connected to the capacitance meter. A program written in Processing was used to communicate with the capacitance meter and an ATmega328 microcontroller (Arduino Uno R3; Adafruit). This program coordinates data retrieval and logging from the capacitance meter and controls a solenoid valve to pressurize each chamber. The solenoid valve is activated using a signal from the ATmega328 to precisely time the input of pressurized air into the actuator. The testing apparatus is shown in Fig. 2.8B. Pressure from human touch was measured on individual panels (Data S4). The applied force was manually controlled by simply pressing each panel. Capacitance measurements were also taken on the panel as known weights were applied externally to the panel (Data S5) and as the underlying pneumatic chambers were pressurized (compressed air, 7 psi, ~48 kPa) (Data S6). The degree of actuation was defined based on the morphology of the undulation, which we control using input pressure and time. Lastly, we measured the capacitance (Fig. 2.8C, Data S7) of the center pneumatic chamber in each possible state of the surrounding chambers (Fig. 2.8A).

Soft robot locomotion. The undulating gait used for crawling included six steps: (i) only the rear chamber pressurized, (ii) rear and middle chambers pressurized, (iii) all three chambers pressurized, (iv) middle and front chambers pressurized, (v) front chamber pressurized, and (vi) no chambers pressurized. Each actuation was driven by a nominal pressure of 4.7 psi (~32 kPa). This sequence produces forward locomotion at a speed of ~4.8 m hr^{-1} (~32 body lengths hr^{-1}). Panel illumination during crawling was powered by an amplifier (610 D; TREK Inc.).

Resistance of hydrogel electrode under uniaxial strain. The resistance of hydro-

gel was examined under uniaxial strain using a precision LCR meter (E4980A; Agilent) (Data S8). All measurements were conducted with a 5 mm gage length. The nominal (or unstretched) resistance was 59.96 ± 1.93 Ω (SD), while at 300% strain it increased to 144.33 ± 4.99 Ω (SD). We also examined the cyclic resistance variation of the electrodes by measuring resistance over 10 successive stretching cycles; we observed negligible resistance variation (Fig. 2.5).

Illuminance of HLEC as a function of voltage. The illuminance (luminous flux per unit area, measured in lux) of the HLEC was measured using a light meter (HHLM 1337; Omega Engineering Inc.) (Data S9). Samples were pre-stretched (ϵ = 135%), mounted on the tensile tester (Z010; Zwick Roell), and connected to the external voltage source. Illuminance was measured as a function of voltage (at 700 Hz). The light meter was held at a distance of 5 mm from the center of the HLEC in all tests. As shown in Figure 2.7, the illuminance increases by a factor of 20 as the voltage is increased from 2.5 - 5 kV (in accordance with Eq. 2.14).

Power consumption and luminous efficacy. We used a simple test circuit (Fig. 2.12) to measure the power consumption of the HLEC (Fig. 2.2A) while illuminated in its unstretched state. We applied an AC waveform using a high-voltage amplifier (610 D; TREK Inc.) coupled with a function generator (3312 A; Hewlett Packard). We applied a nominal voltage input of 2.5 kV at 700 Hz to the high voltage input of the test circuit. We used a multimeter (83V; Fluke Corp.) to measure $V_{RMS,BA}$ (the root mean square, RMS, voltage across R_2), $V_{RMS,A}$ (the RMS voltage across R_1), and the resistance of each resistor (Table 2.1). We calculated the RMS current across each resistor using $I_{RMS} = V_{RMS} R^{-1}$. Using Kirchoff's current law, we equated the current through resistors 1 and 2:

$$I_{RMS,2} = \frac{V_{RMS,BA}}{R_2} = \frac{V_{RMS,A}}{R_3} = I_{RMS,3}, \tag{2.2}$$

Using Eq. 2.2, we calculated $V_{RMS,CA}$ (the voltage across the entire test circuit):

$$V_{RMS,CA} = V_{RMS_CB} + V_{RMS,BA} = \left(1 + \frac{R_3}{R_2}\right)V_{RMS,BA}, \tag{2.3}$$

The current across the first resistor (R_1) is equal to the total current through the test circuit. Using this equality, we calculated the power of the test circuit using

$$P_{real,total} = I_{RMS,total}cos(\theta) = I_{RMS,1}V_{RMS,CA}cos(\theta), \tag{2.4}$$

where θ represents the phase shift between the current and voltage waveforms across the test circuit. This phase shift was measured using an oscilloscope (TDS 1012; Tektronix) (Table 2.1). We calculated the real power of the test circuit to be 1.86 W [43]. This power consumption includes energy used by the HLEC and the resistors according to

$$P_{Total} = P_{HLEC} + P_{Resistor}, \tag{2.5}$$

We subtracted the power consumption of the resistors to find the power consumption of the HLEC. We used $P=V_{RMS}I_{RMS}$ to calculate the power consumed by each resistor. The cumulative power consumption of the three resistors was 1.66 W. Therefore the power consumption of the illuminated HLEC (Fig. 2.2A) was approximately 0.20 W. The illuminance of this HLEC was measured to be

4.32 cd sr m^{-2} (Model HHLM 1337; Omega Engineering Inc.), with a calculated luminous efficacy of 43.2 millilumens per Watt (mlm W^{-1}).

Mechanical testing. Stress-strain curves were measured for Ecoflex 00-30 (Smooth-On Inc) with and without embedded ZnS phosphor powders (25µm), PAM-LiCl hydrogel and the composite HLEC using a tensile tester (Z010; Zwick Roell) (Data S10). A strain rate of 100% min^{-1} was used in all tests. The engineering strain (grip-to-grip) was recorded using the controller software, while the strain within the luminescent area was measured from recorded video using Image-J (Data S11).

Modelling of Capacitance Sensor Behavior. The capacitance of a parallel plate capacitor in the stretched (C) and unstretched (C_0) states scales according to Eq. 2.6 and Eq. 2.7, respectively. We use this basic model to understand how the capacitance of the HLEC behaves as the area (A) and thickness (d) are changed,

$$C \propto \frac{A}{d} \tag{2.6}$$

$$C_0 \propto \frac{A_0}{d_0}. \tag{2.7}$$

For uniaxial stretching, we approximate the relative change in A and d using Eq. 2.8 and Eq. 2.9, respectively. Here, λ_1, λ_2, and λ_3 represent the axial, transverse, and out-of-plane stretches of the illuminated portion of the HLEC. Still-frames extracted from video taken of the uniaxial tension test (Movie S1) were measured in Image-J to determine λ_1 and λ_2, and then the condition of incompressibility (Eq. S9) was invoked to determine λ_3.

$$A = A_0 \lambda_1 \lambda_2 \tag{2.8}$$

$$d = d_0 \lambda_3 \tag{2.9}$$

$$\lambda_1 \lambda_2 \lambda_3 = 1 \tag{2.10}$$

Combining Equations 2.6-2.10 yields the scaling law for the capacitance of the HLEC (Eq. 2.11).

$$\frac{C}{C_0} = \lambda_1^2 \lambda_2^2 \tag{2.11}$$

For an incompressible material (Eq. S9) under uniaxial tension, we expect $\lambda_2 = \lambda_3 = \lambda_1^{-1/2}$ as the sample is stretched axially (along λ_1). Applying this boundary condition to Eq. 2.11, we expect that the relative capacitance under uniaxial tension scales according to

$$\left(\frac{C}{C_0}\right)_{uniaxial} = \lambda_1. \tag{2.12}$$

For an incompressible material (Eq. 2.10) under biaxial tension, we impose $\lambda_1 = \lambda_2$. Applying this boundary condition to Eq. 2.11, we expect that the relative capacitance under biaxial tension scales according to

$$\left(\frac{C}{C_0}\right)_{biaxial} = \lambda_1^4. \tag{2.13}$$

Modelling of Luminescent Behavior. Here we use the Alfrey-Taylor model [44] to predict how the illuminance changes as a function of stretching in uniaxial tension. We start with Equation 2.14, which expresses the relative illuminance (I/I_0) as a function of applied voltage (V). From Figure 2.7, we observe that the HLEC behaves in accordance with Eq. 2.14. The fitting parameter (b = 15.71) was calculated using a least squares fit (R^2 = 0.983).

$$\frac{I}{I_0} = \exp\left[b(V_0^{-1/2} - V^{-1/2})\right] \tag{2.14}$$

Our goal is to express Eq. 2.14 in terms of the principle stretches along the axial, transverse, and out-of-plane directions in our uniaxial tension test (λ_1, λ_2, and λ_3, respectively). First we replace the voltage terms with electric field, E, using the relation to yield Eq. 2.15.

$$\frac{I}{I_0} = \exp\left[b\Big((E_0 d_0)^{-1/2} - (Ed)^{-1/2}\Big)\right] \tag{2.15}$$

Where E_0 represents the nominal electric field (2.5 kV cm^{-1}). We then invoke Eq. 2.9 to obtain

$$\frac{I}{I_0} = \exp\left[a\Big(1 - \lambda_3^{1/2}\Big)\right]. \tag{2.16}$$

where $a = b(E_0 d_0)^{-1/2}$. We also must account for the change in areal number density of EL particles, η, as the electrode area, A, increases. We propose that this affects the illuminance inversely according to the following scaling law:

$$\frac{I}{I_0} \propto \frac{\eta}{\eta_0} \propto \frac{A_0}{A}. \tag{2.17}$$

Combining Equations 2.8, 2.16, and 2.17 yields the relative change in intensity as a function of physical parameters that can be measured in the uniaxial tension test (λ_1, λ_2, and λ_3):

$$\frac{I}{I_0} = (\lambda_1 \lambda_2)^{-1} \exp\left[5.68\Big(1 - \lambda^{1/2}\Big)\right], \tag{2.18}$$

The illuminance was measured in uniaxial tension using a portable light meter (Model HHLM 1337; Omega Engineering Inc.) (Data S2). The results are shown in Fig. 2.2C, along values predicted using Eq. 2.18. The fitting parameter (a = 5.68) was calculated using a least squares fit (R^2 = 0.902).

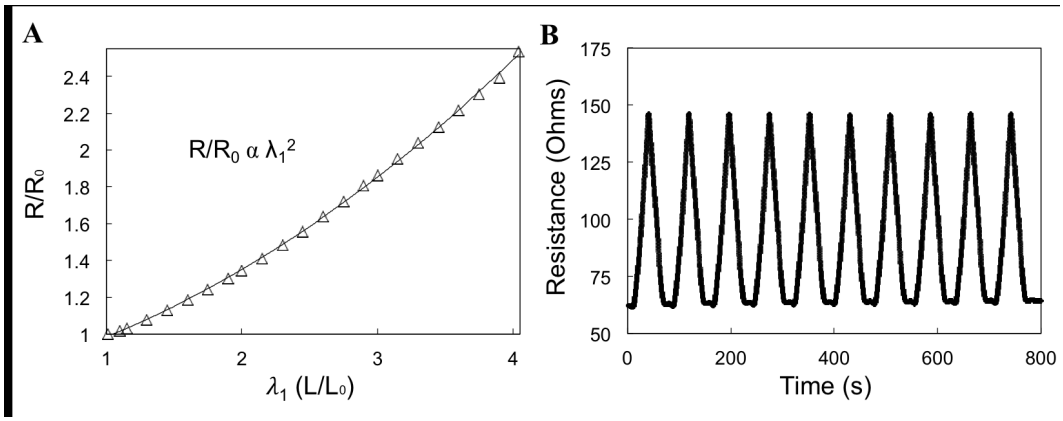

Figure 2.5: **Resistive behavior of PAM-LiCl hydrogel**. (A) The relative change in hydrogel resistance (R/R_0) increases with uniaxial strain (n = 5; standard deviation within markers). The relative change in resistance scales with λ_2 (note: $\lambda = \epsilon + 1$), and is consistent with recently reported conductive acrylamide hydrogel chemistries [22, 24]. (B) The hydrogel under cyclic loading for 10 cycles.

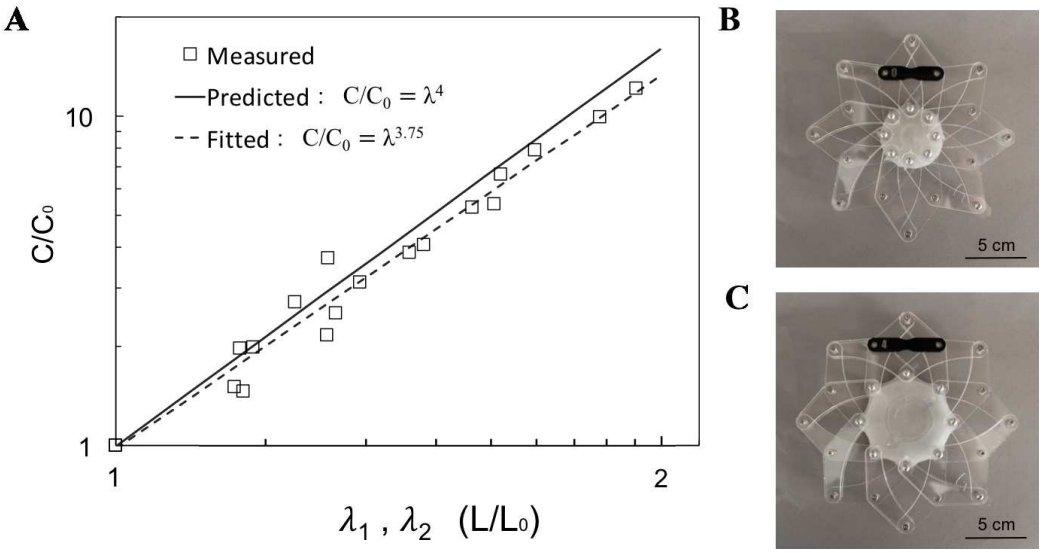

Figure 2.6: **Capacitance of the HLEC in equibiaxial tension**. (A) The relative change in capacitance follows the λ^4 dependence predicted in Eq. 2.13 (n = 3). (B) A circular HLEC test sample mounted in the biaxial test apparatus in the unstretched state. (C) The HLEC sample being stretched biaxially, with intervals set by a series of black acrylic linkages.

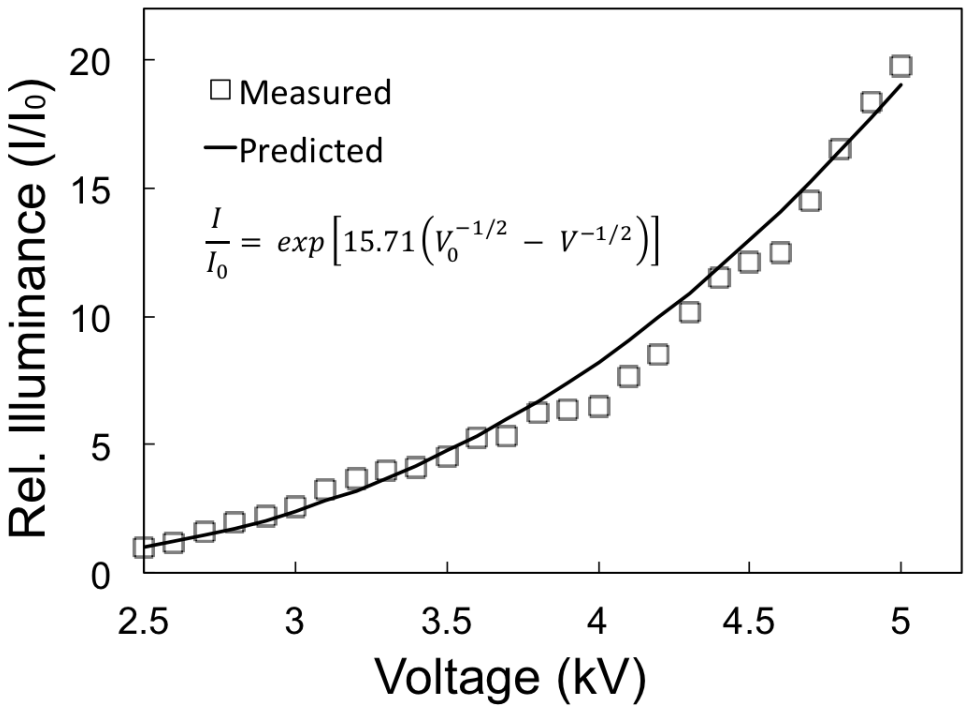

Figure 2.7: **Relative illuminance of the HLEC versus voltage**. Measurements are taken in the pre-stretched state (ϵ = 135%) at a constant frequency (700 Hz). Predicted values are calculated using Eq. 2.14. The fitting parameter (b = 15.71) was calculated using a least squares fit (R^2 = 0.983).

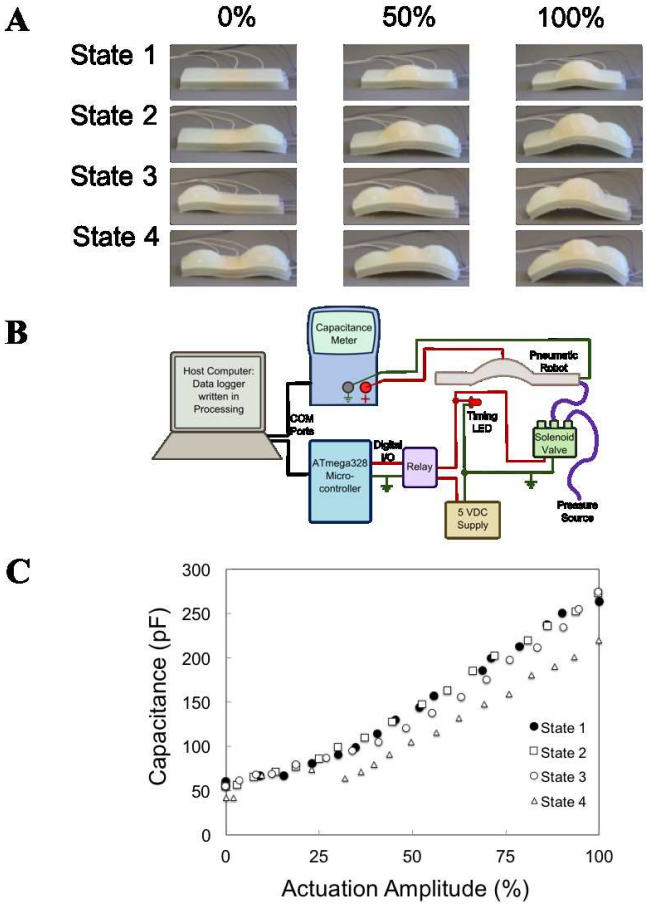

Figure 2.8: **Capacitance of the center HLEC panel measured as a function of actuation amplitude for various system states**. (A) The system states are shown visually; State 1: left and right panels non-pressurized, State 2: left panel non-pressurized, right panel pressurized, State 3: left panel pressurized, right panel non-pressurized, and State 4: left and right panels pressurized. (B) Experimental setup for measuring capacitance as pneumatic chambers are inflated. (C) Capacitance of the center HLEC as a function of the actuation amplitude of the center pneumatic chamber for each of the four states. The capacitance is largely independent of the actuation level of neighboring chambers.

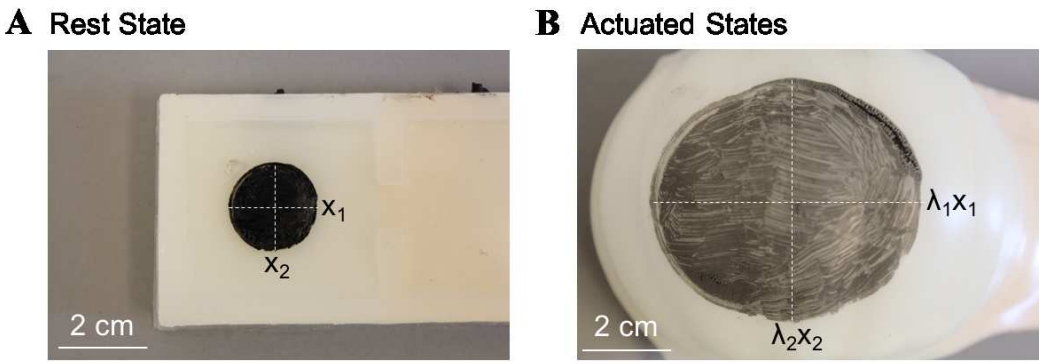

Figure 2.9: **Deformation of the HLEC during pneumatic actuation of the robot**. The principal stretches, λ_1 and λ_2, which correspond to the longitudinal (x_1) and transverse (x_2) directions, respectively, were measured as the robot was actuated through the crawling sequence (shown in Fig. 2.4F). (A) A circular fiducial mark was placed on the HLEC and measured along its major (x_1) and minor (x_2) axes. (B) The principal stretches shown in this figure are $\lambda_1 = 2.63$ and $\lambda_2 = 2.42$. These measurements account for out-of-plane deformation of the inflated chamber (not captured in this 2D image). We observe that the surface area of the ellipse in the deformed state is ~635% larger than the nominal circular fiducial mark in the rest state ($A/A_0 = \lambda_1\lambda_2$).

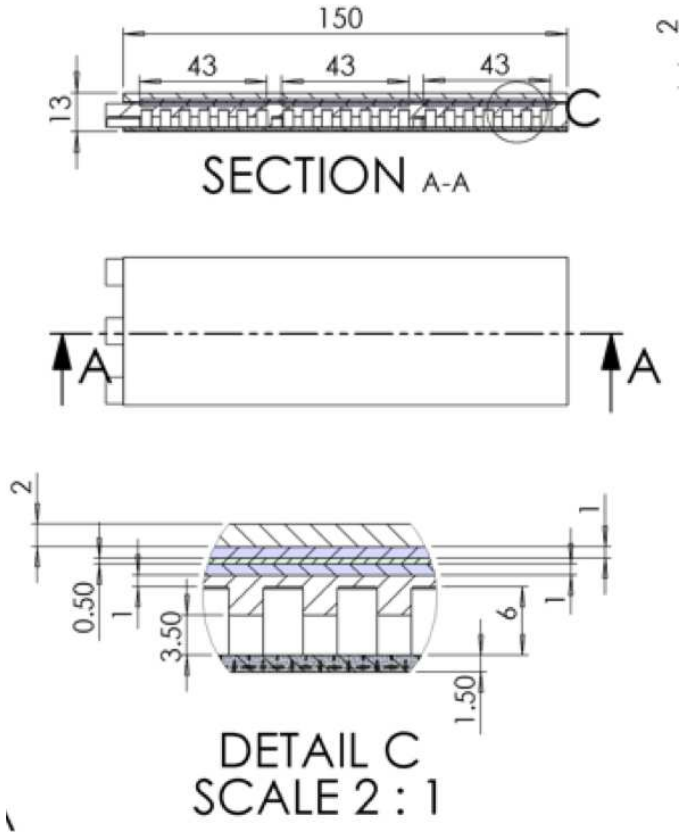

Figure 2.10: **Dimensioned drawing of the soft robot**. The robot has three independently actuated pneumatic chambers corresponding to three HLEC panels. Dimensions are shown in mm.

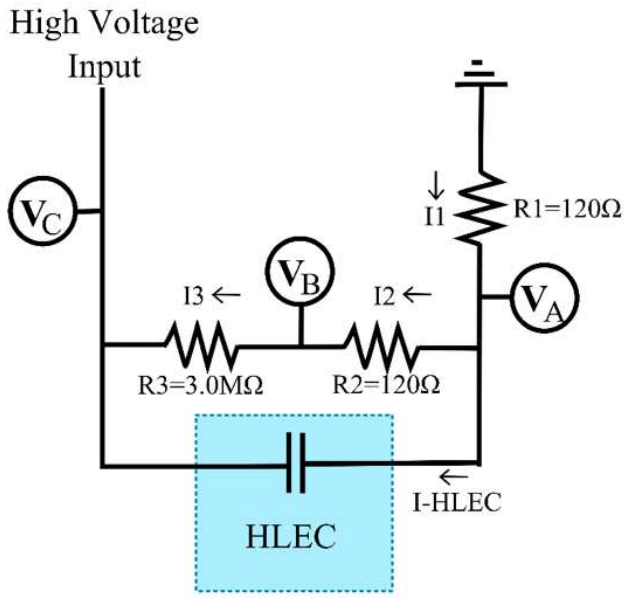

Figure 2.11: **Test circuit used to measure power consumption of the HLEC.**

Table 2.1: Power consumption measurements for the HLEC. The test circuit used to measure these values is shown in Fig. 2.11.

$V_{RMS,BA}(mV)$	88.2
$V_{RMS,A}(mV)$	101.5
$R_1(\Omega)$	118.3
$R_2(\Omega)$	118.6
$R_3(M\Omega)$	2.993
$R_1(\circ)$	13.5

REFERENCES

[16] L. Mäthger R. T. Hanlno A. Barbosa, J. J. Allen. *Proc. R. Soc. London Ser. B*, 279:84—-90, 2012.

[17] R. F. Shepherd X. Chen G. M. Whitesides F. Ilievski, A. D. Mazzeo. *Angew. Chem. Int. Ed. Engl.*, 50:1890–1895, 2011.

[18] M. T. Tolley D. Rus. *Nature*, 521:467–475, 2015.

[19] M. J. Spenko et al. *J. Field Robot*, 25:223–242, 2008.

[20] E. Kreit et al. *J. R. Soc. Interface*, 10, 2012.

[21] Y. Huang J. A. Rogers, T. Someya. *Science*, 327:1603–1607, 2010.

[22] S. A. Morin et al. *Science*, 337:828–832, 2012.

[23] S. L. Craig X. Zhao Q. Wang, G. R. Gossweiler. *Nat. Commun.*, 5(4899), 2014.

[24] C. Yu et al. *Proc. Natl. Acad. Sci.*, 111:12998–13003, 2014.

[25] P. E. Burrows et al. *Displays*, 22:65–69, 2001.

[26] T. H. Han et al. *Nat. Photonics*, 6:105–110, 2012.

[27] T. Sekitani et al. *Nat. Mater.*, 8:494–499, 2009.

[28] M. K. Shin et al. *Adv. Mater.*, 22:2663–2667, 2010.

[29] M. S. White et al. *Nat. Photon.*, 7:811–816, 2013.

[30] J. Y. Lee P. Peumans Y. Cui L. Hu, H. S. Kim. *ACS Nano*, 4:2955–2963, 2010.

[31] X. Niu Z. Yu Q. Pei J. Liang, L. Li. *Nat. Photon.*, 7:817–824, 2013.

[32] T. Someya et al. *Proc. Natl. Acad. Sci. U.S.A.*, 102:12321–12325, 2005.

[33] K. Takei et al. *Nat. Mater.*, 9:821–826, 2010.

[34] T. Someya et al. *Proc. Natl. Acad. Sci. U.S.A.*, 101:9966–9970, 2004.

[35] R. J. Wood Y. L. Park, B. R. Chen. *IEEE Sens. J.*, 12:2711–2718, 2012.

[36] S. P. Lacour D. P. J. Cotton, I. M. Graz. *IEEE Sens. J.*, 9:2008–2009, 2009.

[37] C. Keplinger et al. *Science*, 341:984–987, 2013.

[38] J. Y. Sun et al. *Nature*, 489:133–136, 2012.

[39] G. M. Whitesides Z. Suo J. Y. Sun, C. Keplinger. *Adv. Mater.*, 26:7608–7614, 2014.

[40] A. Kitai. *Luminescent Materials and Applications*, page 249–268, 2008.

[41] R. M. D. Nunes G. M. Whitesides R. F. Shepherd, A. A. Stokes. *Adv. Mater.*, 25:6709–6713, 2013.

[42] Y. Bai et al. *Appl. Phys. Lett.*, 105:151903, 2014.

[43] Materials and methods are available as supplementary materials. *Science Online*.

[44] J. B. Taylor G. F. Alfrey. *Proc. Phys. Soc. B*, 68:775–784, 1955.

[45] R. F. Shepherd et al. *Proc. Natl. Acad. Sci. U.S.A.*, 108:20400–20403, 2011.

[46] D. H. Kim et al. *Science*, 333:838–843, 2011.

[47] J. Kim et al. *Nat. Commun.*, 5:5747, 2014.

CHAPTER 3

VANISHING INTERFACES: UNTETHERED STRETCHABLE DISPLAYS FOR TACTILE INTERACTION

3.1 Abstract

While physical buttons provide tactile sensations that allow them to be identified and pressed without visual focus, their static nature limits their use for dynamic interfaces. Conversely, touchscreens offer highly flexible, task-specific interfaces, but do not provide the tactile qualities needed for vision-free interaction. Here we present a stretchable display that can change shape from a flat sheet into a dome when pressurized. The vanishing interface we designed uses hyperelastic light emitting capacitors (HLECs) that actively emit light, sense strain, and detect finger presses. We characterize the stretch and luminance of the device as the thin sheet is pressurized. Interestingly, but not unexpectedly, these HLEC panels show a pressure dependent luminance which we use to highlight where they are being pressed, a visual display of haptic information. We further demonstrate the co-located touch sensing and light emitting capabilities by developing an interactive memory game.

3.2 Background

The physical buttons and switches found on conventional control panels provide tactile feedback, allowing the user to identify buttons and provide input without shifting visual focus from safety critical tasks such as driving [48, 49, 50]. Touchscreen technologies, in contrast, can easily be reconfigured to task-specific interfaces, but lack the requisite tactile qualities for non-visual in-

teraction with machines [51]. To solve this contradiction, many methods have been used to combine the tactile qualities of physical buttons with the reconfigurable nature of digital interfaces. Arrays of independently controlled pneumatic chambers [52], motorized actuators [53, 54], and shape memory alloys [55, 56] have all been used to create surfaces that can dynamically change shape. Harrison et al. have developed pneumatically actuated laminate structures of translucent elastomers and rigid spacers that enable multiple dynamically changeable physical buttons to occupy the same footprint [57]. These methods, however, require external projection systems to incorporate visual displays into the tactile interfaces as they change shape.

Recent advances in stretchable electronics [58, 59, 60] have enabled soft display systems that can undergo large deformations. These stretchable displays are comprised of alternating current electroluminescent (ACEL) phosphors embedded in elastomer membranes and sandwiched between transparent elastomer electrodes [61, 62, 63, 64, 65]. These hyperelastic light emitting capacitors (HLECs) can actively emit light and sense deformation while undergoing areal strains of greater than 635% [63]; using these devices, we have previously reported a color changing soft robot with extero- and proprioceptive sense [63], as well as higher resolution displays capable of displaying multiple colors (R,G,B) and detecting multiple touch inputs [65].

Here we present a soft spherical interface comprised of HLECs that can actively emit light, sense touch and, when not in use, vanish into a flat sheet. This vanishing interface combines the best traits of physical buttons and electronic touchscreens—the pressurized elastomeric membrane allows tactile interaction while also providing co-located light emission and touch sensing capabilities. Our HLECs can be pressurized to form physical buttons when and where they

are needed (Fig. 3.1, Supplemental Video SV1), but vanish into the plane when not in use.

While previous stretchable electroluminescent devices [63, 64] needed to be tethered to a bulky and expensive high voltage amplifier (610 D; TREK Inc.) and function generator (3312 A; Hewlett Packard), we now present a standalone, battery-powered electronic system capable of delivering a high frequency (f ~ 1 kHz), high voltage (V ~ 4 kV) square wave input signal to illuminate the panels. This compact and portable electronic system senses changes in capacitance and pneumatically inflates a spherical array of four HLECs. To relate these inputs to the physical state of the system, we characterize the stretch and luminance as an unpressurized thin sheet and a pressurized hemisphere. Additionally, we found that the HLEC panel light intensity increases during finger pressing locally; we investigated this effect using image analysis. To demonstrate the utility of all these features, we integrated the core abilities of this system (co-located touch sensing and light emission) into an interactive memory game analogous to the game Simon ®.

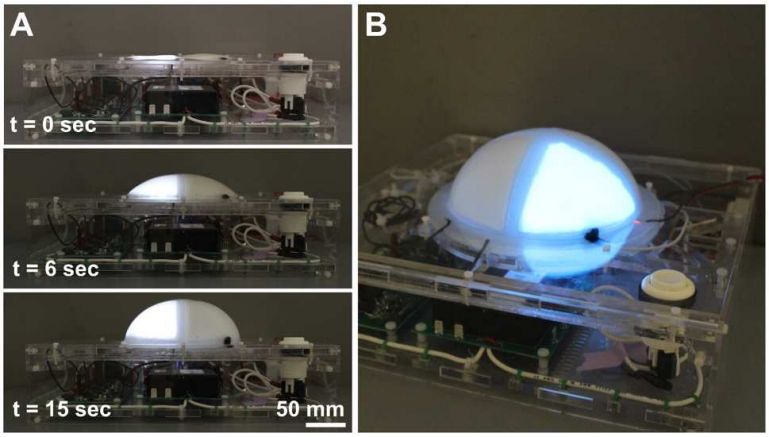

Figure 3.1: **Four hyperelastic light emitting capacitors (HLECs) form an untethered soft interface capable of emitting light and sensing touch.** (A) The membrane is pressurized using an integrated pump. (B) Fully inflated HLEC interface with one panel is illuminated using applied voltage, V ~ 4 kV, and frequency, f ~ 1 kHz.

3.3 Results

3.3.1 Soft Interface Design

We patterned four different colored and independently controlled HLEC panels into a circular membrane using replica molding. The center layer of the membrane is composed of an insulating dielectric layer of silicone (Ecoflex 00-30, Smooth-on Inc.) with embedded ZnS phosphor powders (Global Tungsten Powders). These phosphors emit light when exposed to a high electric field (E ~ 4 kV mm^{-1}), with color (orange, green, blue, and white) dependent on the concentrations of metallic dopants such as Cu and Mn [66]. This central dielectric layer is sandwiched between optically transparent, stretchable electrodes composed of a LiCl polyacrylamide hydrogel that exhibits high mechanical toughness, low volatility and high ionic conductivity [67]. These active layers are

encapsulated within a layer of silicone elastomer (Ecoflex 00-30), allowing the composite device to be safely handled when high voltages are applied. Each of the five layers has a nominal thickness of 1 mm, resulting in a total membrane thickness of ~ 5 mm. This composite structure and dimensions are shown in Fig. 3.2a and 3.2b, respectively.

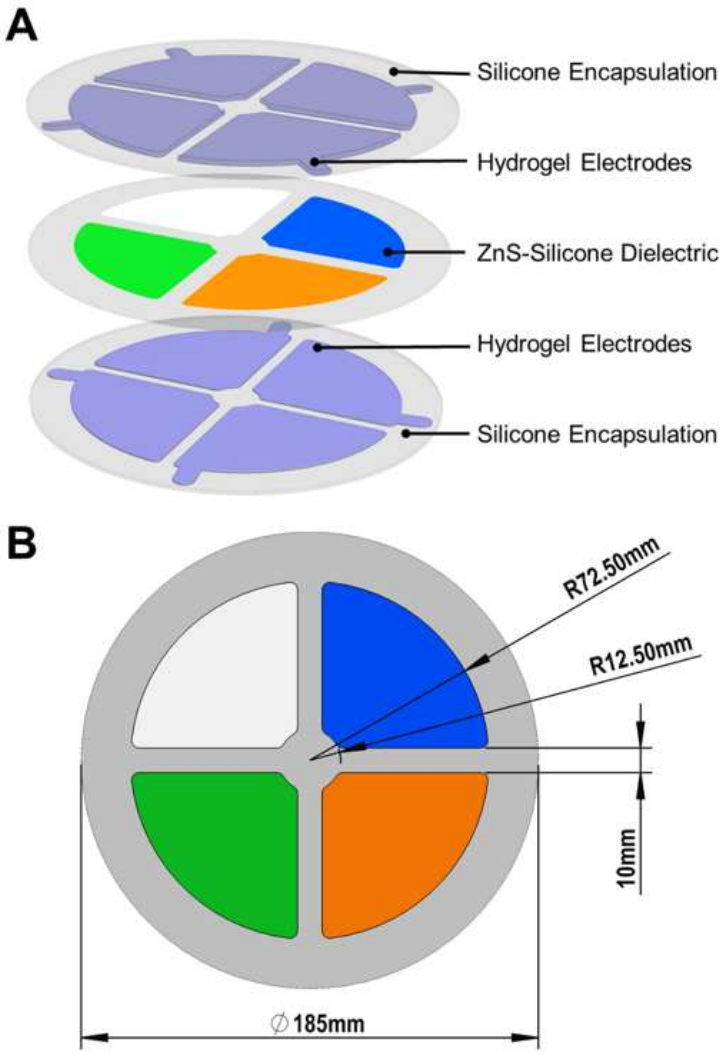

Figure 3.2: **Design of the elastomeric membrane with four independently controlled HLEC panels.** (A) Exploded view of the membrane showing its five- layer structure. A 1 mm thick electroluminescent dielectric layer is sandwiched between hydrogel electrodes and the device is encapsulated with a final layer of silicone. (B) Dimensioned drawing of the dielectric layer. The active area of the device has a diameter of 145mm, with a 20 mm border for mounting.

3.3.2 Control System

To generate the high electric field required to activate the HLEC panels, we use a regulated high voltage DC to DC converter (H40P; EMCO) to amplify a 24 VDC input into a 4,000 VDC output. A high voltage MOSFET (IXTT02N450HV; IXYS Corporation) switches this output at a frequency of 1,000 Hz to produce a square wave capable of causing electron-hole pair recombination in the ZnS phosphors [66]. A pair of MOSFETs switch the connection to the top electrode of each HLEC between the high voltage signal required for illumination and a low voltage signal used for sensing capacitance. A 32 bit CortexM3 ARM microcontroller (Arduino DUE, SparkFun Electronics) coordinates these operations and records capacitance measurements. A 6,800 mAh 12V lithium polymer battery pack powers the entire system, including a 12 VDC pump (D2028, AIRPO) used to pressurize the membrane without need the need for an external source of compressed air. The electronic schematic for the pressurization subsystem and a schematic for the illumination and sensory subsystems are shown in Fig. 3.3 and 3.4, respectively. We used a variant of this control system (Fig. 3.9) to illuminate the HLEC panels shown in Fig 3.1. To maximize luminance for this device, we control the top and bottom electrodes with independent, out-of-phase high voltage signals. For all other presented devices, we use the simplified electronic system shown in Fig. 3.4 to reduce complexity when integrating capacitive sensing.

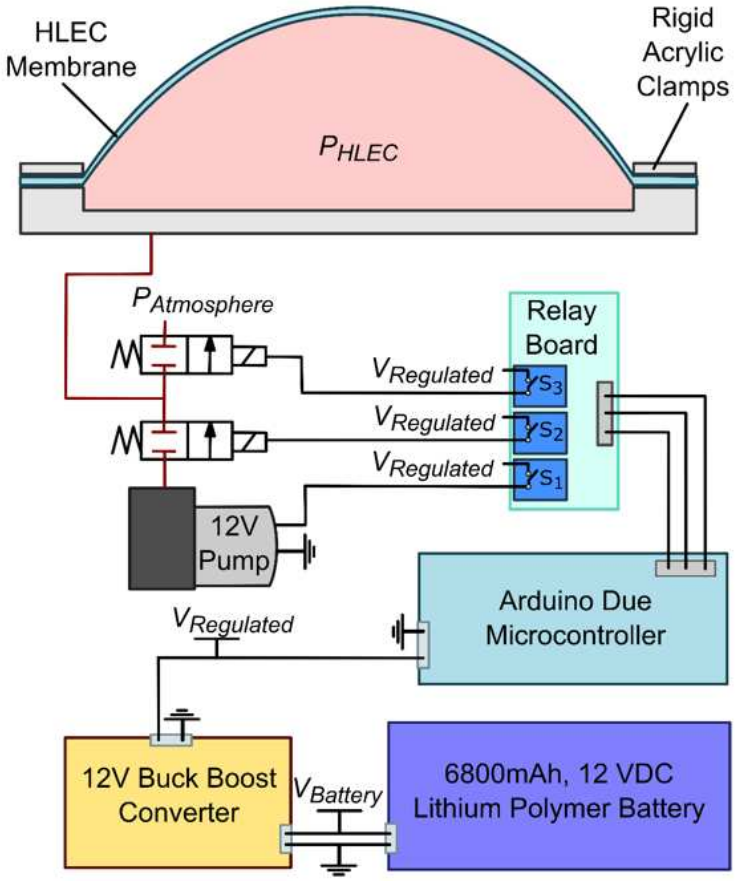

Figure 3.3: **Pneumatic control system for the untethered HLEC interface.** A pair of two-way, normally closed directional valves are used to alternate between inflation using a 12 VDC pump, holding pressure, and venting to the atmosphere.

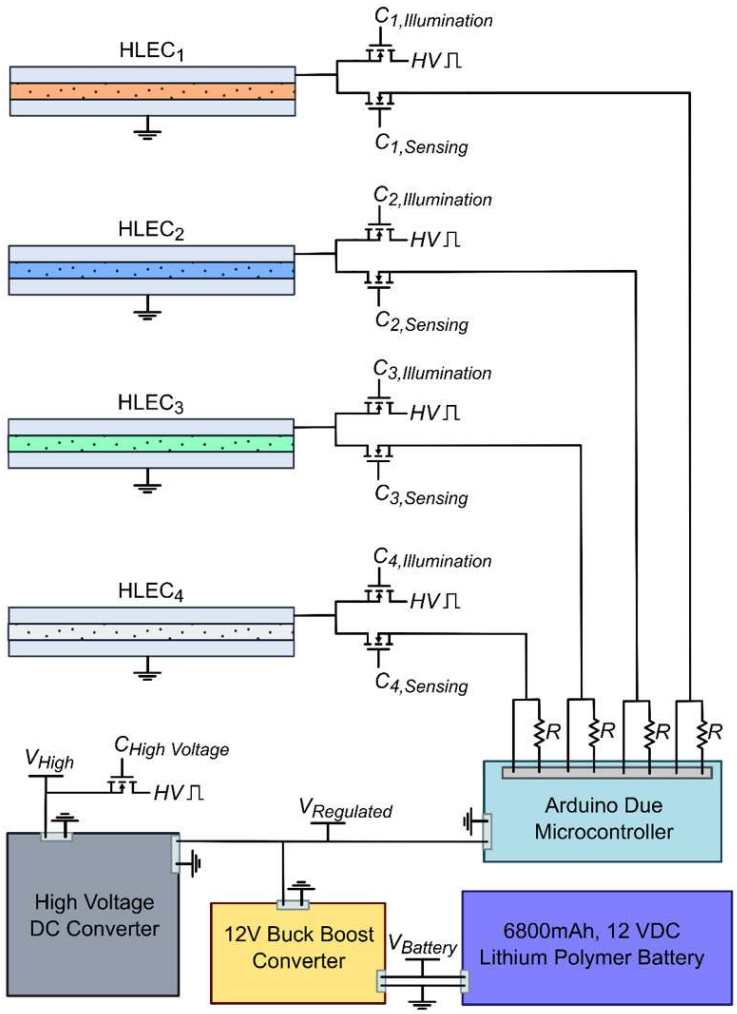

Figure 3.4: **Electronic design for untethered illumination and touch sensing.** One electrode from each HLEC is grounded, while the other is switched between a high voltage square wave for illumination and a low voltage signal for capacitive touch sensing.

3.3.3 Stretch Characterization and Simulation

To characterize extensibility of the membrane, we mounted the composite sheet to a rigid frame as shown in Fig. 3.3. We connected the pressure inlet on the rigid mounting base to a regulated pressure source (Performus VI; Nordson EFD) capable of controlling the relatively low pressure ($\Delta P \geq 10$ kPa) needed to fully

inflate the membrane. As the membrane is inflated, we measured the circumference along the profile of the resulting hemisphere; the resulting stretch ratio ($\lambda = L/L_0$) is included in Fig. 3.5a with intermediate inflation profiles shown in Fig. 3.5b-e. The low elastic modulus of our composite membrane ($E \sim 30$ kPa) [68] enables full inflation with a relatively low actuation pressure ($\Delta P \sim 5.5$ kPa) as shown in Fig. 3.5e. While fully inflated ($\Delta P \sim 5.5$ kPa), the average stretch along the circumference is $\lambda \sim 1.63$, corresponding to a ~166% increase in area.

To simulate the deformation of our device, we developed an FEM model of our composite membrane using AbaqusTM (DASSAULT Systems). We used uniaxial test data [63] to create a material constitutive model for the HLEC that captures the hyperelastic behavior of the composite structure. Our model assumes that the material is isotropic and only experiences plane stresses. We apply the Marlow strain energy potential model to perform the materials curve fit. Due to the large elastic deformations of the HLEC (Fig. 3.5), our model includes nonlinear geometric effects. Our mesh is composed of shell elements with five integration points through the thickness. To compare our FEM model to experimental data, we imposed a fixed boundary condition around the perimeter of the membrane, applied a uniform pressure to the internal surfaces, and recorded the resulting stretch ratio, λ, along the profile. The simulated stretch ratios are shown alongside experimental data in Fig. 3.5a, with a map of vertical displacement, u, overlaid on the inflated profiles in Fig. 3.5b-e. Supplemental Video SV2 shows a simulation of the membrane being inflated.

For low pressures ($\Delta P \leq 4.1$ kPa), the mean percent difference between experimental and numerical stretch ratios is 1.24%. At our maximum pressure ($\Delta P \sim 5.5$ kPa), the percent difference between stretch ratios increases to 5.12%. This deviation is due to two limitations of our FEM model: (i) biaxial effects become

more significant at higher strains, but our model was created using data from uniaxial stretch tests, (ii) our device is composed of four HLEC panels framed by thin sections of silicone, but our model assumes the device is isotropic and uses the composite properties throughout. Future research efforts will focus on developing a higher fidelity material model that includes each layer in the composite structure separately for uniaxial and biaxial stretching.

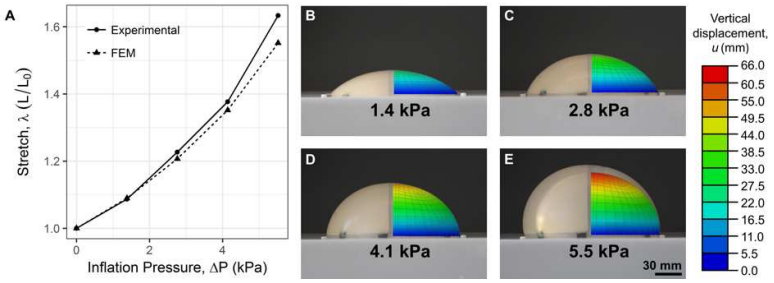

Figure 3.5: **Stretch of the elastomeric membrane during inflation.** (A) Aggregate stretch across the profile of the HLEC membrane as internal pressure is applied. Experimental results are compared to results of a numerical simulation. Profiles of the device are shown alongside vertical displacement, u, for pressures of 1.4 kPa (B), 2.8 kPa (C), 4.1 kPa (D) and 5.5 kPa (E).

3.3.4 Capacitive Touch Sensing

To enable capacitive touch sensing, we isolate the HLECs from high voltage and connect the top electrode of each HLEC to digital input/output (I/O) pins on the microcontroller; we use the microcontroller to measure the increased capacitance across each electrode as a finger approaches. By applying a simple threshold to the relative capacitance of each panel, we were able to identify the touched panel throughout all stages of inflation.

Figure 6a shows a testing sequence in which we press the white, blue, orange and green panels for three consecutive cycles. We apply this sequence and mea-

sure relative capacitance in the unpressurized (Fig. 3.6b) and pressurized (Fig. 3.6c) states. Figures 3.6d,e show the relative capacitance (C/C_0) of each panel during each of these trials. Although more noise is present in the pressurized state, we are still able to correctly detect the pressed panel in all cases. If the relative capacitance of any of the four panels has exceeded a preset threshold ($C/C_0 > 2$), then we identify the panel with the highest relative capacitance as the panel being pressed. The dashed grey line at $C/C_0 = 2$ in Fig. 3.6b,d shows the threshold for detection; the grey, blue, orange and green boxes below the data represent the identified buttons. Fluctuations in the duration of each signal are due to manual timing used for pressing all four panels in sequence.

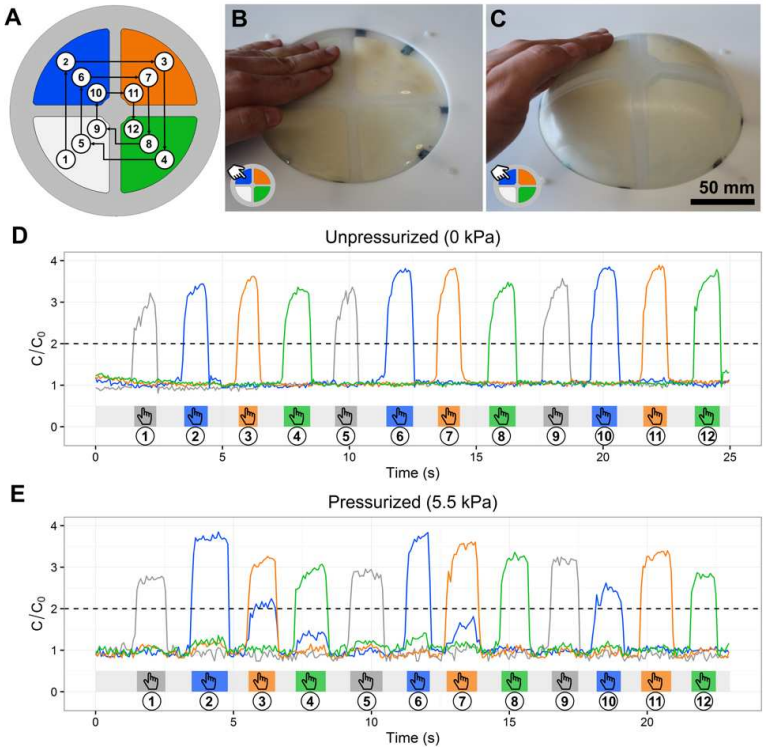

Figure 3.6: **Touch sensing capabilities of the HLEC panels.** (A) Sequence of touches to the HLEC panels, starting with the white panel in the bottom left and proceeding clockwise around the device. A sequence of twelve touches (three per panel) is repeated for the unpressurized and pressurized states. (B) Representative touch on the blue panel in the unpressurized state. (C) Representative touch on the blue panel in the pressurized state. (D) Relative capacitance for each HLEC panel as they are pressed in the unpressurized state. (E) Relative capacitance for each HLEC panel as they are pressed in the pressurized state. The dashed grey lines in (D) and (E) indicate the threshold used to indicate whether a panel has been pressed. The colored rectangles below the capacitance data represent which panel, if any, have been identified as being pressed.

3.3.5 Illumination

As the HLECs are capacitive, their deformation affects the electric field between parallel electrodes: the applied voltage, V, and the dielectric thickness, t, de-

termine the field strength, E (eq. 3.1). Additionally, the elastomers comprising the HLEC membrane can be treated as incompressible and thus we can relate the axial, λ_1, transverse, λ_2, and out-of-plane, λ_3, deformations to one another as $\lambda_1\lambda_2\lambda_3 = 1$. Therefore, as the thickness, $t = \lambda_3 t_0$ (eq. 2), decreases, the area, $A = A_0\lambda_1\lambda_2$ (eq. 3), of the membrane increases. Combining eq.'s 3.1-3.3, we define the field strength across the dielectric layer in terms of the voltage, area, and initial dimensions of the HLEC membrane: $E = (VA)/(A_0 t_0)$. As the light emission from the HLEC is electric field driven, we can modulate the local intensity simply by changing the dimensions of the panel.

When we hold the amplitude and frequency of the voltage source constant and stretch the HLEC, the luminance increases. Figure 3.7a shows the luminance of the blue panel as the HLEC inflates. To measure this increase, we used a luminance meter (SM208; MA Instruments) to collect three measurements at each of the pressures set by an external pressure regulator (Performus VI; Nordson EFD). Throughout an inflation cycle, the luminance of the blue panel increases 354% from 3.47 ± 0.53 cd m^{-2} to 15.74 ± 0.72 cd m^{-2} as the panel stretches with applied pressure (Fig. 3.7a).

Figures 3.7b-c and Supplemental Video SV3 show the anisotropic change in luminance of the single blue panel as a finger deforms the HLEC. We used the MATLAB image processing toolbox to analyze individual frames from a recorded video and determine the relative luminance across the panel. For this task, we first converted the native RGB color space of each image to a YCbCr color space where the three components for each pixel represent relative luminance (Y) and chrominance (Cb and Cr) color values. We then isolated the illuminated region of interest by applying a color-based threshold. For this region of interest, we generated a heat map based on the relative luminance compo-

nent, with brighter areas shown in yellow and darker areas shown in red. The localized increase in luminance as a finger press deforms the panel becomes more pronounced as the finger presses deeper into the membrane.

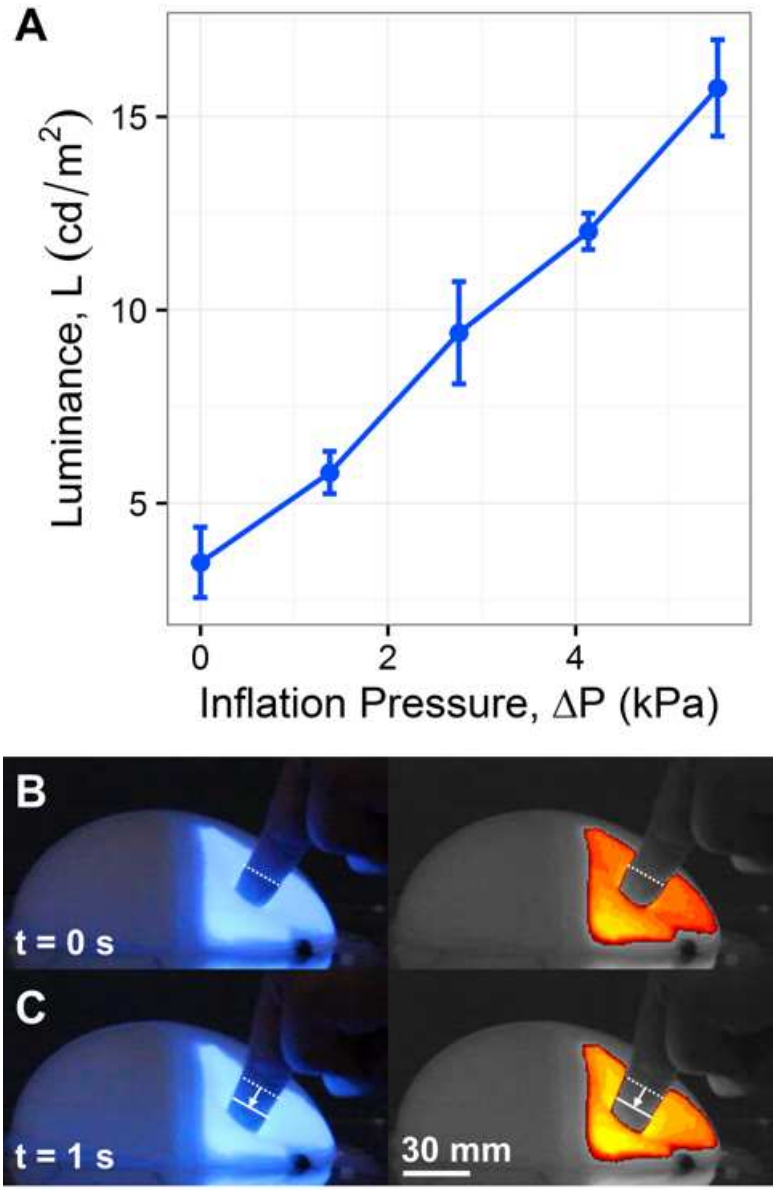

Figure 3.7: **Change in luminance during deformation.** (A) Luminance for the blue panel as the membrane is pressurized. Error bars represent the standard error calculated using three measurements. (B-C) Pressurized HLEC panel being deformed with a finger press while illuminated. The images on the right show the relative luminance of the device, with yellow coloration corresponding to the highest luminance.

3.3.6 Gameplay

Finally, we integrate the sensory and illumination capabilities to create an interactive memory game analogous to the Hasbro game Simon. To play the game, the player must repeat the sequence of illuminated panels in the correct order. After the illumination cycle is complete, the capacitive touch sensors detect whether the player has selected the next panel in the sequence. If the player correctly selects all panels in the sequence, the game adds a randomly generated panel to the sequence and the process repeats. If the player selects the wrong panel or waits too long to provide an input, flashing HLEC panels indicate that the game has ended (Supplemental Video SV4 shows a representative game). In this example, the gameplay lasts for nearly three minutes and the player reaches a sequence of thirteen panels prior to making an error and ending the game. The four different colored panels used for gameplay are shown illuminated in their unpressurized (Fig. 3.8a-d) and pressurized states (Fig. 3.8e-h; Supplemental Video SV5 shows a finger deforming the illuminated panels. To determine the power consumption of our interface, we substitute the lithium polymer battery shown in Fig. 3.3 and 3.4 with a switching DC bench power supply (1550; BK Precision). With a 12 VDC input, we measure a baseline current of 1.04 A that increases to 1.56 A when a panel is illuminated. For a typical game, panels are illuminated 29% of the time, leading to an average power consumption of 14.3 W. Based on these power requirements, we estimate that our 6,800 mAh will provide 5.7 hours of gameplay on a single charge.

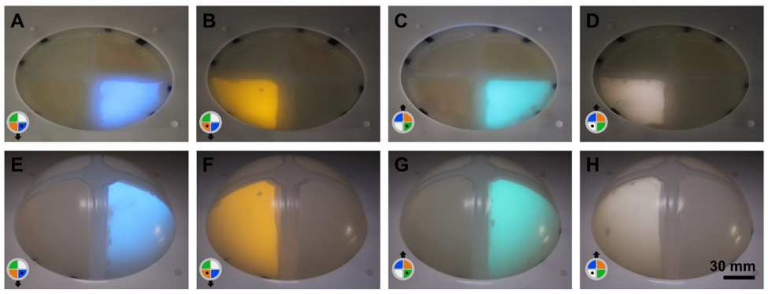

Figure 3.8: **Illumination of the HLEC panels.** Blue (A), orange (B), green (C) and white (D) panels are illuminated while the membrane is uninflated. Blue (E), orange (F), green (G) and white (H) panels are illuminated while the membrane is pressurized to 4.1 kPa.

3.4 Discussion

In this article, we present a portable, battery-powered electronic control system for hyperelastic light emitting capacitors. This portable system stores the HLEC as a flat sheet when not in use and inflates the membrane into a hemisphere for use as a tactile interface. To understand the relationship between physical system states and measurable electrical signals, we characterized the stretch and luminance of the membrane at varying levels of internal pressurization. For sensing touch, we implemented a capacitive sensing method that decouples touch from deformation and we used it to detect button presses using simple thresholding. Through integration of the HLEC array into a soft version of the game Simon®, we demonstrated the combined utility of illumination and touch sensing. With higher resolution patterning of HLECs onto the elastomeric membrane and more complex pneumatic networks, we envision a general-purpose interface that provides flexibility in both visual display and three-dimensional shape.

3.5 Materials and Methods

Materials are selected and prepared according to [63]. Silicone elastomer (Ecoflex 00-30; Smooth-On Inc.) is used for the encapsulation layers and the center dielectric layer. For the center layer, transition metal-doped ZnS phosphors (25 m, 8 % by weight) (Global Tungsten Powders Corp.) are embedded in Ecoflex 00-30 to emit orange (GGL11X), green (GG41X), blue (GGL61X), or white (GGL71X) light when an alternating electric field is applied. The surrounding stretchable electrodes are formed from a polyacrylamide based LiCl hydrogel. These hydrogels are synthesized using acrylamide (AAm, Sigma-Aldrich), polyacrylamide (PAM, M_W 5x10^6) (92560, Sigma-Aldrich), aqueous LiCl (LiCl, Alfa Aesar), crosslinker (N,N'-methylenebisacrylamide, or MBAA, Sigma-Aldrich) and a photoinitiator (Irgacure 1173; BASF). First, AAm and LiCl are dissolved in deionized water at a concentration of 1.75 M and 8 M, respectively. Next, PAM is added with a weight ratio of 0.142 PAM:AAm and the solution is mixed on a magnetic stirrer at 60 °C for 4 hours. Lastly, MBAA and Irgacure 1173 are added at a weight ratio of 0.01 MBAA:AAm and 0.016 Irgacure:AAm. The solution is mixed for two more hours to produce hydrogel precursor that is ready to be molded.

3.5.1 HLEC Materials

Molds for each layer of the HLEC are 3D-printed using an acrylic resin (VeroBlue RGD840, Stratasys Ltd.) with an Objet30 3D printer in glossy mode. The outer encapsulation layers are formed by pouring silicone elastomer (Ecoflex 00-30; Smooth-On Inc.) directly into these molds and curing for 20 minutes at 80°C. The relief patterns in these silicone layers serve as molds for the hydrogel

electrodes. The silicone layers are treated with with UV ozone for 10 minutes prior to pouring the uncured hydrogel. The hydrogel is cured for 15 seconds under UV light (320-500 nm, 200 W) (Model S1500; Lumen Dynamics). Each colored panel in the dielectric layer is molded separately using 3D printed molds (VeroBlue RGD840, Stratasys Ltd.). After curing for 20 minutes at 80°C, the four panels are arranged into a circular mold and silicone (Ecoflex 00-30; Smooth-On Inc.) is poured around the panels to form a dielectric layer with consistent thickness. A thin layer of Ecoflex 00-30 is used to bond all the layers together, forming the stretchable capacitor with a nominal thickness of 5 mm. Carbon conductive grease (846-1P; MG Chemicals) and Cu/Sn plated fabric (Zelt conductive fabric; Mindsets Ltd, UK) are inserted next to the hydrogel tabs protruding from each electrode. Copper tape is applied to the ends of the conductive fabric to provide compliant electrical connections that can be soldered to copper wire.

3.5.2 HLEC Fabrication

Molds for each layer of the HLEC are 3D-printed using an acrylic resin (VeroBlue RGD840, Stratasys Ltd.) with an Objet30 3D printer in glossy mode. The outer encapsulation layers are formed by pouring silicone elastomer (Ecoflex 00-30; Smooth-On Inc.) directly into these molds and curing for 20 minutes at 80°C. The relief patterns in these silicone layers serve as molds for the hydrogel electrodes. The silicone layers are treated with with UV ozone for 10 minutes prior to pouring the uncured hydrogel. The hydrogel is cured it for 15 seconds under UV light (320-500 nm, 200 W) (Model S1500; Lumen Dynamics). Each colored panel in the dielectric layer is molded separately using 3D printed molds (VeroBlue RGD840, Stratasys Ltd.). After curing for 20 minutes at 80°C, the four panels are arranged into a circular mold and silicone (Ecoflex 00-30; Smooth-On

Inc.) is poured around the panels to form a dielectric layer with consistent thickness. A thin layer of Ecoflex 00-30 is used to bond all the layers together, forming the stretchable capacitor with a nominal thickness of 5 mm. Carbon conductive grease (846-1P; MG Chemicals) and Cu/Sn plated fabric (Zelt conductive fabric; Mindsets Ltd, UK) are inserted next to the hydrogel tabs protruding from each electrode. Copper tape is applied to the ends of the conductive fabric to provide compliant electrical connections that can be soldered to copper wire.

3.5.3 Pressure Control for Stretch and Illumination Characterization

The HLEC membrane is mounted to a rigid acrylic frame to measure stretch and illumination at controlled pressures. To ensure that the pressurized chamber is airtight, the outer rim of the HLEC interface is glued to the bottom of the acrylic frame with a one component adhesive (Sil-Poxy, Smooth-On Inc.). Four screws are tightened around the perimeter to clamp the HLEC membrane between the top and bottom frames. A 150 mm diameter circular cutout in the acrylic constrains inflation to the center of the membrane. The outer rim of the HLEC remains unstrained, ensuring that the hydrogel tabs shown in Fig. 3.2a do not break the electrical connections needed for illumination and capacitive sensing. A port in the bottom of the frame uses a barbed fitting an and polyethylene tubing (5181K15, McMaster-Carr) to connect the pressure chamber to a regulated pressure source (Performus VI; Nordson EFD). Due to the small tubing (inner diameter, I.D. $\sim$ 1.6 mm) and low input pressures ($\Delta P < 10$ kPa), we wait at least 30 seconds between pressure changes for the device to reach steady-state prior to measurements.

3.5.4 Capacitive Touch Sensing

To safely measure capacitance of each HELC panel without damaging any of the electronics, we first isolate the electrodes from the high voltage supply and connect the top electrode of each HLEC to digital input/output (I/O) pins on the microcontroller (Arduino DUE, SparkFun Electronics). Grounding the illumination control pins, $C_{n,illumination}$, for each of the four HLEC panels (n = 1,2,3,4) increases the resistance across the drain-source pathways of the illumination MOSFETs, effectively disconnecting the electrodes from the high voltage signal (Fig. 3.4). Subsequently setting the sensing control pins, $C_{n,sensing}$, to high lowers the resistance across the drain-source pathways of the sensing MOSFETS, connecting the hydrogel electrodes to the send and receive pins of the microcontroller. A resistor (R = 100 kΩ) in series with the HLEC electrode forms an RC circuit, where the time constant τ = RC correlates to the time delay between state changes in the send and receive pins. Because the resistance is nearly constant, this delay is proportional to the capacitance across the electrode—as fingers touch the encapsulating silicone, the effective capacitance increases. A calibration step is performed to account for differences in the absolute capacitance of each panel. One hundred measurements are recorded for each panel without any finger presses. The mean of the calibration measurements for each panel is used to define its initial capacitance, C_0.

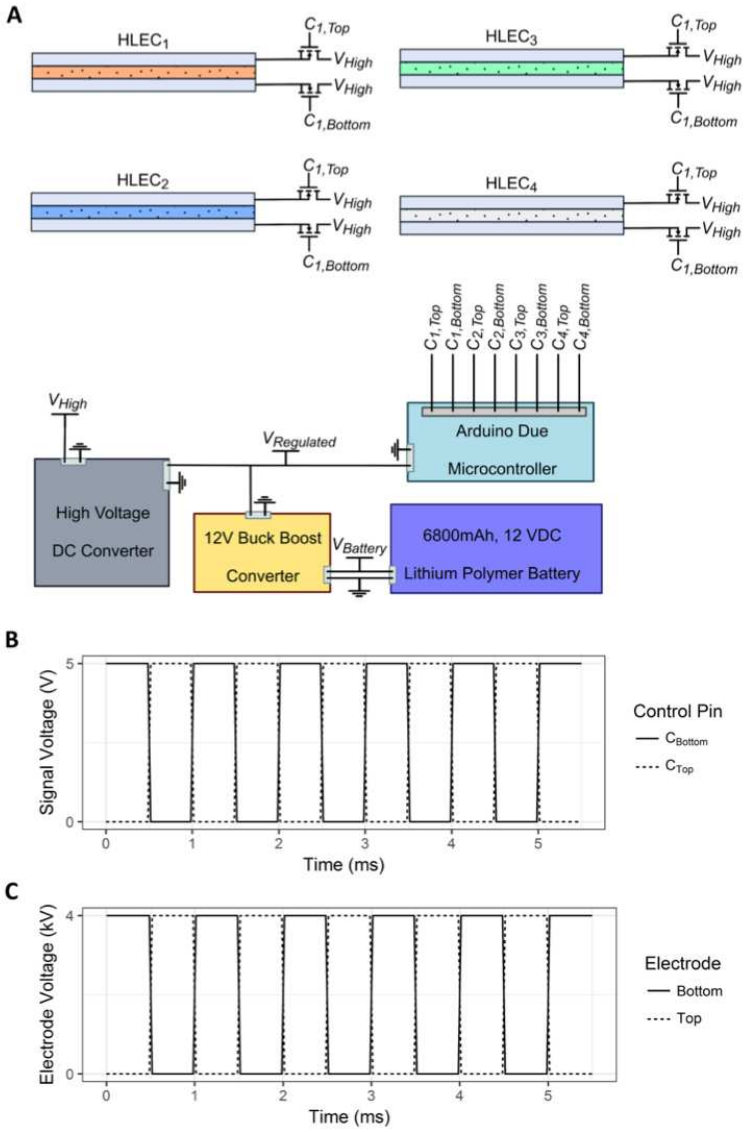

Figure 3.9: **Electronic design for increased illumination.** (A) Both electrodes from each HLEC are connected to independent MOSFETs that can independently switch between high voltage and ground. (B) Nominal signal voltage applied to a bottom and top control pins to illuminate an HLEC panel. (C) Nominal voltage applied to a bottom and top electrodes to illuminate an HLEC panel.

REFERENCES

[48] Glyn Lawson Laura Millen Burnett, Gary and Carl Pickering. Designing touchpad userinterfaces for vehicles: Which tasks are most suitable? *Behaviour Information Technology*, 30.3:403–14, 2011.

[49] Aaron M. Brooks Chiang, Dean P. and David H. Weir. On the highway measures of driver glance behavior with an example automobile navigation system. *Applied Ergonomics*, 35.3:215–23, 2004.

[50] Shigeaki Maruyama Poupyrev, Ivan and Jun Rekimoto. Ambient touch: Designing tactile interfaces for handheld devices. *Proceedings of the 15th Annual ACM Symposium on User Interface Software and Technology - UIST '02*, pages 51–60, 2002.

[51] Catherine Letondal Sylvain Pauchet Vinot, Jean-Luc and Stéphane Chatty. Could tangibility improve the safety of touch-based interaction? *International Conference on Human-Computer Interaction in Aerospace*, pages 8:1–8, 2016.

[52] Aaron D. Mazzeo Robert F. Shepherd Stephen A. Morin Unmukt Gupta Idin Zhalehdoust Sani David Lai Shuichi Takayama Mosadegh, Bobak and George M. Whitesides. Control of soft machines using actuators operated by a braille display. *Lab Chip*, 14.1:189–99, 2014.

[53] Sean Follmer Alex Olwal Leithinger, Daniel and Hiroshi Ishii. Shape displays: Spatial interaction with dynamic physical form. *IEEE Computer Graphics and Applications*, 35.5:5–11, 2015.

[54] Hiroaki Yano Fumitaka Nakaizumi Iwata, Hiroo and Ryo Kawamura. Project feelex: Adding haptic surface to graphics. *Proceedings of the 28th An-*

nual Conference on Computer Graphics and Interactive Techniques - SIGGRAPH '01, pages 469–476, 2001.

[55] Tatsushi Nashida Shigeaki Maruyama Jun Rekimoto Poupyrev, Ivan and Yasufumi Yamaji. Lumen: Interactive visual and shape display for calm computing. *ACM SIGGRAPH 2004 Emerging Technologies - SIGGRAPH '04*, page 17, 2004.

[56] H. Kajimoto K. Vlack D. Sekiguchi N. Kawakami Nakatani, M. and S. Tachi. Control method for a 3d form display with coil-type shape memory alloy. *Proceedings of the 2005 IEEE International Conference on Robotics and Automation*, pages 1332–1337, 2005.

[57] Chris Harrison and Scott E. Hudson. Providing dynamically changeable physical buttons on a visual display. *Proceedings of the 27th International Conference on Human Factors in Computing Systems - CHI 09*, pages 299–308, 2009.

[58] T. Someya Rogers, J. A. and Y. Huang. Materials and mechanics for stretchable electronics. *Science*, 327.5973:1603–607, 2010.

[59] J.-Y. Sun C. C. Foo P. Rothemund G. M. Whitesides Keplinger, C. and Z. Suo. Stretchable, transparent, ionic conductors. *Science*, 341.6149:984–87, 2013.

[60] Christoph Keplinger George M. Whitesides Sun, Jeong-Yun and Zhigang Suo. Ionic skin. *Advanced Materials*, 26.45:7608–614, 2014.

[61] Chaoyi Yan Kenji Jianzhi Chee Wang, Jiangxin and Pooi See Lee. Highly stretchable and self-deformable alternating current electroluminescent devices. *Advanced Materials*, 27.18:2876–882, 2015.

[62] Chaoyi Yan Guofa Cai Mengqi Cui Alice Lee-Sie Eh Wang, Jiangxin and Pooi See Lee. Extremely stretchable electroluminescent devices with ionic conductors. *Advanced Materials*, 28.22:4490–496, 2015.

[63] B. Peele S. Li S. Robinson M. Totaro-L. Beccai B. Mazzolai Larson, C. and R. Shepherd. Highly stretchable electroluminescent skin for optical signaling and tactile sensing. *Science*, 351.6277:1071–074, 2016.

[64] Flurin Stauffer and Klas Tybrandt. Bright stretchable alternating current electroluminescent displays based on high permittivity composites. *Advanced Materials*, 28.33:7200–203, 2016.

[65] Bryan N. Peele Chris M. Larson Huichan Zhao Li, Shuo and Robert F. Shepherd. A stretchable multicolor display and touch interface using photopatterning and transfer printing. *Advanced Materials*, 28.44:9770–775, 2016.

[66] Adrian Kitai. *Luminescent Materials and Applications*, pages 249–268, 2008.

[67] Baohong Chen Feng Xiang Jinxiong Zhou Hong Wang Bai, Yuanyuan and Zhigang Suo. Transparent hydrogel with enhanced water retention capacity by introducing highly hydratable salt. *Applied Physics Letters*, 105.15: 151903, 2014.

[68] Adam A. Stokes Rui M. D. Nunes Shepherd, Robert F. and George M. Whitesides. Soft machines that are resistant to puncture and that self seal. *Advanced Materials*, 25.46:6709–713, 2013.

CHAPTER 4

NEURAL NETWORKS RECOGNIZE HUMAN TOUCH IN SOFT HAPTIC INTERFACES THROUGH DEFORMATION

4.1 Abstract

User interfaces provide an interactive window between physical and virtual environments [69]. A new concept in the field of human-computer interaction is a soft user interface [70, 71]; a stretchable, rubber-like surface that facilitates complex physical interactions through deformation. Despite their potential, these soft surfaces lack a signal processing framework through which we can extract meaning from deformation [72]. Here we present OrbTouch, an inflatable rubber orb with an embedded array of carbon nanotube based capacitive dielectric elastomer sensors, and use it as a communication source. Using a relative entropy statistic [73], we quantify the orb's ability to extract information from its shape. We then use convolutional neural networks to map multivariate capacitance data from highly complex, arbitrary touch gestures to discrete commands and touch locations. We demonstrate these capabilities by using OrbTouch to control the popular game Tetris. Interfacing stretchable sensors with our signal processing layer enables soft media to learn complex, user-specific deformations, laying a foundation for new modes of human computer interaction through shape changing solids.

4.2 Background

The use of compliant touch interfaces is a topic of interest within the field of human computer interaction (HCI) [74] and virtual reality (VR) [75]. Rubber-like

materials, that deform under the force of the human hand, potentially combine the gesture capabilities of capacitive touchscreens [76] with the tactile feedback of physical buttons [4]. The unique advantage of a soft interface is that it has infinite degrees of freedom [77]; it can facilitate complex interactions between a user and her virtual environment that a rigid structure cannot. Physical buttons only occupy binary states, and while touchscreens can sense continuous inputs, they require full visual attention from the user, precluding their use in many common situations where, for example, a user is driving a car [78] or is engaged in a virtual reality environment [75].

While vibrotactile feedback [79] has reached widespread adoption in touch screens and game controllers, it does not replicate the tactile properties of real surfaces. Recent work in microfluidics [80] and soft robotics [72], on the other hand, now supplies us with machinery to modulate the shape [81], appearance [82], and compliance [83] of surfaces using rubber with internal fluidic circuits. Additionally, recent advances in stretchable electronics provide material systems that can be embedded in elastomers. Conductive leads and electrodes, for example, can be made stretchable though the use of carbon nanotube (CNT) films deposited on elastomeric substrates [84, 15]. Similarly, capacitive dielectric elastomer sensors (DESs) have been fabricated using ionic hydrogel conductors as electrodes [14]. Yet, despite these advances, a signal processing framework capable of inferring the shape of an elastomer remains elusive. Whereas rigid interfaces are compatible with a wide range electronic components (e.g., transistors, accelerometers, IMUs, rotary encoders), elastomers have a limited set of sensing modalities (e.g., resistance and capacitance [85], optical loss [10]), and are often prone to noise and hysteresis, making signal processing a significant challenge.

Sensory feedback in soft interfaces, we posit, will require a signal processing framework that can (i) interpret noisy, non-stationary time-series data from stretchable sensors, (ii) dynamically update its internal state to accommodate changes in the system and environment over time, and (iii) learn application- and user-specific inputs. Statistical models are well suited for this set of tasks, particularly in cases where they can learn from large amounts of labeled data. Deep neural networks [86], in particular, exhibit state-of-the-art performance over a broad spectrum of domains ranging from computer vision [87] to speech and text recognition [88]. The benefits of a learning-based approach are that it circumvents the need to program general purpose filters that rely on a physical model of the system, and it enables the device to learn new inputs without being explicitly programmed.

4.3 OrbTouch Design and Fabrication

Here we introduce OrbTouch, an inflatable balloon that can recognize arbitrary touch inputs by learning representations of complex deformations using convolutional neural networks. Its touch interface consists of a pressurized silicone orb with an embedded array of CNT-DES's that are capable of high strains ($\epsilon_{orb} > 100\%$). As a user interacts with the interface, the shapes of the capacitors change, inducing a change in their capacitance, which is captured by a data acquisition system. The rubber orb (Fig. 4.1a) changes it shape continuously from circular (i.e., flat; = 45 mm, P_{orb} = 1 atm) to hemispherical ($P_{orb} \sim 5.5$ kPa). The internal components of the device (Fig. 4.1a) consist of a single board computer, an analog-digital converter (ADC), and an air-compressor. Figure 4.5 shows a schematic of the fluidic circuit used to inflate and deflate the orb; the air compressor is connected to two push-button solenoid valves which enable the user

to perform these functions. The 5×5 sensor array is configured as a passive matrix, with each sensor consisting of a parallel plate capacitor having two blended MWCNT-SWCNT (or CNT) thin film electrodes that are separated by a PDMS dielectric layer (Fig. 4.1b). The electrodes are deposited by aerosol spraying a dispersion of the CNTs in a solution of 2-propanol and toluene. Electrodes are patterned by placing a stencil on the substrate during deposition. To measure the capacitance of each sensor independently, we set one horizontal electrode to +3.3VDC, and monitor the corresponding voltage rise on the opposite electrode (Fig. 4.1c).

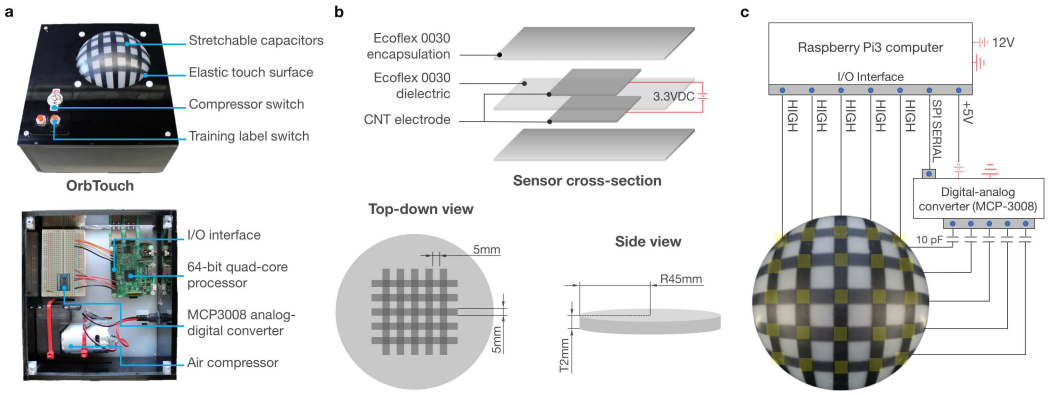

Figure 4.1: **Images and schematic of OrbTouch and its embedded sensor array.** (A) Photograph of the OrbTouch device. Its embedded capacitors capture shape changes caused by human touch. Push-button switches are used to modulate pressure in the orb and label training examples. Bottom: The embedded RBPI3 computer, analog-digital converter (MCP3008), and air compressor used to inflate the orb. (B) Top: a cross-sectional view of the touch interface showing the architecture of our sensors, which consists of upper and lower PDMS encapsulation layers, upper and lower CNT film electrodes, and a 0.5 mm PDMS dielectric layer. Each electrical lead in the passive matrix is 5×55 mm, yielding an overall density of 1 sensor cm^{-2}. (C) Schematic of the drive electronics used to implement real-time capacitance measurements. To measure capacitance, we set one vertical electrode HIGH (+3.3 VDC) at a time, and monitor the induced voltages on the opposite electrodes (i.e., horizontal orientation) using the ADC, which relays the signals to the RBPI3 over SPI serial. During each measurement, there is one pin set HIGH, and one pin that is read; the remaining eight electrodes are connected to ground.

4.4 Device Characterization

4.4.1 Mechanical Properties

To establish OrbTouch as a communication channel, we recall the expression relating the fractional change in capacitance, (denoted z), to the radial stretch,

λ, in an incompressible membrane under equibiaxial tension: $z = \lambda^4$. Figure 4.2a shows a free body diagram of the inflated orb; approximating it as hemi-spheroidal, we express λ^4 as a function of the membrane radius, r, and vertical deflection, d_{def}, to yield the parameterized expression

$$z \approx 4\left(\frac{1}{3} + \frac{2}{3}\left(\frac{d_{def}}{r}\right)^{8/5}\right)^{5/4}. \tag{4.1}$$

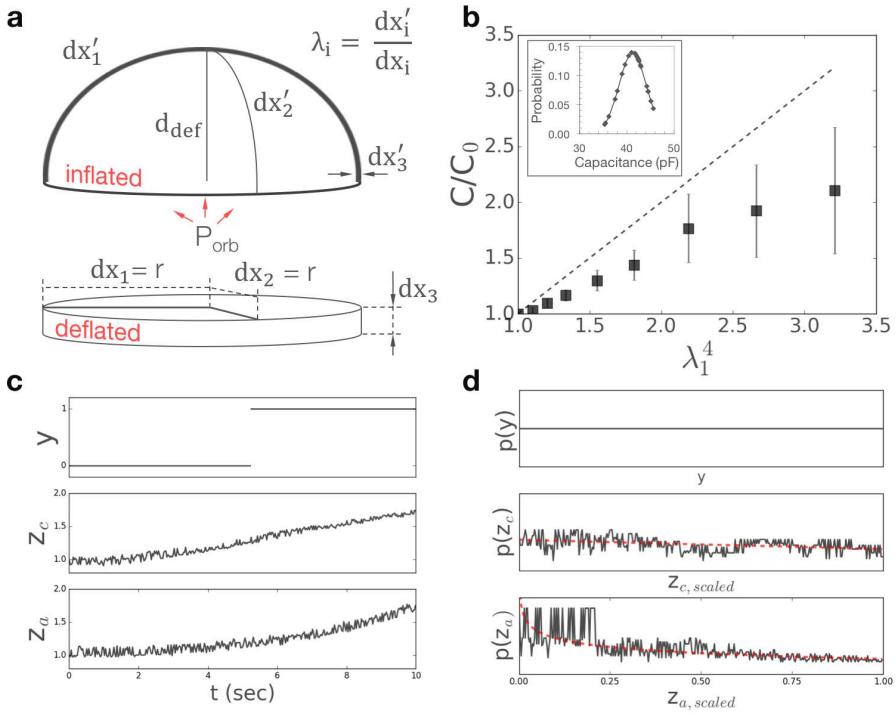

Figure 4.2: **Relationship between deformation, capacitance, and information in the OrbTouch membrane.** (A) Free body diagram of the touch membrane in the undeformed (deflated) and deformed (inflated) states. Under inflation we assume equibiaxial tension ($\lambda_1 = \lambda_2$), and thus, because the membrane is incompressible, its stretch state is fully described by the radial stretch, λ_1. (B) Plot of C/C_0 versus λ_1^4 ($n = 5$). The observed behavior of our DES's undershoot the predicted behavior, but vary monotonically with the quartic stretch. Inset: Plot of the distribution of capacitance values in the undeformed membrane. We observe a mean baseline capacitance of 41.2 pF (SD = 2.9 pF). (C) Time series plots of a binary response variable, (top), and time series z_c (center) and z_a (bottom) under quasi-constant and increasing quartic stretch rates, respectively ($n = 350$). Time series z_c was produced by inflating the membrane at a constant pressure (~7 kPa) over a 10 second interval, while z_a was produced by inflating the membrane at a linearly increasing rate (0 - ~10 kPa) over the same interval. (D) Normalized PMFs of z_c, z_a and y. As an independent variable, y requires an encoding length of 1 bit. Here we discretize our time series into 24 bins. The slight nonlinearity in z_c produces a small information gain of ~0.07 bits, whereas the nonlinear quartic stretch rate is much more evident in the PMF of z_a, yielding an information gain of ~0.22 bits.

4.4.2 Sensor Behavior

Figure 4.2b compares the measured and predicted changes in capacitance versus our parameterized function, $\lambda^4(r, d_{def})$. Tabulated data is provided in Supplementary Table 1. Not unexpectedly, the observed scaling behavior deviates from our prediction. We attribute this to a decrease in dielectric permittivity as the capacitor is stretched [13], and to a lesser degree, our approximation of the orb as a hemispheroid [89]. Importantly, though, the capacitance varies monotonically with lambda4.

4.5 Information Entropy in Deforming Capacitors

Given the established relationship between quartic stretch and capacitance, we hypothesize that information can be encoded in the capacitive signal of a membrane by actively changing its shape. To evaluate this hypothesis, we measure the relative entropy between our capacitive signal and a hypothetical, binary random variable. Figure 4.2c plots capacitive signals corresponding to constant (z_c) and linearly increasing (z_a) quartic stretch rates, $d\lambda_1^4/dt$, along with our response variable, y (these data are tabulated in Supplemental Table 2). Figure 4.2d plots the marginal probability mass functions (PMFs) of their distributions, $p(z_c)$, $p(z_a)$, and $p(\mathrm{y})$. We discretize $p(z_c)$ and $p(z_a)$ by considering a sufficiently large data sample, $n = 350$, and use the mutual information statistic [73], $H(z, y)$, given by

$$H(z, y) = \frac{1}{n^2} \sum_{i=1}^{n} \sum_{j=1}^{n} p(z_i, y_j) \log_2 \left(\frac{p(z_i, y_j)}{p(z_i) p(y_j)} \right) \tag{4.2}$$

to measure the relative entropy between the product of the marginal distribu-

tions, $p(z)p(y)$, and that of the joint distributions, $p(z, y)$. This metric yields the expected decrease in uncertainty of y, or more concretely, the decrease in the number of bits required to encode it, when it is conditioned on our signal, z. We measure relative entropies of $H(z_c, y) = 0.07$ bits and $H(z_a, y) = 0.22$ bits (one bit fully describes the independent variable). Under a purely constant stretch rate, PMF_{zc} would be uniform and thus provide zero information gain; the non-zero information in is due to the slight nonlinearity in its quartic stretch under constant pressure, in addition to the noise in its signal. Most importantly, though, z_a produces a highly non-uniform PMF, which is reflected in its higher relative entropy. This result confirms that time-varying modulations in quartic stretch generate information in stretchable capacitors.

4.6 Learning Latent Representations of Deformation using Convolutional Neural Networks

OrbTouch captures information from arbitrary touches using function approximators, based on convolutional neural networks (CNNs), that learn latent representations of deformation from labeled examples. To demonstrate this, we train a model on a set of touch gestures that we defined for the popular game Tetris; they are a finger-press (translate piece left, right, down), twist-right (rotate piece clockwise), twist-left (rotate piece counterclockwise), and pinch (drop piece to bottom). From these inputs, our predictive model must infer user intent and localize finger touches in order to control the game; we therefore implement two CNNs: (i) an inference network (CNN-G) that maps a stack of 10 input layers (spanning 10 time steps) to a categorical probability distribution, p_g , over 5 classes of touch gestures ($\mathfrak{R}^{5\times5\times10} \rightarrow \mathfrak{R}^5$), and (ii) a regression net-

work (CNN-L) that maps a single input layer to the *x-y* location of a finger-press ($\mathfrak{R}^{5\times5} \rightarrow \mathfrak{R}^2$). Figure 4.3a shows visual representations of networks CNN-G and CNN-L, along with an excerpt from the time series used to train them. Tables 4.1 and 4.2 lists the architectures of networks CNN-G and CNN-L, respectively. We note that potential differences between the user and orb introduce a capacitive component to the sensor signal, however we find that shape changes account for most of the response during touch interaction (see Fig. 4.6). Because the information in a gesture is inherently spatiotemporal, CNN-G convolves a 3D kernel over both the spatial and temporal dimensions of the input to capture relevant features. During gameplay, commands are generated by taking $argmax(p_g)$. In the case of a finger-press, we pass a single sensor layer to our regression network to determine the location of touch, from which the appropriate translation is generated.

Our inference network, CNN-G, was trained by performing each of the five gestures for 10 min at a sampling rate of 10 Hz, labelling the data at each time step. After class-balancing, this yielded a dataset of $n = 1.75\times10^4$ examples. The network parameters were optimized against the categorical cross-entropy loss using the adaptive momentum estimation algorithm (ADAM) [90]. Figure 4.3b shows the training and validation accuracy of CNN-G plotted versus training epoch; we measure a test accuracy of ~97.5% after 3×10^2 epochs of training. To train network CNN-L, a user visually located each sensor on the membrane and pressed it (on, off) for ~30 minutes at irregular intervals, yielding $n = 1\times10^4$ training examples. Network parameters were optimized against the mean-squared error (MSE, mm) using ADAM. Figure 4.3c plots MSE versus training epoch. We observe very low test error, MSE = 0.4 mm, and variance, var = 0.2 mm, after 1.6 $\times10^3$ epochs of training. For simplicity, we report distances with re-

spect to the undeformed membrane that lies in two-dimensions (i.e., its circular state), where the touch surface spans the x-y interval [(0, 0), (4,4)] mm. Thus, for a membrane deflection of , a multiplicative factor of $\pi/2$ provides an approximation of the true error along the curvilinear surface of the orb. Although not precise, this training method produces models that generalize well, and it also offers a simple training protocol that can be implemented without an external measurement tool. Another import aspect of our training pipeline is the number of examples required to yield acceptable performance. To evaluate this, we measure the test performance of each network as a function of training set size. Figures 4.3c and 4.3d show the performance of CNN-G and CNN-L as a function of number of training examples after 3×10^2 and 1.6×10^3 epochs, respectively. We find that both networks exhibit reasonable performance with only ~5,000 training examples, which translates to ~30 min of total training time. The data used to train networks CNN-G and CNN-L are provided in Supplementary Table 3.

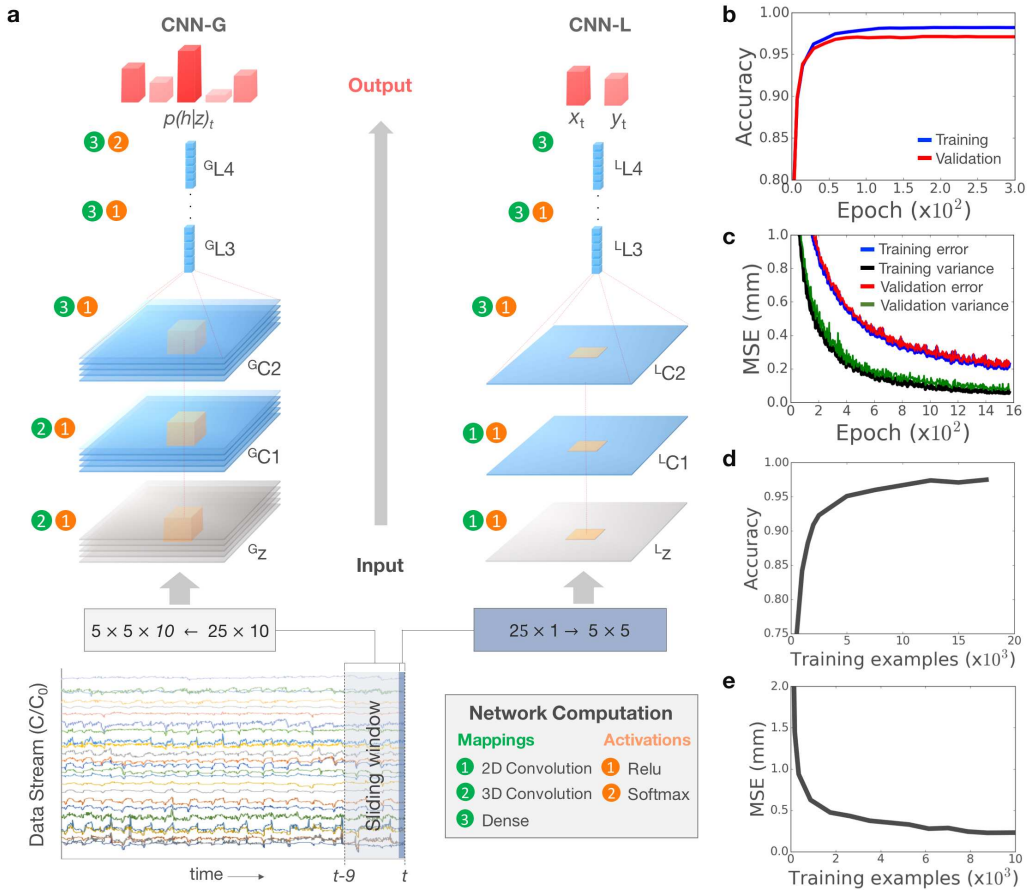

Figure 4.3: **CNN architecture and training results.** (A) Visual representation of our inference (CNN-G) and regression (CNN-L) networks. Tables 4.1 and 4.2 lists the nonlinearities, and number of weights and biases used in each layer of CNN-G and CNN-L, respectively. The plot at the bottom shows an excerpt from a 25-channel time series that was collected at a sampling rate of 10 Hz. Network CNN-G accepts as input a sliding window of ten discrete sensor readings (5×5×10) and outputs a probability distribution over five classes (static, finger press, rotate right, rotate left, and pinch). Network CNN-L accepts as input a 5×5 sensor matrix and outputs a continuous *x*-*y* position. Both networks have two hidden convolutional layers, and two hidden fully connected layer. (B) Plot of binary classification accuracy versus training epoch. We measure a test accuracy of 97.5% after 3×10^2 epochs ($n = 1.75\times10^4$). (C) Plot of the mean squared error of CNN-L and the variance of its residuals with the training labels, both measured in mm, over 1.6×10^3 epochs ($n = 1\times10^4$). (D) Plot of the binary classification accuracy of CNN-G versus number of training examples. (E) Plot of the mean squared error of CNN-L versus number of training examples.

4.7 Using OrbTouch as a Game Controller

To use OrbTouch as a Tetris controller (Fig. 4.4a), we wrote a program that collects sensor measurements, implements our inference and regression networks, and communicates with an external host. The objective of Tetris is to place a random cascade of falling pieces (Tetrominos) into a bounded rectangle without filling it up; filling a row causes the Tetrominos in that row to disappear, allowing the pieces above it to drop and thus preventing the game board from filling. The user uses OrbTouch to translate and rotate the Tetrominos as they fall (Fig. 4.4b). Figure 4.7 provides a detailed description of the gestures that we use to produce these moves. Our software facilitates interaction between the user and the host by storing in memory sensor data from the previous 10 time steps (f = 10Hz), and passing the relevant inputs to CNN-G and CNN-L. The outputs of these models are then passed to a filter that relays commands asynchronously to the host via Bluetooth (Fig. 4.4c). Supplementary Videos 1 and 2 show recordings of the real-time output of OrbTouch, and the Tetris game, respectively.

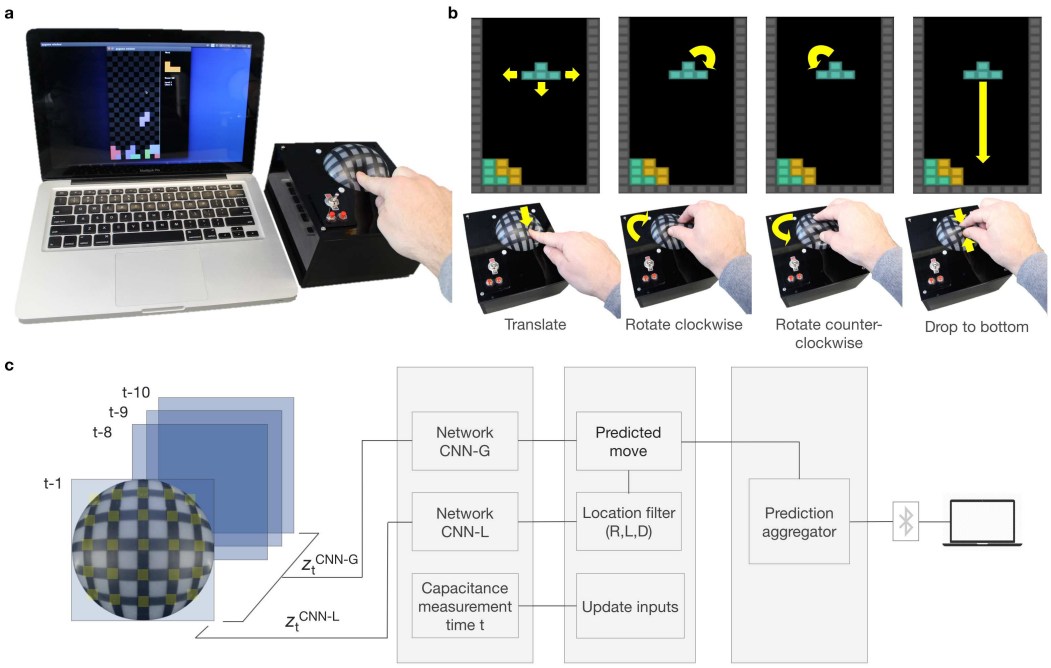

Figure 4.4: **Application of OrbTouch to control the popular game of Tetris.** (A) Photograph of the OrbTouch device being used to control a game of Tetris. (B) Photographs of the four gestures (finger press, twist-right, twist-left, pinch) that are used to produce the six commands required to control Tetris: move right, move down, move left, rotate clockwise, rotate counter-clockwise, and drop to bottom. (C) Diagram of our OrbTouch software implementation. The capacitor array is sampled at 10 Hz. The first processing step parallelizes capacitance measurements and the computation of networks CNN-L and CNN-G. The network outputs are then passed to a second processing step that produce a prediction about the player's intent, in parallel with a separate thread that updates the network inputs for the next time step. In the third step, a simple bouncing algorithm is used to aggregate predictions over time to produce commands, which are sent to the host via Bluetooth. Each cycle of compute take ~86 ± 9 ms; we fix the system latency at 100 ms.

4.8 Conclusions

OrbTouch is comprised of hardware and software that are extensible to a variety of stretchable sensing and soft robotics applications. Our CNN-based processing layer is implemented using fast linear algebra sub-routines [91], while the materials that we use (PDMS, CNTs) are compatible with a variety of scalable fabrication methods. Although OrbTouch was designed with a low number (25) and density (1 cm^{-2}) of sensors, systems of significantly higher complexity could easily be afforded through increases in sensor resolution. Decreasing the CNT electrode thickness to 500 using a commercially available inkjet printer [92], for example, would yield 100 sensors cm^{-2}. In terms of usability, OrbTouch is highly intuitive, and although it required ~1 hr of training for our application, training time could be decreased significantly by using pre-trained networks that have been sensitized to a common set of touch gestures.

By combining the concept of mutual information with a simple model of deformation, we provide theoretic grounds for using a deformable capacitor as a communication channel: the information contained in its signal is directly produced by modulations in its quartic stretch rate, $d(\lambda_1^2\lambda_2^2)/dt$. We further demonstrate that a modular, CNN-based signal processing layer can efficiently learn information from arbitrary deformations produced by human touch. The ability to extract meaning from shape enables a new class of human computer interfaces that learn, and then infer, user-specific touch inputs to a deforming medium. On the basis of this capability, OrbTouch lays a foundation for new modes of interaction in virtual reality, wearables, and other applications that use compliant touch surfaces.

4.9 Supplementary Information

Device fabrication and materials. The internal components of the OrbTouch device consist of a single board computer (Raspberry Pi3; Raspberry Pi Foundation), an analog-digital converter, or ADC (MCP3008; Microchip Corp.), and a 12V DC air-compressor (D2028; AIRPO). Each sensor consists of a parallel plate capacitor with two conductive CNT films separated by a silicone dielectric elastomer layer. Fabrication of the membrane with its embedded sensors is achieved using a multi-step process: (i) in a beaker, a blended mix of MWCNT (P/N 724769; Sigma Aldrich Corp.) and SWCNT (P/N P3-SWNT; Carbon Solutions Inc.) are dispersed in a 90/10 (vol. %) solution of 2-propanol (P/N 278475, Sigma Aldrich Corp.) and toluene (P/N 244511; Sigma Aldrich Corp.) at an overall concentration of 0.05 wt.% using a centrifugal mixer (SR500, Thinky U.S.A. Inc.) in combination with ultrasonic agitation. (ii) A ~0.5 mm layer of silicone rubber (Ecoflex-0030, Smooth-on Corp.) is cast onto an acrylic sheet and cured. (ii) A layer of tape is overlaid onto the substrate and a laser cutter (Zing 24, Epilog Laser Corp.) is used to selectively remove the tape to form the bottom electrode pattern. (iii) The CNT dispersion is sprayed through the mask with an airbrush (eco-17 Airbrush Master, Master Inc.) to form the bottom electrode. Several coats are applied until the leads reach an end-to-end resistance of ~1 kohm. (iv) The mask is then removed and a thin (~0.5 mm) dielectric layer (Ecoflex-0030) is cast over the entire substrate. (v) Steps ii-iv are repeated (in reverse) to form the top half of the membrane (overall thickness ~2.5 mm). (vi) External leads are attached to each of the 10 CNT electrodes and connected to I/O pins on the RBPI3 and ADC.

Capacitance-stretch-deflection scaling law. To characterize the capacitive behavior of our sensors, we recall the scaling law relating capacitance to principle

stretches in a parallel plate capacitor,

$$\frac{C}{C_0} = \lambda_1 \lambda_2 \lambda_3^{-1} \tag{4.3}$$

We impose the condition of incompressibility ($\lambda_1 \lambda_2 \lambda_3 = 1$) and equibiaxial tension ($\lambda_1 = \lambda_2$) to obtain the scaling behavior of a DES shell under inflation,

$$\frac{C}{C_0} = \lambda_1^4 \tag{4.4}$$

There is no known analytic solution relating the radial stretch, λ_1, of an inflated circular shell to its deflection, [89]. Observing that C/C_0 scales with the square of the fractional change in the cross-sectional area of the electrodes, $SA_{orb}/\pi r^2$, here we approximate the orb as a hemispheroid to parameterize the stretch in terms of d_{def}, which we can measure in experiment. The approximate surface area of a hemispheroid is given by

$$SA_{orb} \approx \left[\frac{r^{16/5} + 2(r d_{def})^{8/5}}{3} \right]^{5/8} \tag{4.5}$$

Dividing this expression by the area of the undeformed membrane, πr^2, and taking its square, yields the predicted scaling behavior as a function of the radius and deflection,

$$\frac{C}{C_0} \approx 4\left(\frac{1}{3} + \frac{2}{3}\left(\frac{d_{def}}{r} \right)^{8/5} \right)^{5/4}. \tag{4.6}$$

We use this relation to compare the capacitive response of our sensors to that of the ideal behavior.

Information entropy analysis of deforming capacitors. The mutual information, $H(z, y)$, of two random variables, z and y, is equal to the Kullback-Leibler divergence, $D_{KL}(p(z, y)||p(z)p(y))$, between their marginal and joint probability distributions, and thus measures correlation between their distributions. To establish our membrane as a communication channel, we use this metric to evaluate how predictive our sensors (under known deformations) are of a hypothetical, binary response variable. Given the established relation, $z = \lambda_1^2\lambda_2^2$, and the fact that a gesture modulates this quantity over time, we expect information in our stretchable capacitor to be intimately related to its deformation. To show this, we modulated the quartic stretch rate, $d(\lambda_1^2\lambda_2^2)dt$, and compared the distribution of the data to that of our hypothetical, binary response variable, y. We collected two datasets, each consisting of 350 samples; one corresponded to a constant-pressure inflation (~7 kPa) that yielded a quartic stretch rate of ~0.09 sec^{-1} (z_c), and the other a linearly increasing pressure rate (0 - ~10 kPa) which yielded an estimated quartic stretch rate that increased from 0 to ~0.15 sec^{-1} (z_a). To compute the marginal and joint PMFs, we linearly projected and onto [0, 1], and discretized their values into 24 bins. We then used the marginal and joint PMFs to compute .

Network architecture. Our networks were designed to run on a small CPU (64-bit quad-core, 1.2GHz, 1GB RAM) in real time (10 Hz). Extended Data Tables 1 and 2 list the architectural features (input/output shapes, parameter shapes, nonlinearities) of networks CNN-G and CNN-L, respectively. Both networks have two hidden convolutional hidden layers and two hidden fully connected layers. The computationally intensive step in these networks is the convolutional operation, which can be expressed algebraically as

$$a^l_{mijk} = \sigma(w^l_m * \mathbf{a}^{'l-1} + \mathbf{b}^l_m)_{ijk} \leftarrow \sigma(b^l_m + \Sigma_n \Sigma_q \Sigma_r a^{'l-1}_{i-n,j-q,k-r} w^l_{mnqr}) \tag{4.7}$$

where a^l_{mijk} is the $(i,j)^{th}$ node in the m^{th} feature map in layer l, w^l_m and b^l_m are the convolutional kernel and bias terms corresponding to the m^{th} feature map in layer l, respectively, the operator, *, denotes the convolution between the kernel and its input, and $a^{',l-1}$ is the zero-padded input to layer l. We note that in CNN-L, the time dimension (indexed by k) is singleton. The dense layers following the convolutional layers are mapped using the simple linear transformation,

$$a^l_{mijk} = \sigma(w^l_m * \mathbf{a}^{'l-1} + \mathbf{b}^l_m)_{ijk} \tag{4.8}$$

The relu and softmax nonlinearities of node in a layer with nodes are defined below.

$$\sigma_{Relu}(a_i) = max(0, a_i) \tag{4.9}$$

$$\sigma_{Softmax}(a_i) = \frac{e^{a_i}}{\Sigma^J_{j=1} e^{a_j}} (i = 1, ..., J) \tag{4.10}$$

We designed our inference network to capture spatiotemporal features from the membrane as it changes shape. Network CNN-G accomplishes this by convolving a 3D kernel of size (1×1×2 stride) over the 5510 input layer. We apply relu activations to its interior nodes, and a softmax to its output, yielding a probability distribution, over the gesture classes. In total, network CNN-G contains 2.925×10^3 hidden nodes. Our regression network is designed to map touches to locations; we find that convolving a 2D kernel over a single 5×5 sensor input accomplishes this well. CNN-L applies tanh activations to its interior nodes with

no nonlinearity on the output to yield a continuous *x*-*y* touch location, and has $1.924{\times}10^3$ hidden nodes.

Network training. We trained our inference and regression networks by evaluating their predictions, $h(z)$, against ground truth labels, y, that were produced using the label button on the OrbTouch (Fig. 4.1a). Network CNN-G was optimized against the categorical cross-entropy loss, ℓ_{CE}, with 2-norm regularization applied to its weights. This is shown algebraically below,

$$\ell_{CE}(h(z)) = -\frac{1}{n}\sum_{i=0}^{n}(yln(h(z)) + (1-y)ln(1-h(z))) + \lambda_{CE1}\sum_{l=1}^{2}\sum_{m=0}^{M}\|w_m^l\|_2^2 + \lambda_{CE2}\sum_{l=3}^{5}\|w^l\|_2^2 \tag{4.11}$$

where l indexes the layers in the network, and m indexes the feature maps in layer l. We used mini-batches of $n = 256$, and regularization constants $\lambda_{CE1} = 1.875{\times}10^{-3}$, $\lambda_{CE2} = 5{\times}10^{-5}$. To optimize the parameters in our network we used the stochastic optimization algorithm ADAM [90]. Network CNN-L was optimized against a mean-squared error (MSE), ℓ_{MSE}, with 2-norm regularization applied to its weights.

$$\ell_{MSE}(h(z)) = -\frac{1}{n}\sum_{i=0}^{n}(y-h(z))^2 + \lambda_{MSE1}\sum_{l=1}^{2}\sum_{m=0}^{M}\|w_m^l\|_2^2 + \lambda_{MSE2}\sum_{l=3}^{5}\|w^l\|_2^2 \tag{4.12}$$

We used mini-batches of $n = 128$, and regularization constants $\lambda_{MSE1} = 3{\times}10^{-4}$, $\lambda_{MSE2} = 5{\times}10^{-5}$. To enable the CNN-L to generalize to unseen touches, we added zero-mean Gaussian noise (SD = 0.05 mm) to each ground truth label. We implemented all training in Python on a quad-core CPU (8 GB RAM) using the Tensorflow framework [91].

OrbTouch software. In optimizing OrbTouch for game play, we were presented

with two constraints: (i) minimum acceptable accuracy (i.e., CNN-G model size), and (ii) maximum acceptable latency (i.e., CNN-G compute time). Network CNN-G was designed with balance of predictive power and complexity (computation ~81±9 ms per forward pass). To ensure a constant rate of data ingestion, we set the overall latency to 100 ms, and designed the core functions of the program to run within this time constraint. Figure 4.4c shows a block diagram of our software implementation. The program stores in memory a sliding window of sensor measurements corresponding to data collected over ten time steps (i.e., 1 second of data). Network CNN-G is fed the entire stack, whereas CNN-L looks only at the most recent sensor measurement. The networks are executed in concurrent threads. The network outputs are then fed to a filter that combines them to produce a prediction about the user's intent. A secondary filter is then used to aggregate these predictions over time, applying a bouncing algorithm to produce commands that are sent to the host via Bluetooth. This program was implemented in the c++ programming language.

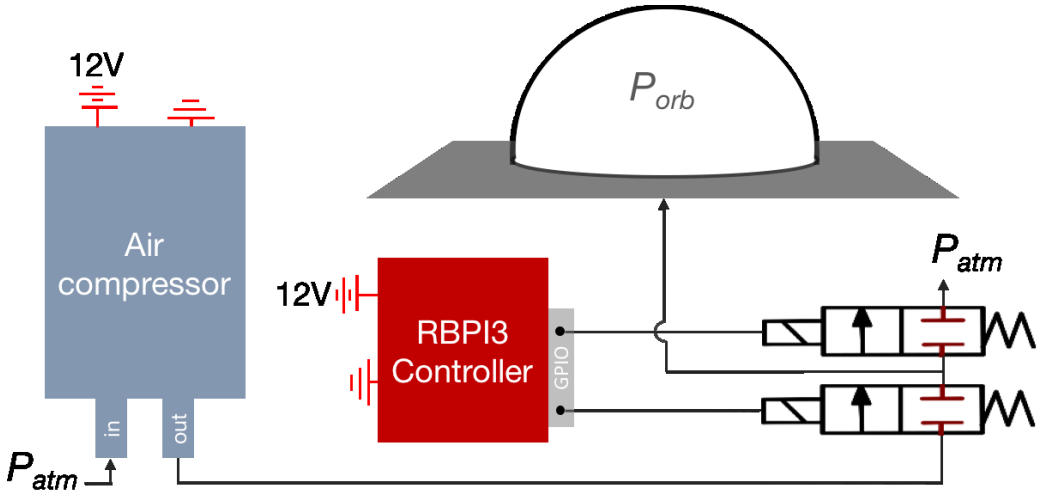

Figure 4.5: **Schematic of the fluidic circuit used to regulate the pressure, Porb, inside the OrbTouch device.** OrbTouch uses an internal air compressor to inflate its soft touch interface. A push button valve is used to allow pressurized air from the compressor into the orb. The valves are powered by the RBPI3, while the air compressor is powered externally.

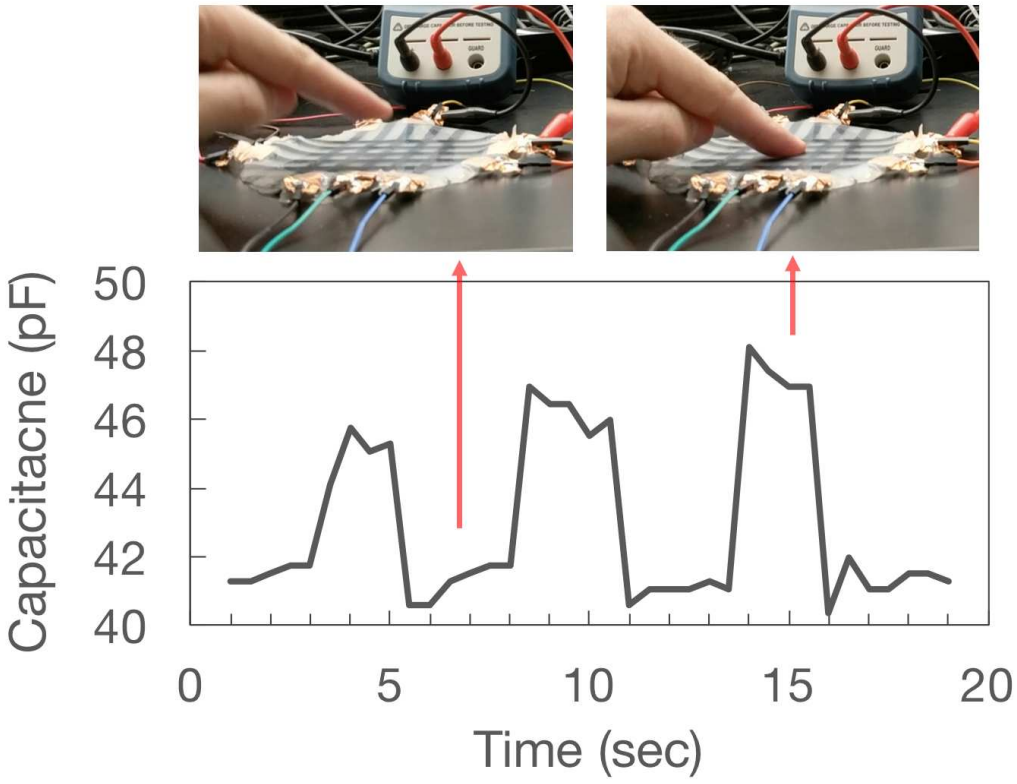

Figure 4.6: **Plot of capacitance versus time as a user lightly touches an undeformed membrane.** Here we press the undeformed touch surface at an interval of ~2.5 sec (on/off), and observe increases of ~4.6 pF (~10.9%) when the surface is touched (with a force similar to what we applied during Tetris; see Supplemental Videos 1 and 2). Comparing this data to our plot of capacitance versus biaxial stretch (Fig. 4.2b) indicates that deformation is primarily responsible for the capacitive response in OrbTouch.

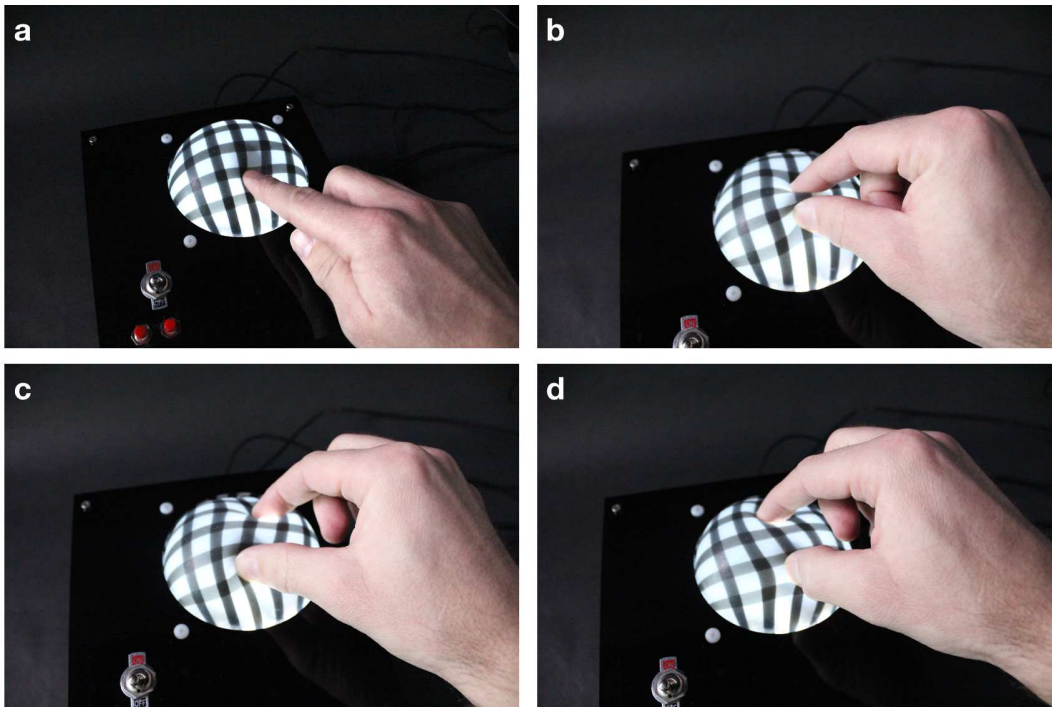

Figure 4.7: **Photographs of four gestures common touch gestures.** We find that four common touch patterns emerge as dominant modes of interaction among different users. (A) A finger press on OrbTouch can be used like finger tracking on a track pad. When network CNN-G infers a finger press, network CNN-L is used to estimate the location of touch. This basic approach could be integrated with application-specific logic to perform a host of common touch functions. For Tetris, we use it to determine the intended direction of translation. (B) Pinching is the second most natural interaction mode. Here we use it as a command to drop the Tetromino directly to the bottom of the grid. (C) A twist-right motion is also very common, especially among right-handed users. Here we use it to rotate the Tetromino 90 deg in the clockwise direction. (D) A twist-left gesture is used to rotate the Tetromino 90 deg in the counterclockwise direction.

Table 4.1: Architecture of neural network CNN-G.

Layer	**Shape**	**Parameters**	**Activation**
Input (${}^{G}z$)	(5, 5, 10)	N/A	N/A
Conv. L1 (${}^{G}C1$)	(3, 3, 5, 25)	$W_1^G \sim (2, 2, 2, 1, 25)$ $b_1^G \sim (25, 1)$	Relu
Conv. L2 (${}^{G}C2$)	(2, 2, 3, 30)	$W_2^G \sim (2, 2, 2, 25, 30)$ $b_2^G \sim (30, 1)$	Relu
Dense L3 (${}^{G}L3$)	(720, 1)	$W_3^G \sim (360, 720)$ $b_3^G \sim (720, 1)$	Relu
Dense L4 (${}^{G}L4$)	(720, 1)	$W_4^G \sim (720, 720)$ $b_4^G \sim (720, 1)$	Relu
Output ($h(z)$)	(5, 1)	$W_5^G \sim (720, 5)$ $b_5^G \sim (5, 1)$	Softmax

Table 4.2: Architecture of neural network CNN-L.

Layer	**Shape**	**Parameters**	**Activation**
Input (${}^{L}z$)	(5, 5)	N/A	N/A
Conv. L1 (${}^{L}C1$)	(4, 4, 36)	$W_1^G \sim (2, 2, 1, 36)$ $b_1^G \sim (36, 1)$	Relu
Conv. L2 (${}^{L}C2$)	(3, 3, 36)	$W_2^G \sim (2, 2, 36, 36)$ $b_2^G \sim (36, 1)$	Relu
Dense L3 (${}^{L}L3$)	(512, 1)	$W_3^G \sim (324, 512)$ $b_3^G \sim (512, 1)$	Relu
Dense L4 (${}^{L}L4$)	(512, 1)	$W_4^G \sim (512, 2)$ $b_4^G \sim (512, 1)$	Relu
Output (x, y)	(2, 1)	$W_5^G \sim (512, 2)$ $b_5^G \sim (2, 1)$	None

REFERENCES

[69] A Dix. *Human-computer interaction*, pages 1327–1331, 2009.

[70] Liu. E Gioscia, R. Soft-user interface feature provided in combination with pressable display surface. *U.S. Patent Application 11/849,133*, August 31, 2007.

[71] Sean Follmer Alex Olwal Hiroshi Ishii Leithinger, Daniel. Shape displays: Spatial interaction with dynamic physical form. *IEEE Computer Graphics and Applications*, 35.5:5–11, 2015.

[72] Tolley M. T. Rus, D. Design, fabrication and control of soft robots. *Nature*, 521(7553):467–475, 2015.

[73] L. Paninski. Estimation of entropy and mutual information. *Neural computation*, 15.6:1191–1253, 2003.

[74] Scott E. Hudson Harrison, Chris. Providing dynamically changeable physical buttons on a visual display. *Proceedings of the 27th International Conference on Human Factors in Computing Systems -200 CHI 09*, pages 299–308, 2009.

[75] Gurocak H. B. Blake, J. Haptic glove with mr brakes for virtual reality. *IEEE/ASME Transactions On Mechatronics*, 14(5):606–615, 2009.

[76] Westerman W. C. Haggerty M. M. Elias, J. G. U.s. patent no. 7,840,912. *Washington, DC: U.S. Patent and Trademark Office*, 2010.

[77] Rahn C. D. Kier W. M. Walker I. D. Trivedi, D. Soft robotics: Biological inspiration, state of the art, and future research. *Applied Bionics and Biomechanics*, 5(3):99–117, 2008.

[78] Glyn Lawson Laura Millen Carl Pickering Burnett, Gary. Designing touchpad user-interfaces for vehicles: Which tasks are most suitable? *Behaviour Information Technology*, 30.3:403–14, 2011.

[79] Astley O. R. Cruz-Hernandez M. Grant D. Robles-De-La-Torre G. Hayward, V. Haptic interfaces and devices. *Sensor Review*, 24(1):16–29, 2004.

[80] G. M. Whitesides. The origins and the future of microfluidics. *Nature*, 442(7101):368–373, 2006.

[81] Ilievski F. Choi-W. Morin S. A. Stokes-A. A.-Mazzeo A. D. Whitesides G. M. Shepherd, R. F. Multigait soft robot. *Proceedings of the National Academy of Sciences*, 108(51):20400–20403, 2011.

[82] Peele B. Li S.-Robinson S. Totaro M. Beccai-L. Shepherd-R. Larson, C. Highly stretchable electroluminescent skin for optical signaling and tactile sensing. *Science*, 351(6277):1071–1074, 2016.

[83] Mac Murray-B. C. Kim J. W.-Robinson S. S. Zou P. X. Silberstein M. N. Shepherd R. F. Van Meerbeek, I. M. Morphing metal and elastomer bicontinuous foams for reversible stiffness, shape memory, and selfhealing soft machines. *Advanced Materials*, 28(14):2801–2806, 2016.

[84] Lee H. W.-Bao Z. Hellstrom, S. L. Polymer-assisted direct deposition of uniform carbon nanotube bundle networks for high performance transparent electrodes. *Acs Nano*, 3(6):423–1430, 2009.

[85] Müller C. Benchirouf A.-Sanli A. Dinh T. N.-Al-Hamry A. Bouhamed A. Kanoun, O. Flexible carbon nanotube films for high performance strain sensors. *Sensors*, 14(6):10042–10071, 2014.

[86] Bengio Y. Hinton G. LeCun, Y. Deep learning. *Nature*, 521(7553):436–444, 2015.

[87] Sutskever I. Hinton G. E. Krizhevsky, A. Imagenet classification with deep convolutional neural networks. *Advances in neural information processing systems*, pages 1097–1105, 2012.

[88] Vinyals O. Le Q. V. Sutskever, I. Sequence to sequence learning with neural networks. *Advances in neural information processing systems*, pages 3104–3112, 2014.

[89] Rivlin R. S. Adkins, J. E. Large elastic deformations of isotropic materials. ix. the deformation of thin shells. *Philosophical Transactions of the Royal Society of London A: Mathematical, Physical and Engineering Sciences*, 244(888): 505–531, 1952.

[90] Jimmy Ba. Kingma, Diederik. Adam: A method for stochastic optimization. *arXiv preprint arXiv:1412.6980*, 2014.

[91] Agarwal A. Barham P. Brevdo E. Chen Z. Citro-C.-Ghemawat S. Abadi, M. Tensorflow: Large-scale machine learning on heterogeneous distributed systems. *arXiv preprint arXiv:1603.04467*, 2016.

[92] Mustonen T. Tóth G. Jantunen H. Lajunen M. Soldano-C.-Ajayan P. M. Kordás, K. Inkjet printing of electrically conductive patterns of carbon nanotubes. *Small*, 2(8-9):1021–1025, 2006.

CHAPTER 5

CONCLUSIONS

This dissertation addresses questions pertaining to how we ought to design, fabricate, and interpret information from deformable interfaces. In Chapters 2 and 3, I focus on design and fabrication strategies to incorporate visual interaction into a deformable touch medium; this work culminated in a new display architecture with enabling mechanical properties. Chapter 4 deals with a more abstract research question: what is the unique advantage (if any) of a deformable user interface? The HCI community uses affordances as a metric to assess the interactive characteristics and usability of a human-centric systems, here I cast the problem in terms of physical quantities, which allows me to use formalism from information theory and statistical machine learning to both quantify and utilize information produced by a deforming touch surface. This ultimately led me the notion of information through deformation, which I used as a guiding principle in the design of OrbTouch.

5.0.1 Summary of Contributions

This work reports advances in stretchable sensors, stretchable displays, user interfaces, and soft robotics. These contributions are summarized below.

A display that can stretch to >500% in uniaxial tension while emitting light. The HLEC display reported in Chapter 2 demonstrates the ability to strain up to 559% in certain portions along its width, with a mean uniaxial strain of 485%. Previous LED-based stretchable displays have been demonstrated ultimate strains of 120%.

A materials system that combines (i) visual display, (ii) capacitance sensing, and (iii) actuation. The capability to monolithically integrate these capabilities into a

single system not only enables deformable, touch sensitive displays (as shown in Chapter 3), but also enables a new class of soft robot that can provide humans with visual cues (as in Chapter 2, Figure 2.4).

An approach to quantify information produced in a deforming solid. Chapter 4 identifies the fundamental mechanism of information production in a deforming capacitor. I first use a simple model of deformation to show that changes in capacitance are proportional to the quartic stretch in the membrane. Capacitance signals from sensors under known deformation are then compared to that of a hypothetical random variable using the mutual information. This result shows very little information is produced in the capacitance signal under constant stretch rates; this is expected given that a constant stretch rate produces (under ideal conditions) uniformly distributed capacitance data. We then go on to show that modulating the quartic stretches produces a significant increase in the information gain, which we expect given its non-uniformly distributed capacitance output.

A soft touch interface that can learn new touch inputs directly from users. OrbTouch demonstrates the ability to learn new inputs from users through labeled training examples. OrbTouch was designed with this function in mind, and has a button that enable the user to do this easily.

A neural network-based signal processing layer for interfacing software applications with stretchable sensors in real-time systems. In soft robotics, a general-purpose sensor filter that enables feedback in a control loop would be broadly enabling; it does not currently exist. Reasons for this are manifold, namely, there is a broad range of sensing modalities currently being explored and they tend to have vary widely in terms of sensitivity, noise, and hysteresis. One of the motivations behind OrbTouch was to address this problem. Although the software that I wrote

was only implemented for the Tetris demo, it was built to be extensible to a wide variety of sensing modalities. The code for this project is hosted on GitHub.

APPENDIX A

A STRETCHABLE MULTICOLOR DISPLAY AND TOUCH INTERFACE USING PHOTOPATTERNING AND TRANSFER PRINTING

A.1 Background

Recent advances in stretchable electronics are attractive for applications ranging from sensory skins for prostheses [93, 94] to stretchable batteries [95, 96] to epidermal healthcare devices [97, 98, 99]. Stretchable light-emitting displays and interfaces, a subclass of stretchable electronics, are important for future devices such as collapsible and expandable flat-panel displays [100], wearable health monitors [101] and in vivo biomedical imaging devices [102, 103]. There are currently two common methods to produce these displays: i) the mechanical structuring of inextensible materials (e.g., silicon wafers) on an elastomeric substrate, and ii) the design of intrinsically extensible materials or composites. The former strategy involves assembling thin films of semiconductors on elastomeric sheets, e.g., poly(dimethylsiloxane) or PDMS, with interconnects patterned into serpentine or buckled ribbons. This strategy enables inorganic light-emitting diodes (ILEDs) to accommodate repeated large strains with high brightness and power efficiencies [104, 97]. The latter one has been demonstrated by organic and polymer light-emitting diodes (OLEDs and PLEDs) [105, 106, 107], light-emitting electrochemical cells (LEECs) [108], and alternating current electroluminescent (ACEL) phosphors [23, 109] integrated with stretchable electrodes. These electrodes use material systems such as ionic transition metal–polymer composites [110], biphasic solid-liquid thin metals films [111], and single-walled carbon nanotubes (SWNTs) or silver nanowires (AgNWs) embedded in a silicone elastomer matrix [105, 107, 112].

We have recently reported a hyperelastic light-emitting capacitor (HLEC) composed of transparent, ionically conductive hydrogel electrodes that sandwich a dielectric layer of silicone elastomer embedded with electroluminescent (EL) ZnS particles to impart a soft robot with the ability to vary its color, and sense both external touch and its own shape change [113]. The light-emitting and touch sensing skin of this robot was fabricated using replica molding and could be stretched up to $\epsilon \approx 480\%$ uniaxial strain, without delamination, at low applied tensile stresses ($\sigma \approx 200$ kPa). Using this technique, we also demonstrated a monochromatic (blue or red) square array of 64 pixels; however, we were not able to pattern individual pixels and incorporate them into a full-color display at sub-centimeter scale resolution using the same method and material system. Here, we present a method of fabricating multicolor hyperelastic light-emitting capacitors (multicolor-HLECs or m-HLECs) capable of biaxial stretching up to $\epsilon_{bi} \approx 200\%$ using photopatterning and transfer printing techniques (process illustrated in Figure A.1a) and demonstrate its use as multipixel color display and multipoint touch sensor (schematic shown in Figure A.1b).

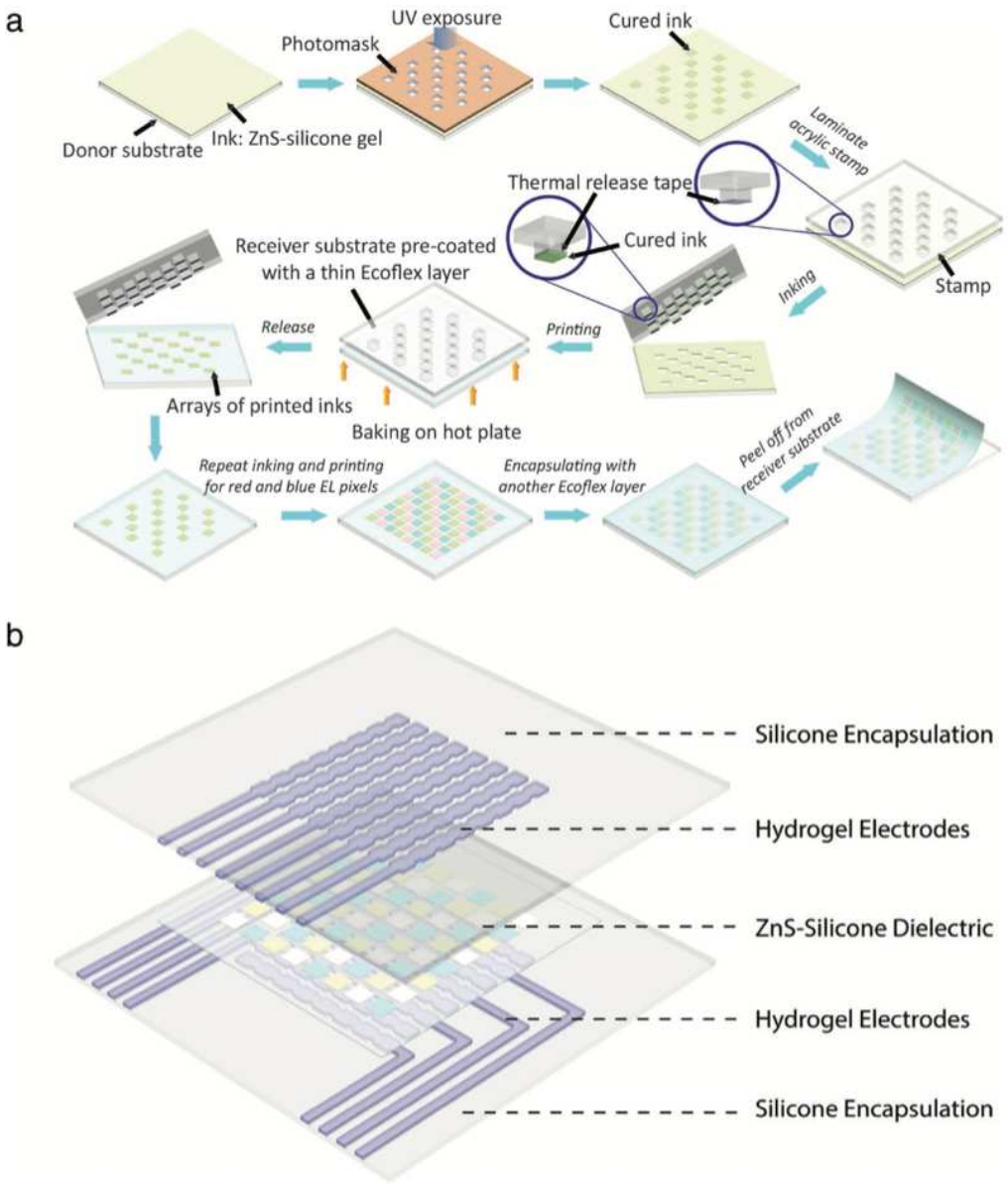

Figure A.1: **Design of the m-HLEC Display.** (A) Schematic illustration of the process ow for photopatterning and transfer printing to form the multicolor electroluminescent dielectric layer. (B) Exploded view of the m-HLEC showing its five layers comprising a 1.3 mm thick EL dielectric layer (ZnS–silicone) that is sandwiched between top and bottom hydrogel electrodes in orthogonal layouts and protected by a silicone encapsulation layer.

A.2 Materials and Fabrication

To make this device, we first premix inks with ZnS phosphor powders (Global Tungsten Powders) and silicone gel (Semicosil, Wacker Chemie AG) and deposit the mixture onto an acrylic donor substrate with subsequent photopatterning into distinct pixels using UV light. Second, we use thermal release tape (Revalpha, Nitto Denko) attached to an acrylic stamp with relief patterns to pick up the cured inks and then print them onto a silicone elastomer (Ecoflex 00-30, Smooth-on Inc.) precoated receiver substrate. Last, we bake the receiver substrate (T = 100 °C, t = 10 min) to release the thermal adhesive and finish delivery of the cured inks. This procedure is repeated three times to integrate the primary color pixels—red, green, and blue—onto one single substrate. The top layer is then encapsulated with more silicone elastomer (Ecoflex 00-30) and this pixelated elastomeric sheet is sandwiched between orthogonal rows of ionically conductive hydrogels also encapsulated within Ecoflex 00-30 (Figure A.1b).

We chose a composite of ZnS–silicone gel–silicone elastomer as the material system for fabricating the light-emitting layer primarily because: i) the ZnS–silicone gel introduces a UV-curing capability for rapid and scalable patterning of stretchable electroluminescent pixels, and ii) the silicone elastomer yields a highly stretchable, tougher matrix that can also bond to the encapsulation layers. Mechanical testing data (Figure A.2a) demonstrates promising adhesion between the layers. The two failure mechanisms are interface delamination and rupture at a strain to failure of $\epsilon \approx 325\%$ with an ultimate tensile strength of $\sigma \approx 289$ kPa.

The photopatterning used for forming this light-emitting layer as depicted in the fabrication procedure abandons some regular steps of photolithography, including photoresist developing and wet etching, because these steps would

cause irreversible swelling of the silicone network [114]. Meanwhile, multiple cycles of transfer printing achieve delivery of the viscoelastic silicone gel onto tougher and more stretchable silicone elastomers in dense configurations over relatively large areas [115]. For the electrodes, we chose the same materials as described in our previous work [111], a LiCl-based polyacrylamide hydrogel that possesses high mechanical toughness, low volatility, high electrical conductivity, and high optical transparency [116].

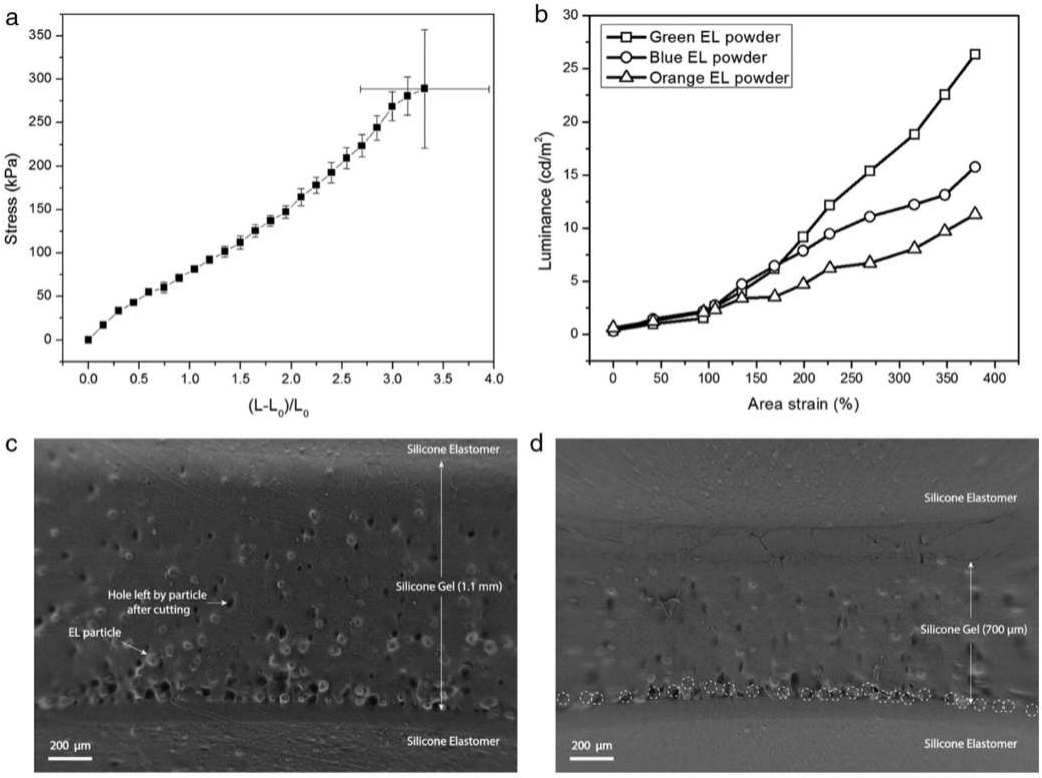

Figure A.2: **m-HLEC Characterization.** a) Stress–strain curve of the ZnS–silicone gel–silicone elastomer composite light-emitting dielectric layer. The nominal stress, σ, is defined as the force applied on the dog-bone shaped composite, divided by the cross-sectional area of the undeformed middle section. b) Luminance of m-HLEC fabricated using three different colored EL phosphor powders in response to area strains. c) Cross-sectional SEM image showing the distribution and morphology of EL particles embedded in silicone gel matrix and encased in silicone elastomer encapsulation for an unstrained sample. d) Cross- sectional SEM image for a uniaxially strained sample. White dotted circles represent the locations of EL particles in the unstrained state.

A.3 Characterization of the m-HLEC Display

A.3.1 Stretch-Luminance Properties

Our assembled display is able to accommodate a large equibiaxial strain up to ≈200% while still emitting light (Figure A.5, Supporting Information). Its luminous intensity during straining increases nonlinearly and depends on: i) the increase in electric field gradient due to the reduction in dielectric layer thickness, and ii) the variation in EL particle concentration due to the expansion in emission area [117]. We measured the strain dependent luminance of our display on a radially folding stretcher [118]. In order to avoid the bias caused by the difference in projected area, we constructed a new display with the same material composition and layer thickness equal to that of the m-HLEC, but with a larger light emission area (≈2.6 cm^2). We mounted and glued this new device to the stretcher and controlled the area strain $\epsilon_{area} = (A – A_0/A_0)$ based on the diameter of the emission area (Figure A.6, Supporting Information). The luminance versus area strain curves demonstrated a monotonic increase for all three colors of EL powders (Figure A.2b).

The increase in emission intensity in response to area strain follows a quasi-linear relationship primarily due to the increase in electric field gradient with stretch. We express the degree of strain by the principal stretches: λ_1, λ_2, and λ_3, which represent the extensions for incompressible materials in axial, transverse, and out-of-plane directions, respectively ($\lambda_1\lambda_2\lambda_3 = 1$). When an equibiaxial force stretches the dielectric to λ times of its original length in planar directions, the thickness of the dielectric scales as $1/\lambda^2$. Thus, we can rewrite the area strain (area) as $\lambda^2 – 1$, and derive the relationship between the relative change in electric field (E/E_0) at constant voltage and the area strain as Equation (1):

$$\frac{E}{E_0} = 1 + \epsilon_{area} \tag{A.1}$$

The resulting enhancement in electric field with strain does not fully account for the increase in luminance with equibiaxial strain. To understand how the microstructural rearrangement of the EL particles during stretching may be assisting in the enhanced light emission, we performed scanning electron microscopy (SEM) on cross sections of unstrained (Figure A.2c) as well as uniaxially strained ($\epsilon \approx 100\%$; Figure A.2d) dielectric sheets. From observation, in the unstrained state, many EL particles tend to form a dense and contiguous monolayer near the bottom surface likely due to a mismatch in density between the particles ($\rho \approx$ g cm^3) and the silicone gel ($\rho \approx 0.97$ g cm^3) matrix. In the uniaxially strained state, although the concentration of EL particles in the bulk appears to decrease, the concentration of particles near the bottom surface (compared to dashed white circles in Figure A.2d) appears to remain constant as particles are pulled to the surface. Therefore, a combined effect of the increase in the electric field gradient due to the reduction in dielectric thickness and the constant number density of particles near the bottom surface during straining, results in an enhancement in light emission. Other factors that might contribute to the nonlinearity of luminance in response to stretching include the dielectric constant of the embedding medium [119] and the optical transmittance of the translucent silicone encapsulations.

A.3.2 Microstructure of the ZnS:Cu-PDMS composite

We also observed in Figure A.2b that the light emission intensity is highly dependent on phosphor powder colors. This effect is more evident at larger

area strains with green powders showing highest luminance, followed by blue, and red-orange showing the lowest. This phenomenon can be explained by the frequency dependence of EL spectra and dopant types. For ZnS:Cu-based green and blue EL powders, there are four emission bands in the green-blue region with different energy levels. At low applied frequencies (for example, in our case, 700 Hz), the emission is dominated by energy levels in the green range [120]. For ZnS:Cu,Mn-based red-orange powders, Mn^{2+} traps holes in the AC field which deteriorates effective electron-hole recombination and therefore lowers the EL efficiency of ZnS:Cu phosphors [121].

A.4 Multiplexed Display

To create a multiplexed display, we used passive matrix electronic addressing to control light emission from each of the 64 pixels using a square array of hydrogel electrodes. When an alternating voltage is applied to one or more of the top electrodes and one or more the bottom electrodes are brought to ground, light is emitted from the intersecting pixels where the electric field is strongest. This method allows us to operate an $m \times n$ matrix using only $m + n$ control inputs; we control all 64 pixels while requiring only 16 relays (Figure A.7, Supporting Information). The passive matrix addressing further allows the m-HLEC to demonstrate dynamic patterns from illuminating a single pixel to displaying more complex shapes with its three-color pixels under various deformation modes such as stretching, wrapping around a finger, folding, rolling, and twisting (Figure A.3, Movie S1 and S2, Supporting Information).

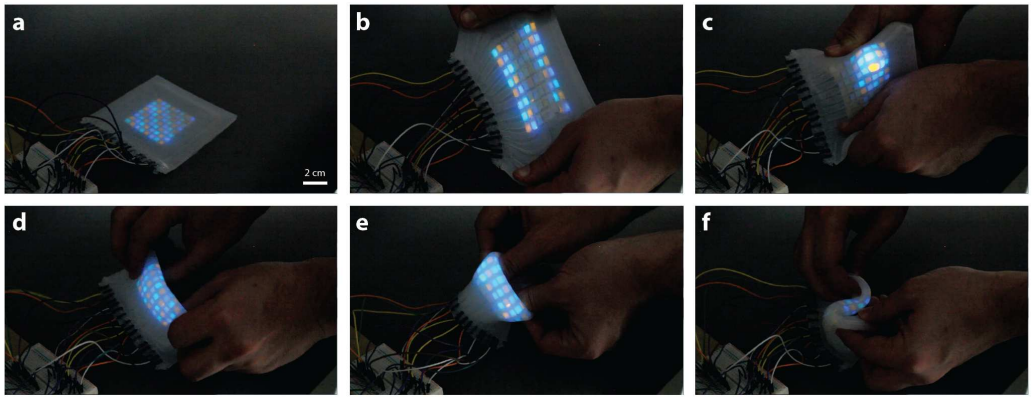

Figure A.3: **Multipixel m-HLEC Device.** m-HLEC showing dynamic patterns under various deformations. a) Illuminating all pixels, undeformed; b) illuminating left and right four columns, stretching; c) illuminating top right corner 5 × 5 pixels, wrapping around a finger; d) illuminating all pixels, folding; e) illuminating middle six columns, rolling; f) illuminating center 4 × 4 pixels, twisting.

A.5 Multitouch Tactile Interaction

In addition to emitting light, the m-HLEC also functions as a multipoint touch sensor using the 64 parallel-plate capacitors formed by orthogonal electrode arrays. We coupled the top and bottom electrodes using two 8-position rotary switches separately, and connected them to a capacitance meter (Figure A.8, Supporting Information). A press (applied uniformly and repeatedly according to details in Supporting Information text) on the capacitor causes compression in both the hydrogel electrodes and the composite dielectric. During the process, we expect an expansion in electrode area (A) and a decrease in distance (d) between the electrodes, and thus a corresponding increase in capacitance ($C \propto Ad^{-1}$) [121]. These touch interfaces report capacitance at 0.1 pF step resolution; for all 64 capacitors we measured capacitance changes at this resolution over a range of 15–20 pF. Figure 4a shows a linear response of the normalized

relative capacitance $(C–C_0)/C_0$ versus the applied force at four randomly selected pixels in the range of 0–4.5 N (per 36 mm^2), equivalent to 0–125 kPa), for both unstrained and strained states ($\epsilon_{area} \approx 200\%$).

In order to characterize the accuracy of our touch interface, we applied touch forces under both unstrained and two strained conditions ($\epsilon_{area} \approx 200\%$ and 200%). Figure A.4b demonstrates topographical maps that indicate normalized relative capacitance change for different states of touch (one, two, and three points of contact) at randomly selected locations under force- controlled compression (3 or 5 N). Using a weighted threshold filter, we were able to identify the exact locations of both single and multitouch inputs (Figure A.4c; Figure A.12 in the Supporting Information for more descriptions of the filter).

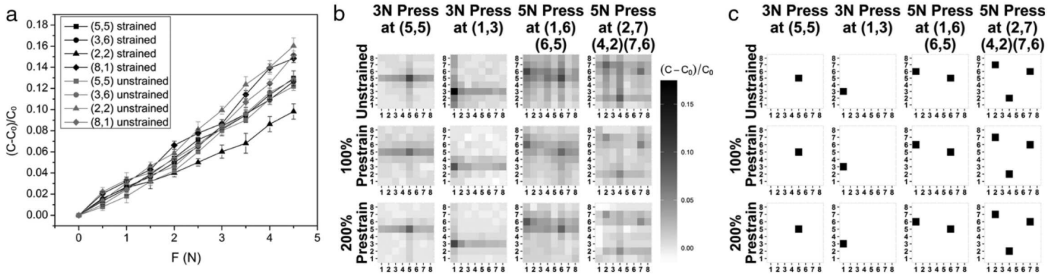

Figure A.4: **Multi-touch Sensing.** Touch sensing capability of the m-HLEC. (A) Normalized relative capacitance in response to applied force at four randomly selected pixels in the range of 0–4.5 N, for both unstrained and strained ($\epsilon_{area} \approx 100\%$) states. (B) Greyscale gradient in the topographical map demonstrates normalized relative capacitance in response to applied force at unstrained and strained ($\epsilon_{area} \approx 100\%$ and 200%) states. (C) Pixels shown in black have been identified as being pressed using a weighted filter that compares the normalized relative capacitance of each pixel to that of its neighbors. The details of the filter are included in the Supporting Information text and the altered response is shown in Figure A.9 in the Supporting Information.

A.6 Conclusion

In conclusion, we have manufactured a m-HLEC with dynamic coloration under area strain up to 200%. The simple fabrication method leverages established techniques, including photopatterning, transfer printing, and soft lithography, offering room for future improvements to yield brighter, higher resolution, and more power efficient multicolor displays. The multitouch sensing capability enabled by the hydrogel parallel plate capacitors at both unstrained and strained states imparts new, potential opportunities to eventually achieve a compliant and expandable touch screen by integrating controllers that can recognize touch and provide feedback to the display components. Meanwhile, we notice that there are still obstacles for the practical implementations of this system; for example, the scaling of the pixel is limited by both the resolution in silicone photopatterning and the dielectric strength of the insulating material. The hydrogel electrodes also confine the electronic control scheme to passive matrix, whereas the more prevalent active matrix addressing requires fully compliant thin film transistors and extensible interconnection wires. Moreover, the ability to increase luminance while decreasing the requirement of input AC voltage remains as a challenging topic for the future research.

A.7 Supplementary Information

Photopatterning. In order to prepare a photocurable ink of silicone, thermosetting (Semicosil 912; Wacker Chemie AG) and UV curing (Elastosil CAT UV; Wacker Chemine AG) silicone elastomer precursor were mixed at a 10:1 ratio by weight. Then transition metal (Cu, Mn, etc.) doped ZnS electroluminescent phosphor powders (Global Tungsten Powders) were added into the mixture

at weight ratio of 1:3 and stirred well. To pattern this ink into a solid-like silicone gel, the mixture was poured on an acrylic donor substrate within a 1 mm thick 3D printed plastic frame (Objet30, Stratasys Ltd.), which also served as support for the photomask (design and dimensions of photomasks shown in Figure A.9, Supporting Information) to avoid direct contact of the photomask with the mixture. After a UV exposure of ≈35 sec, the solution was cured into the pixel configuration for one color.

Transfer Printing. Acrylic sheets were laser cut and assembled (1/8 inch thick; McMaster-Carr) to form the stamp with a relief pattern that corresponds to the pixel configuration. Then double-sided thermal release tape was attached (Revalpha, Nitto Denko) on the tips of the relief pattern. Aligning and pressing this stamp to the ink and quickly peeling back enabled retrieval of the pixels from the donor substrate. After contacting against an Ecoflex 00-30 (Smooth-on Inc.) precoated acrylic receiver substrate, the receiver substrate was placed on a hot plate and baked at 100 °C for 10 min. This procedure allowed the adhesion strength of the thermal release tape to completely vanish, thereby completing the delivery of the pixels to the receiver substrate. Since the thermal release tape serves as a sacrificial interface during the procedure, the acrylic stamp can be reused for multiple transfer printings.

Fabrication of Stretchable Multicolor Electroluminescent Display. Repeating the photopatterning and transfer printing three times and protecting with another layer of Ecoflex encapsulation yielded the multicolor electroluminescent dielectric layer (Figure A.10, Supporting Information). To fabricate the 8-by-8 encapsulation layer and to cast conductive hydrogel electrodes, soft lithography was used. For this process, molds were 3D printed (Objet30, Stratasys Ltd.), filled with Ecoflex 00-30 pre-elastomer, baked in oven at 70 °C for 30 min, and the

cured silicone rubber was demolded. Using these masters, transparent LiCl-polyacrylamide ionically conductive hydrogel was cast under UV exposure after a 10-min UV-ozone treatment to create the surface hydrophilicity. The design and dimensions of the molds are shown in Figure A.11 in the Supporting Information and the synthesis of the hydrogel is described in Supporting Information text.

Characterization of Electroluminescent Dielectric Composite. Tensile test: A uniform layer of ZnS–Semicosil mixture was first UV-cured on Ecoflex 00-30 precoated acrylic substrate, and encapsulated the whole structure in Ecoflex (total thickness 1.3 mm). Then this composite was laser cut into dog bone-shaped specimens and tensile tests (Z010; Zwick Roell) were performed to explore their stretchability. The samples are able to extend to an average uniaxial strain of ϵ = 325% before interface delamination or fracture. SEM: A Keck SEM (LEO 1550 FE-SEM; Zeiss) was used to take cross-sectional images of composite dielectric layer for both unstrained and uniaxially strained states.

Characterization of Multicolor Electroluminescent Display. The luminance versus equibiaxial strain was measured using a screen luminance meter (SM208; MA Instruments). A high-voltage amplifier (610D; TREK Inc.) combined with a function generator was used (3312A; Hewlett Packard) to power the device. The voltage and frequency used for illumination are respectively 2.5 kV and 700 Hz, unless otherwise specified. A custom built radially folding stretcher provides the equibiaxial strain (Figure A.12, Supporting Information).

Control of Passive Matrix Display. Passive matrix addressing was used to control the display shown in Figure A.1b with mechanical relays (SRD- 05VDC-SL-C; Ningbo Songle Relay Co.). As shown in Figure A.7 in the Supporting Information, a high-voltage signal is generated using a high-voltage amplifier (610D;

TREK Inc.) combined with a function generator (3312A; Hewlett Packard). Each of the eight electrodes on the top layer is connected to the high-voltage output when a 5V DC signal is applied to its control relay. Similarly, each of the eight electrodes on the bottom layer is connected to ground when a 5V DC signal is applied to its control relay. The high electric field at the intersections of selected electrodes induces illumination in the m-HLEC pixels. All 16 control relays are operated from a microcontroller (Mega 2560 R3; Arduino), allowing dynamic patterns to be stored and demonstrated on the m-HLEC.

Weighted filter for multi-touch location identification of m-HLEC. A simple filter is applied to identify touch points based on the relative capacitance changes between neighboring pixels. First, the normalized relative capacitance change, $C_{nr} = (C - C_0)/C_0$ is calculated for each pixel, with the results shown in Figure A.4b. In order to generate a clear threshold to identify which pixels are being pressed, a filter is applied to compare the normalized relative capacitance of each pixel to that of its neighbors. This filtered response for each pixel, F_i, is defined as

$$F_i = \sum_{j \in E} w(C_{nr,i} - C_{nr,j})/|E| + \sum_{j \in D} w(C_{nr,i} - C_{nr,j})/|D| \tag{A.2}$$

where Erepresents the set of neighboring pixels that share an edge, D represents the set of neighboring pixels along a diagonal, and w is a weighting constant that can be used to vary the relative influence of edge and diagonal neighbors. The filtered response of the multi-touch capacitance data, using a weighting constant $w = 2.5$, is shown in Figure A.13. Pressed pixels correspond to a filtered response of F > 0.12, and are highlighted in Figure A.4c.

Force and pressure control for multi-touch of m-HLEC. To characterize the capac-

itive touch sensing capability of the m-HLEC, we connected top and bottom hydrogel electrodes to a capacitance meter (830C; BK Precision) via two 8-position rotary switches. The apparatus setup is shown in Figure A.8. Forces for single and multipoint touch are applied by finger pressing and known weight and controlled by a digital balance placed underneath the m-HLEC panel. The applied pressure is also controlled by applying force against an acrylic block(s) (dimensions 6mm×6mm×6mm). To calibrate the 8×8 touch interface, we randomly selected four pixels with coordinates (5,5), (3,6), (2,2), and (8,1) and measured their capacitance change in response to applied force from 0 to 4.5 N with an interval of 0.5 N. This process was repeated under equibiaxially strained ($\epsilon_{area} \approx$ 100%) state. To explore the multipoint touch sensing, we chose three different strain states: unstrained, 100% area strained, and 200% area strained; for each state, we applied one point (two different locations with coordinates (5,5) and (1,3)), two points (with coordinates (1,6), (6,5)), and three points (with coordinates (2,7), (4,2), (7,6)) of touching force using the same method as described above.

Synthesis of the LiCl based polyacrylamide hydrogel for transparent electrodes. 1.75 M of acrylamide (AAm, Sigma-Aldrich) is dissolved in deionized water with 8 M of LiCl (Alfa Aesar) and polyacrylamide (PAM, $M_W \approx 5 \times 10^6$, Sigma-Aldrich) at weight ratio of 0.142 PAM: AAm. The solution is mixed thoroughly on magnetic stirrer hotplate at 500 rpm and 60°C for 4 hours. Then, small amount (0.1% of solution) of a crosslinker (N, N' methylenebisacrylamide, Sigma-Aldrich) and a photo-initiator (Irgacure 1173, BASF; 0.3% of solution) are added to the solution and mixed for two additional hours to yield the uncured hydrogel.

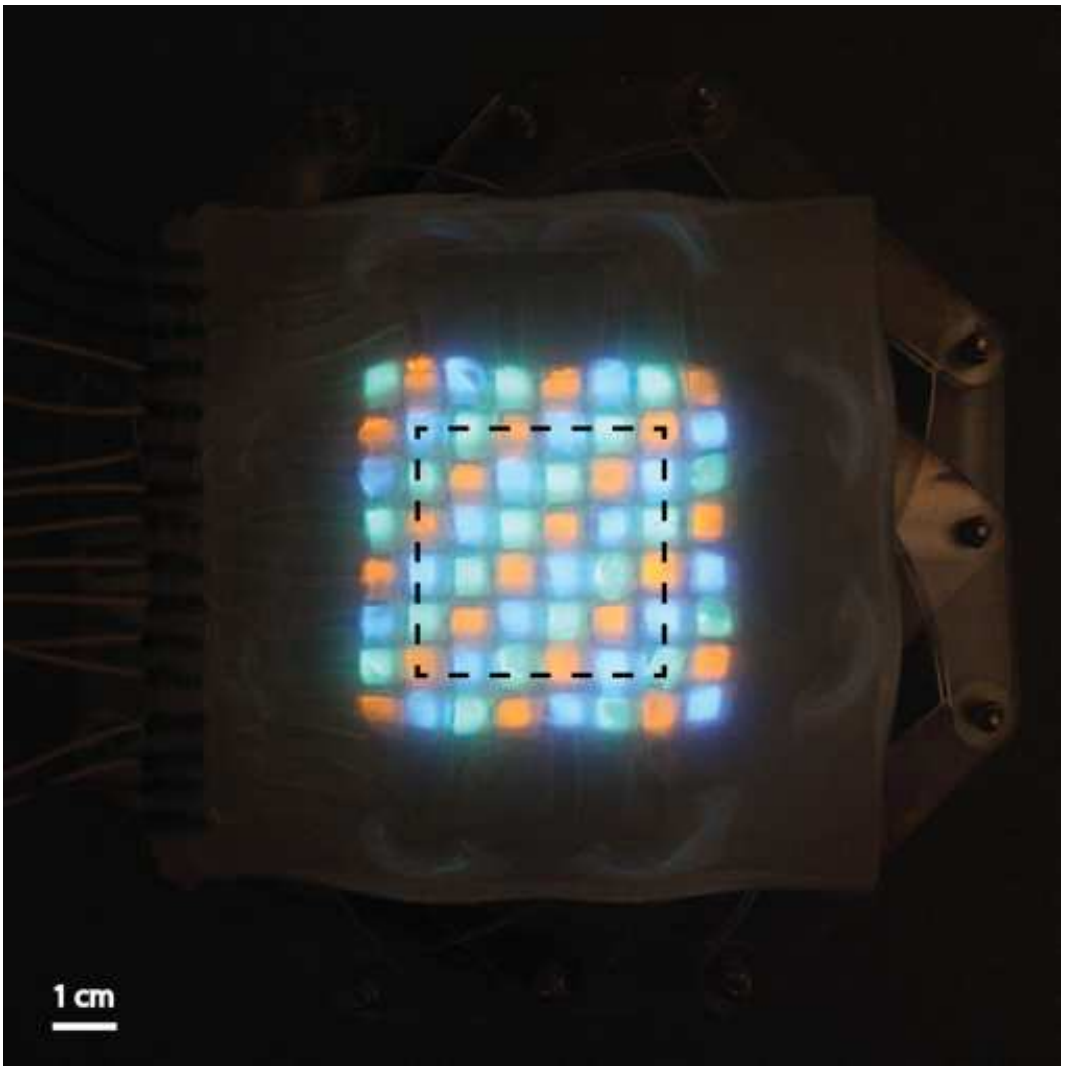

Figure A.5: **Photograph of the m-HLEC being stretched to 200% area strain under equibiaxial strain with a radially folding stretcher.** The black dotted square indicates the area of the light emission at unstrained state. The area strain is determined by the strain gauge/linkage (not shown in the figure; =1.8 in this case). The actual area expansion per pixel is from 21.4 mm^2 to 44.6 mm^2 (~108% area strain).

Figure A.6: **Luminance measurement apparatus.** The luminance versus area strain for three different colored EL phosphors shown in Figure A.2b.

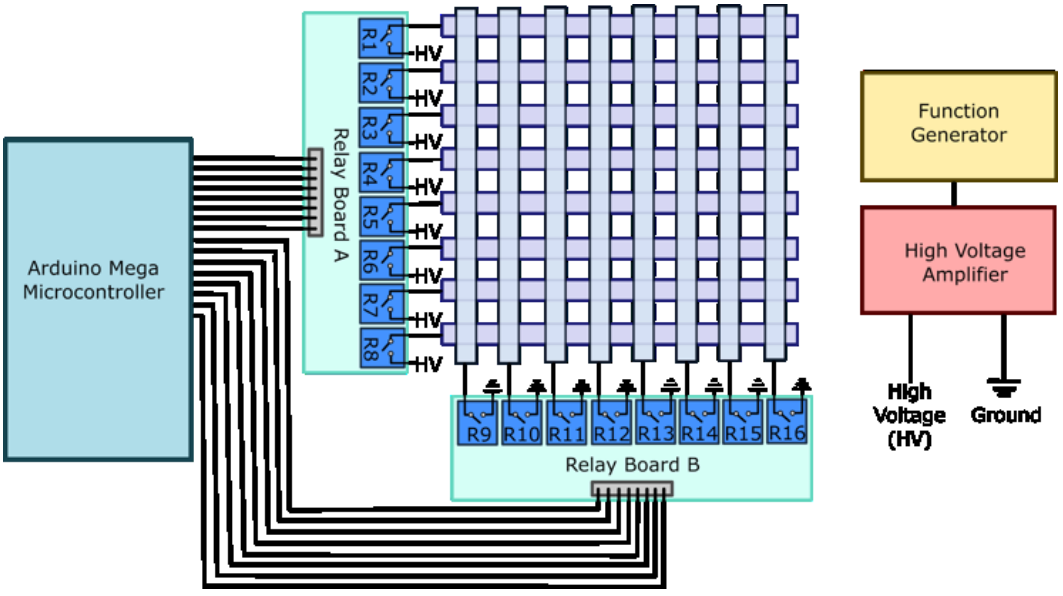

Figure A.7: **Electronic system used to control the passive matrix display.**

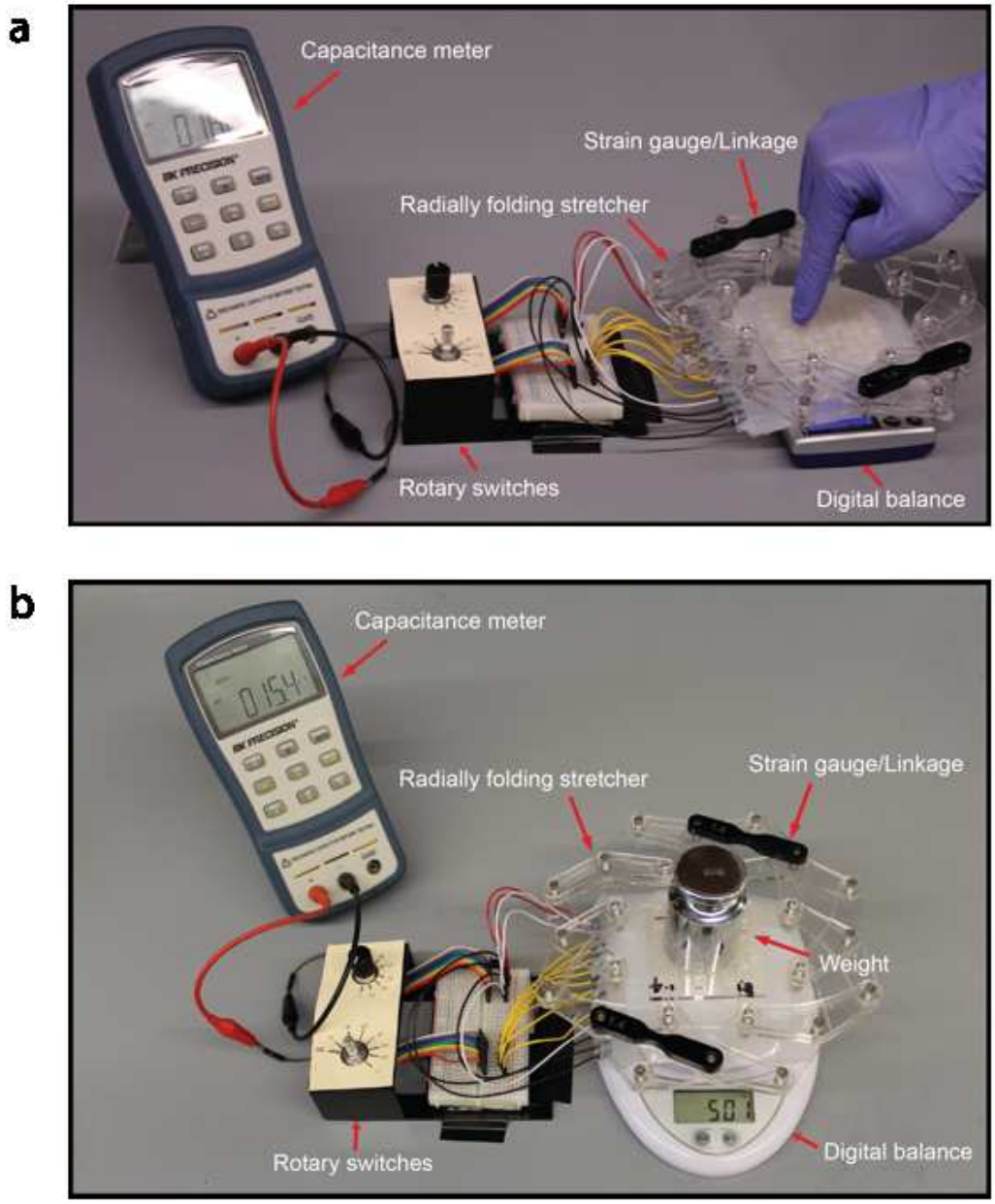

Figure A.8: **Capacitance measurement apparatus.** Setup to measure the capacitance versus applied force under unstrained or equibiaxially strained states as shown in Figure A.4a,b. (a) Single point touch is achieved by pressing on the top of pixels against an acrylic block. (b) Multipoint touch is achieved by placing a weight on the top of an acrylic table that has legs standing on two or three pixels.

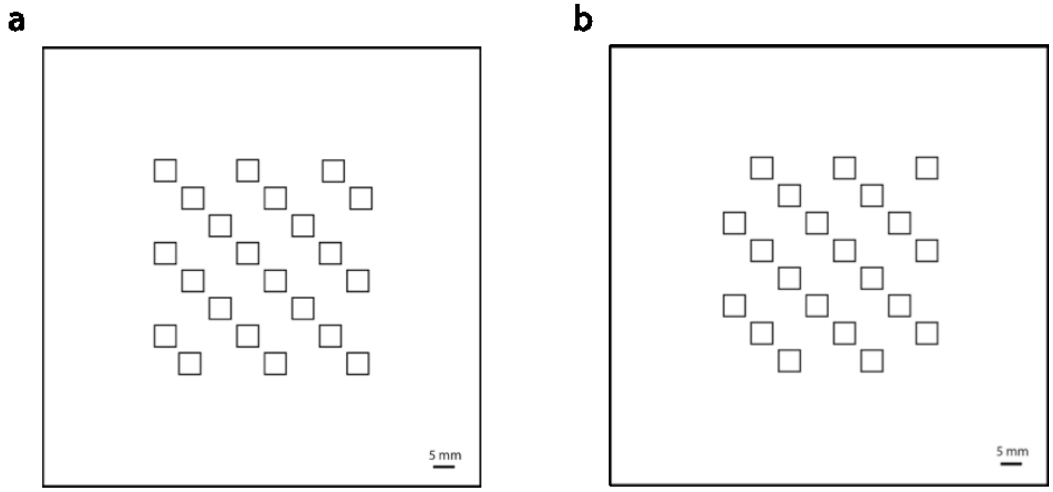

Figure A.9: **A schematic drawing showing the design and dimensions of the photomasks.** (a) Photomask for red pixels. (b) Photomask for blue and green pixels.

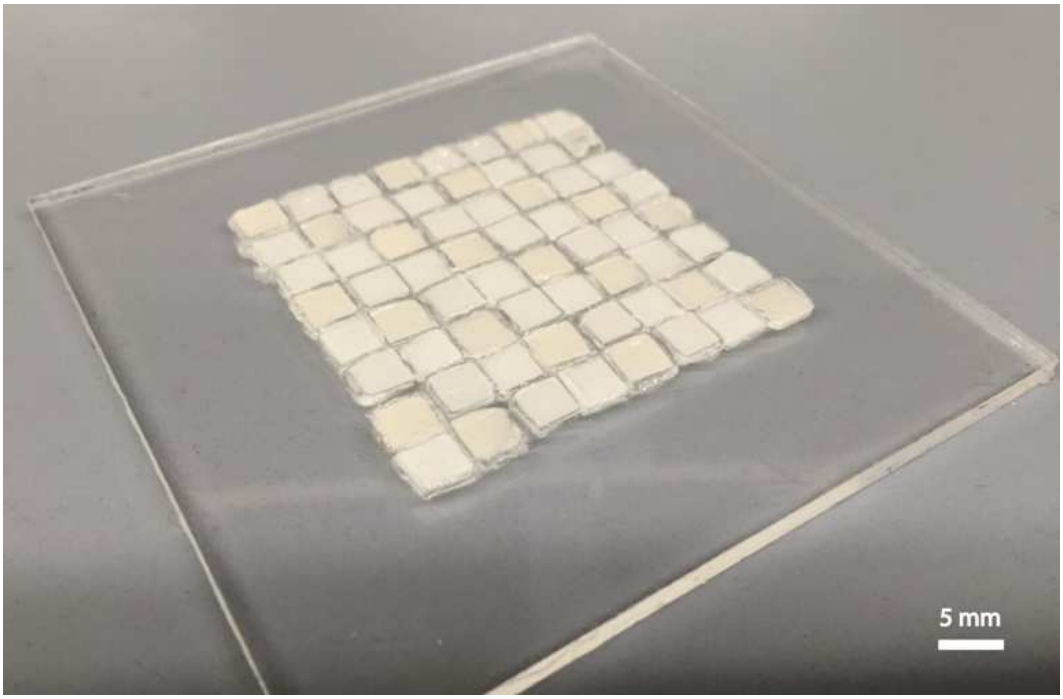

Figure A.10: **A photograph showing the multicolor electroluminescent dielectric layer fabricated via photopatterning and transfer printing.**

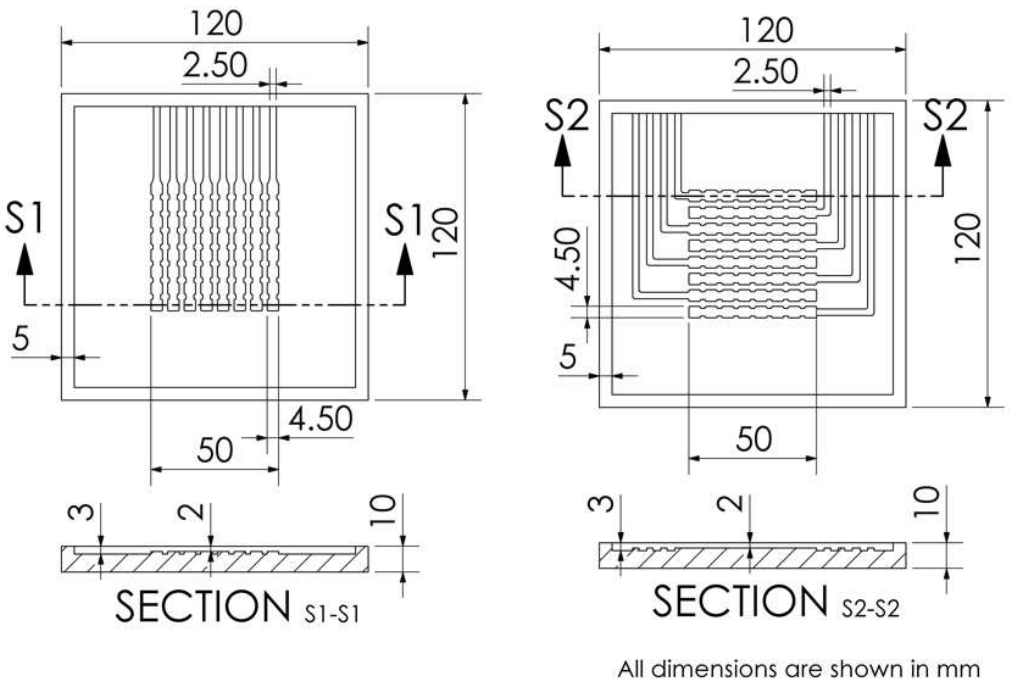

Figure A.11: **Schematic showing the design and dimensions of the 3D printed molds for molding top and bottom Ecoflex 00-30 silicone encapsulation masters.** These masters are later used for casting hydrogel electrodes.

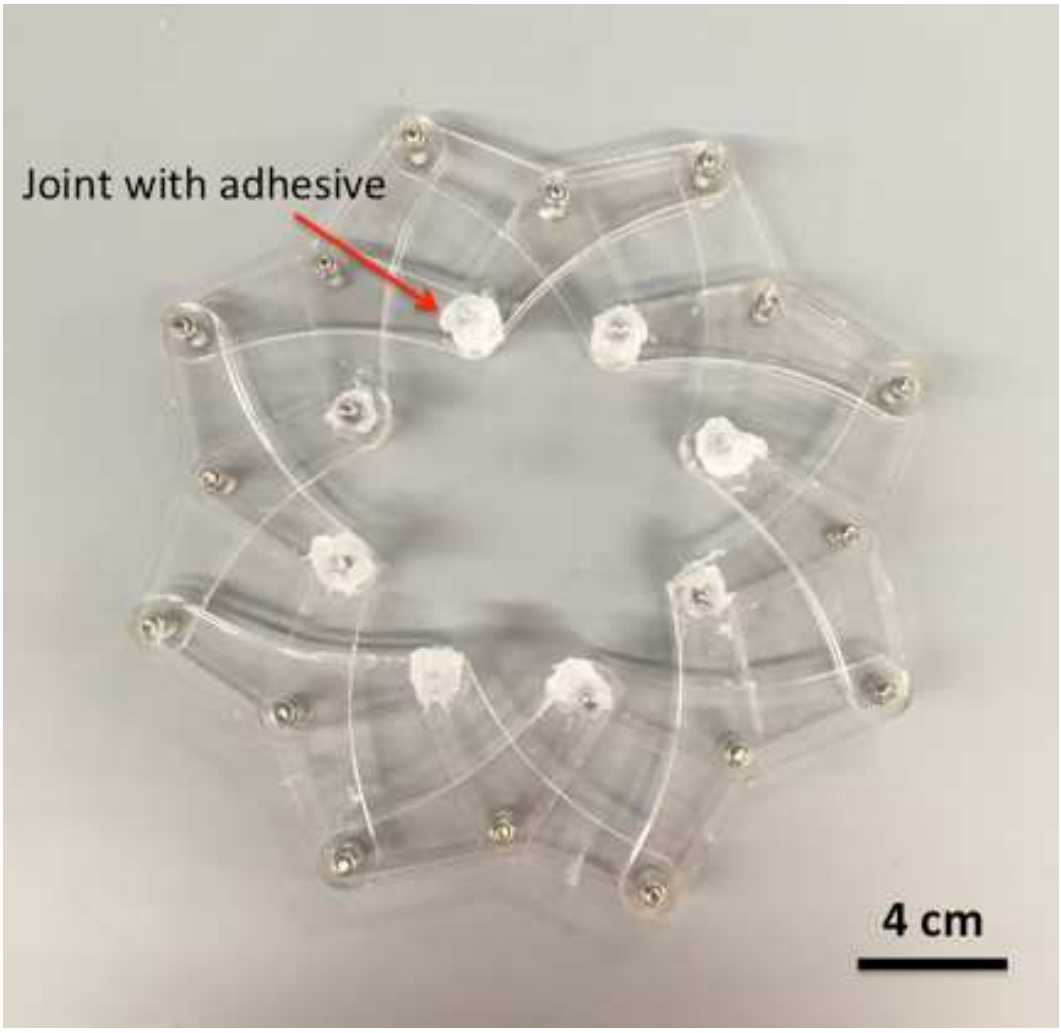

Figure A.12: **A photograph of the radially folding stretcher made of acrylic and metal joints.** The m-HLEC can be coupled to the inner joints using silicone adhesives (Silpoxy, Smooth-on Inc.). A radial tensile force is required to generate a uniform equibiaxial strain to the device.

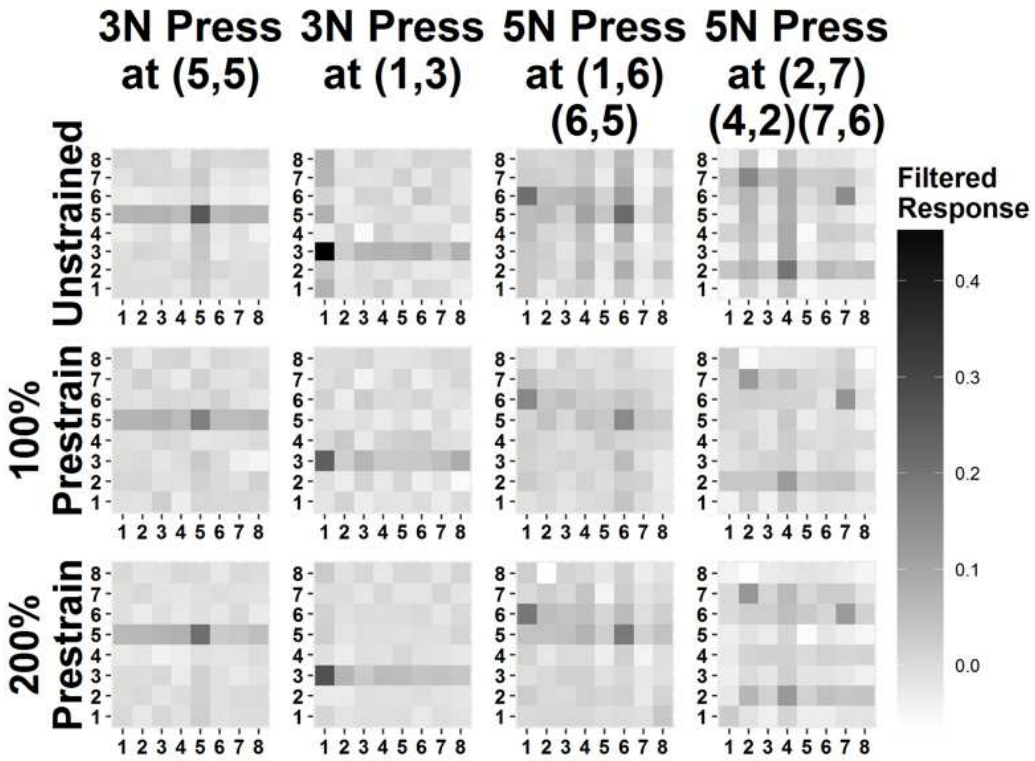

Figure A.13: **A weighted filter is applied to multitouch capacitance measurements from Figure A.4b to create a clear threshold for identifying press locations.**

REFERENCES

[93] H. J. Shim R. Ghaffari H. R. Cho D. Son Y. H. Jung M. Soh C. Choi S. Jung K. Chu D. Jeon S.-T. Lee J. H. Kim S. H. Choi T. Hyeon D.-H. Kim J. Kim, M. Lee. *Nat. Commun.*, 5:5747, 2014.

[94] A. Berndt A. K. Nguyen A. Tom A. McGuire Z. C. Lin K. Tien W.-G. Bae H. Wang P. Mei H.-H. Chou B. Cui K. Deisseroth T. N. Ng Z. Bao B. C.-K. Tee, A. Chortos. *Science*, 350:313, 2015.

[95] J. Cho J. Lee X. Huang L. Jia J. a Fan Y. Su J. Su H. Zhang-H. Cheng B. Lu C. Yu C. Chuang T.-I. Kim T. Song K. Shigeta S. Kang C. Dagdeviren I. Petrov-P. V. Braun Y. Huang U. Paik J. A. Rogers S. Xu, Y. Zhang. *Nat. Commun.*, 4:1543, 2013.

[96] C. Lv Y. An M. Liang T. Ma D. He Y.-J. Zheng S.-Q. Huang H. Yu H. Jiang Z. Song, X. Wang. *Sci. Rep.*, 5:10988, 2015.

[97] R. Ma Y.-S. Kim R.-H. Kim S. Wang-J. Wu S. M. Won H. Tao A. Islam K. J. Yu T. Kim R. Chowdhury M. Ying L. Xu M. Li H.-J. Chung H. Keum-M. McCormick P. Liu Y.-W. Zhang F. G. Omenetto Y. Huang T. Coleman J. A. Rogers D.-H. Kim, N. Lu. *Science*, 333:838, 2011.

[98] A. Akhtar-J. J. S. Norton Y. J. Kwack-S. Li S. Y. Jung Y. Su W. Lee J. Xia H. Cheng Y. Huang W. S. Choi T. Bretl J. A. Rogers J. W. Jeong, W. H. Yeo. *Adv. Mater.*, 25:6839, 2013.

[99] A. Behnaz-Y. Zhang K. J. Yu H. Cheng-M. Shi Z. Bian Z. Liu Y.-S. Kim W.-H. Yeo J. S. Park J. Song Y. Li Y. Huang A. M. Gorbach J. A. Rogers R. C. Webb, A. P. Bonifas. *Nat. Mater.*, 12:938, 2013.

[100] J. A. Rogers Y. Sun. *Adv. Mater.*, 19:1897, 2007.

[101] L. Jia K. E. Mathewson K.-I. Jang J. Kim H. Fu X. Huang P. Chava R. Wang-S. Bhole L. Wang Y. J. Na Y. Guan M. Flavin Z. Han Y. Huang J. A. Rogers S. Xu, Y. Zhang. *Science*, 344:70, 2014.

[102] G. Shin C. D. Morgan B. A. Copits H. U. Chung M. Y. Pullen K. N. Noh S. Davidson S. J. Oh J. Yoon K.-I. Jang V. K. Samineni M. Norman J. G. Grajales-Reyes-S. K. Vogt S. S. Sundaram K. M. Wilson J. S. Ha R. Xu T. Pan T.-I. Kim Y. Huang M. C. Montana J. P. Golden M. R. Bruchas R. W. Gereau J. A. Rogers S. I. Park, D. S. Brenner. *Nat. Biotechnol.*, 33:1280, 2015.

[103] R. Ghaffari Y.-S. Kim S. P. Lee L. Xu J. Wu R.-H. Kim J. Song Z. Liu J. Viventi B. de Graff B. Elolampi-M. Mansour M. J. Slepian S. Hwang J. D. Moss-S.-M. Won Y. Huang B. Litt J. A. Rogers D.-H. Kim, N. Lu. *Nat. Mater.*, 10:316, 2011.

[104] R.-H. Kim-P. Elvikis M. Meitl D.-H. Kim J. Wu J. Yoon C.-J. Yu Z. Liu Y. Huang K. Hwang P. Ferreira X. Li K. Choquette J. A. Rogers S.-I. Park, Y. Xiong. *Science*, 325:977, 2009.

[105] H. Maeda-T. Fukushima-T. Aida K. Hata T. Someya T. Sekitani, H. Nakajima. *Nat. Mater.*, 8:494, 2009.

[106] X. Niu-Z. Yu-Q. Pei J. Liang, L. Li. *Nat. Photonics*, 7:817, 2013.

[107] Z. Liu-Q. Pei Z. Yu, X. Niu. *Adv. Mater.*, 23:3989, 2011.

[108] R. S. Carmichael G. J. E. Davidson T. B. Carmichael H. L. Filiatrault, G. C. Porteous. *Adv. Mater.*, 24:2673, 2012.

[109] J. Zhou Y. M. Chen Z. Suo C. H. Yang, B. Chen. *Adv. Mater.*, 28:4480, 2016.

[110] A. P. Gerratt S. de Mulatier S. P. Lacour A. Hirsch, H. O. Michaud. *Adv. Mater.*, 28:4507, 2016.

[111] S. Li S. Robinson M. Totaro L. Beccai B. Mazzolai R. Shepherd C. Larson, B. Peele. *Science*, 351:1071, 2016.

[112] K. J. Chee P. S. Lee J. Wang, C. Yan. *Adv. Mater.*, 27:2876, 2015.

[113] G. M. Whitesides J. N. Lee, C. Park. *Anal. Chem.*, 75:6544, 2003.

[114] Y. Huang R. G. Nuzzo J. A. Rogers A. Carlson, A. M. Bowen. *Adv. Mater.*, 24:5284, 2012.

[115] F. Xiang J. Zhou H. Wang Z. Suo Y. Bai, B. Chen. *Appl. Phys. Lett.*, 105: 151903, 2014.

[116] A. Kitai. *Solid State Luminescence: Theory, Materials and Devices*, 1993.

[117] J. Rossiter A. T. Conn. *IEEE/ASME Trans. Mechatronics*, 17:968, 2012.

[118] R. Baumgartner R. Kaltseis C. Keplinger R. Schwödiauer I. Graz S. Bauer A. Tröls, A. Kogler. *Smart Mater. Struct.*, 22:104012, 2013.

[119] L. Gil M. Mollar B. Marí J. Ibañez, E. Garcia. *Displays*, 28:112, 2007.

[120] R. Revathi T. R. N. Kutty. *Mater. Res. Bull.*, 20:19, 1985.

[121] H. Zhao B. N. Peele C. M. Larson B. C. Mac Murray I. M. Van Meerbeek S. N. Dunham R. F. Shepherd S. S. Robinson, K. W. O'Brien. *Extreme Mech. Lett.*, 5:47, 2015.

APPENDIX B

INTEGRATED SOFT SENSORS AND ELASTOMERIC ACTUATORS FOR TACTILE MACHINES WITH KINESTHETIC SENSE

B.1 Abstract

Human skin contains highly specialized deformation receptors that allow us to intuitively and effortlessly interpret our surroundings. These sensors help us to localize touch and determine the degree of contact pressure. In addition, the innate understanding of our own body posture is also due to these mechanoreceptors. This work demonstrates a synthetic sensory–motor analog that can be 3D printed, using direct ink writing (DIW) onto soft, fluidic elastomer actuators (FEAs). This 3D printing technique uses two inks – one that is an ionically conductive hydrogel and another that is an electrically insulating silicone – which is then patterned and photopolymerized into stretchable capacitive sensors. In this paper, these sensors are used to enable tactile sensing and kinesthetic feedback in a pneumatically actuated haptic device. This capacitive skin enabled the device to detect a compressive force from a finger press of ~2 N, and an internal pressurization of as low as ~10 kPa.

B.2 Introduction

Human development, intelligence, and survival are intimately linked to tactile (i.e. touch and pressure) and kinesthetic (i.e. position and movement) feedback we receive from millions of mechanoreceptors embedded in our skin [122, 123]. These highly specialized receptors are capable of transmitting signals through ionically conducting nerve fibers at rates of up to 70 m s^1 [123]. When these sen-

sors are deformed mechanically – perhaps by compression of the skin or contraction of a muscle – an action potential is transmitted along afferent pathways then processed in the central nervous system [123]. An appropriate response to the input stimulus is then returned along efferent neuronal pathways [123]. This sensory–motor coupling allows us to effortlessly perceive and interact with our environment, enabling the performance of complex tasks such as avoiding furniture in the dark or playing the piano. Due to skin's significant role in learning, tool manipulation, and gross motor coordination, the development of a synthetic analog will enable new methods of feedback control in robotics, medical monitoring, and human–machine interfaces. Wearable [124] and implantable electronics [125] have been developed to integrate with human tissue, which is soft, three-dimensional, and mechanically dynamic.

Along with the development of stretchable electronics, the field of soft robotics has been gaining traction as a result of their ability to (i) interact gently with biological organisms [126, 127], (ii) easily conform to their surroundings [128, 129, 130], and (iii) achieve complex motions using simple modes of actuation [131, 132, 133, 134]. These robots are typically composed of hyperelastic materials (e.g. silicones) with large ultimate strains, $\gamma_{ult} \approx 400\%$–$700\%$, that have embedded networks of pneumatic channels (PneuNets). These pneumatic actuators are powered through inflation, similar to a balloon. A critical limitation of soft robots is the availability of compliant and extensible sensors [135] that can (i) reliably detect external stimuli and internal actuation, (ii) be easily integrated with current manufacturing processes, (iii) function at the high strains encountered throughout actuation, and (iv) tolerate many actuation cycles without delamination.

To address these sensing deficiencies many groups have developed flexible

and stretchable sensors that use changes in resistance [136, 137, 138], capacitance [139, 140, 141], light [142], or resonant frequency [143, 144] to detect deformation. Specifically, for soft robots that undergo large deformations, shape sensing is a critical need for feedback control (communicating with a central computer to ensure a machine task is being completed accurately). Therefore, we focus on sensing techniques using stretchable capacitors due to their high precision and sensitivity over large ranges of strain and pressure [145, 146].

Here we present a highly extensible sensing skin that we integrated with soft, pneumatic actuators via a 3D printing technique called direct ink writing (DIW; Fig. B.1). This skin enables soft machines to sense external stimuli as well as their own shape, thus creating a device that has both tactile and kinesthetic sense. Central to our approach is the development of two viscoelastic fluids—one that is ionically conductive (hydrogel elastomer precursor) and another that is electrically insulating (silicone elastomer precursor). We directly patterned these inks by extruding them in alternating layers through micronozzles of two different diameters, d_{hydr} = 330 μm and d_{sil} = 250 μm, on our custom dual-head 3D printer. The two inks are yield-stress fluids that flow through our print heads at high shear rates and retain their shape after exiting the nozzles due to their viscoelastic properties. After extrusion, we used in-situ photopolymerization of the inks to chemically crosslink them into conductive hydrogels and insulating silicones with large ultimate strains, $\gamma_{sil}^{ult} > 350\%$ and $\gamma_{hydr}^{ult} > 300\%$ (Fig. B.2, B.6). When patterned into alternating conductive and dielectric layers, these composite skins behave as stretchable capacitors, capable of transducing low mechanical stresses and large strains into electrical signals. We printed these stretchable capacitors onto soft, Pneumatically-powered Haptic Displays (PHD; Fig. B.1, B.5) to provide sensory feedback control. We characterized the ability

of the PHD to (i) detect touch (tactile sense), (ii) detect its own actuation (kinesthetic sense), and (iii) integrate these two senses for sensory–motor coupling.

B.3 Experimental Design

We chose to use DIW because it offers material flexibility, rapid design iteration, low cost [147, 148, 149], and facile integration with previously established soft robot fabrication methods (i.e. replica molding [129] and rotational casting [130]). In addition, the rheological properties of many polymeric inks can be modified to enable this printing technique [150, 151, 152]. Specifically, both the shear thinning and yield stress properties of these complex fluids can be adjusted so the inks flow smoothly out of micronozzles and retain their shape after being printed. The shear thinning exponent (n), storage (G) and loss (G) moduli are primarily controlled by the high molecular weight polymer constituents [153].

To tailor the rheology of the silicone elastomer precursor, we prepared blends of high and low molecular weight silicones (60 wt% Nuvasil Loctite 5039, 40 wt% Wacker Semicosil 912) together into a homogeneous melt (details in supplemental information, SI). In this system, the high molecular weight polymer serves to adjust the yield stress, while the low molecular weight one polymerizes into a resilient matrix. We chose silicones because they have very high electrical resistivity (on the order of 10^{13} Ωm), low leakage currents [154], high strain to failure, and high resilience [138, 155].

We chose hydrogels because they can be made highly conductive, transparent, biocompatible, and stretchable [138, 155]. We formulated the hydrogel elastomer precursor analogously to the silicone by combining high molecular weight polyacrylamide (PAAM 5–6 million M_W; 92560, Sigma Aldrich) and acry-

lamide monomer (AAM; Sigma Aldrich) in deionized water and ethylene glycol (EG; Sigma Aldrich). We also used N,N-methylenebisacrylamide (MBA; Sigma Aldrich) as the crosslinking agent and Darocur photoinitiator, ionic liquid (IL; 1-decyl-3-methylimidazolium chloride, Sigma Aldrich) served as the conductive medium. As the hydrogel is optically transparent, we used fluorescently labeled monomer (FOA; Fluorescein O-acrylate, Sigma Aldrich) for visualization of the ink during printing. We found that using 14 wt% AAM, 5.6 wt% PAAM, 0.22 wt% MBA, 0.14 wt% DarocurR 1173, 3.4 wt% IL, 0.1 wt% FOA, 56.2 wt% EG, and 20.3 wt% DI water resulted in the desired rheological and mechanical properties.

We fabricated silicone actuators using soft lithography as this process is simple and allows for rapid design iteration (details in SI). We then printed stretchable capacitors onto these pneumatic actuators as the skin of our PHD (Fig. B.1, S1). First we placed and leveled the prefabricated actuators on the bed of the 3D printer, then loaded the silicone and hydrogel inks into two separate syringes. By alternating layers of polyacrylamide and silicone inks we created planar arrays of capacitive sensors. The inks were exposed to high intensity UV radiation throughout the printing process. Once the capacitive skin was fully printed, no post exposure to UV light was necessary. We chose to overlay these sensors onto the actuators as an intuitive user interface to physically program the PHD; in addition, they enable us to detect the degree of actuation of individual chambers. Alternatively, if kinesthetic sensing is not needed, we can print the sensors anywhere, not necessarily on top of the actuators.

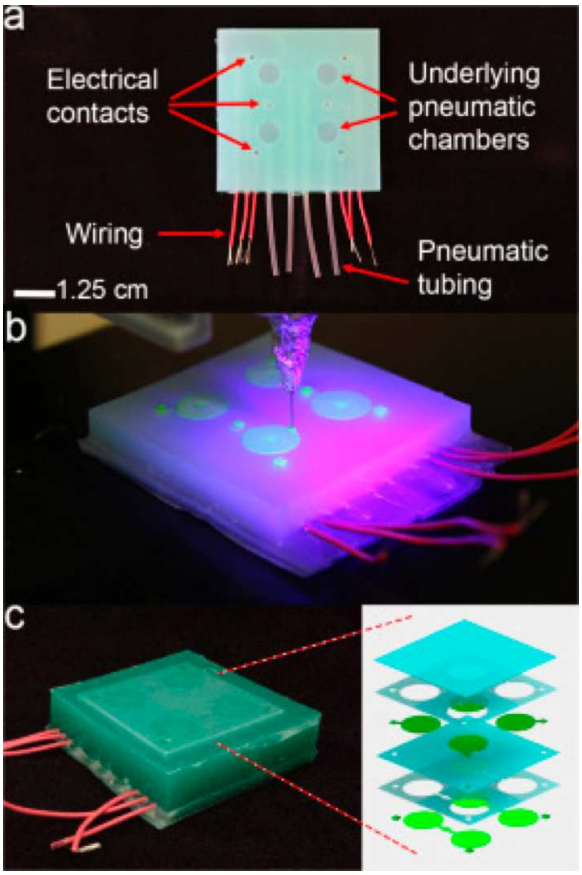

Figure B.1: **Photograph of the pneumatic haptic display.** (A) Image of pneumatic haptic display with wells where electrical contacts will be formed, underlying pneumatic chambers, tubing and electrical wiring. (B) Image of printing stretchable sensors onto pneumatic haptic display. (C) Fully printed sensor on surface of pneumatic haptic display; (inset) Schematic of printed layers of conductive polyacrylamide (green) and insulating silicone (blue).

B.4 Results and Discussion

To be compatible with our pressure inputs (P_{sil} ~ 270 kPa and P_{hydr} ~ 70 kPa) we tuned our materials to have viscosities less than 50 Pa·s at the shear rates for which we were printing (Fig. B.2a). Both inks displayed pronounced shear thinning above a critical shear rate of 0.1 s^{-1}. This behavior indicates that above

these shear rates, the entangled, long-chained polymers are aligning under the applied shear stress and will start to flow smoothly through micronozzles. Using Eq. B.1, we estimated the shear rate experienced by the ink at the nozzle walls during extrusion [155]:

$$\dot{\gamma}_{wall} = \left(\frac{3+b}{4}\right)\frac{4Q}{\pi R^3} \tag{B.1}$$

where b is the inverse of the shear thinning exponent, $Q = v\pi R^2$ is the volumetric flow rate, $v \sim 4$ mm s^{-1} is the print speed, and R is the nozzle radius. We determined the shear thinning exponent from our measured viscometry data to be $nv_{hydr} = 0.287$ and $v_{sil} = 0.496$. We calculated the shear rate experienced by these fluids at the nozzle to be $\dot{\gamma}^{hydr}_{wall} \sim 157$ s^{-1} and $\dot{\gamma}^{sil}_{wall} \sim 160$ s^1. At these shear wall wall rates, the ink viscosities are $v_{hydr} \sim 7$ Pa·s and $v_{sil} \sim 17$ Pa·s. Ink elasticity is an important rheological parameter that can indicate whether ink will retain its printed shape before crosslinking. To determine the elasticity of these inks, we measured the shear elastic modulus (G') and viscous modulus (G'') at a frequency of 1 Hz (Fig. B.2b). The polyacrylamide ink has a plateau elastic modulus of $G_0 \sim 350$ Pa and a yield stress of $\sigma_{hydr} \sim 539$ Pa, while the silicone ink has $G_0 \sim 2250$ Pa and $\sigma_{sil} \sim 22$ Pa. We found that both inks display a solid-like response ($G' > G''$) at low shear stresses, which enables shape retention after extrusion and before being cured under UV illumination.

The skin of the PHD must withstand large strains, yet deform at low stresses. As the mechanical properties of the skin are dominated by the silicone, we measured its tensile properties (Fig. B.2c; details in SI). We also compared our printed material's mechanical properties to that of cast silicone (Fig. B.2c). At 100% strain, the printed and cast silicones have elastic moduli of $E_{print} \sim 73$

kPa and $E_{cast} \sim 109$ kPa, respectively. The lower elastic modulus of the printed silicone may indicate that the high molecular weight polymer remains in a pre-stretched state due to shear alignment from extrusion.

To model $P(\lambda)$, we employ three assumptions: (i) the membrane behaves linear elastically (Fig. B.2c) with an elastic modulus, E, (ii) the undeformed sensor is a circle and upon actuation deforms into a spherical cap with a radius of curvature r, and deflection h, and (iii) the elastomeric membrane is incompressible giving rise to principle stretches of $\lambda_1 = \lambda_2 = \lambda$, $\lambda_3 = \lambda^{-2}$, and principal stresses of $\sigma_1 = \sigma_2 = \sigma$, $_3 = 0$. We first balance the forces from the internal pressure (P) acting on the membrane with the induced reaction forces within it.

$$\begin{aligned} P \cdot (\pi r_0^2) &= T \cdot sin\theta \\ T &= \sigma \cdot (2\pi r_0) \\ sin\theta &= \frac{r_0}{r} \end{aligned} \tag{B.2}$$

where r_0 is the radius of the undeformed sensor, T is the stretching force, t is the nominal thickness of the membrane (see Figure B.10). The pressure can therefore be expressed as follows:

$$P = \frac{2\sigma t}{r} \tag{B.3}$$

Given assumptions 2 and 3 we can relate λ to r, t, and t_0 as follows:

$$\frac{A}{A_0} = \frac{2\pi r h}{\pi r_0^2} = \lambda^2 \quad and \quad \frac{t}{t_0} = \lambda^{-2} \tag{B.4}$$

We now invoke a geometrical argument that relates r to r_0 and h, both of which are measurable quantities.

$$r^2 = r_0^2 + (r - h)^2 \tag{B.5}$$

Combining Eqs. B.2-B.5 with Hooke's law, $\sigma = E(\lambda 1)$, yields the following relation:

$$P(\lambda) = \frac{4t_0 E(\lambda - 1)(\lambda^2 - 1)^{1/2}}{r_0 \lambda^4} \tag{B.6}$$

The circular capacitive sensor is designed such that the in the fully actuated state (i.e., a hemisphere), it covers the underlying chamber completely. The nominal radius of the sensor, r_{C0}, is thus larger than r_0. To model the change in capacitance as accurately as possible, therefore, we bifurcate the capacitance equation into two parts—the first models the outer region that is bounded by r_{C0} and $r_0(C_0)$, and the center portion bounded by $r_0(C_0)$. Our equation for capacitance is:

$$C = C_0 + C_1 \tag{B.7}$$

where

$$C_0 = \epsilon_r \epsilon_0 \frac{\pi(r_{C0}^2 - r_0^2)}{t_{C0}} \tag{B.8}$$

and

$$C_1 = \epsilon_r \epsilon_0 \frac{2\pi r h}{t_c} = \epsilon_r \epsilon_0 pi \frac{r_0^2}{t_{C0}} \lambda^4 \tag{B.9}$$

Combining relations in Eq. B.7 yields the relationship between λ and C:

$$\lambda = \left(\frac{C - C_0}{\epsilon_r \epsilon_0 \pi \frac{r_0^2}{t_{C0}}} \right)^{1/4}. \tag{B.10}$$

Finally, we substitute $\lambda(C)$ in Eq. (10) into Eq. B.6 to derive $C(P)$. We solve for $C(P)$ numerically in MATLAB to obtain the plot shown in Fig. B.3a, left. Table B.1 lists the parameters used in the model. We observe that the predicted relationship between C and P is in general agreement with the measured values, confirming that our deformable capacitor follow $C \sim Ad^{-1}$ behavior. The slight deviation between the predicted and measured values at pressures >25 kPa indicates that our bifurcation scheme could be further refined.

Next, we demonstrated the ability of the PHD to transduce external touch into an electrical signal by repeatedly pressing on a single sensor cell 99 times (Fig. B.3a, right, Fig. B.7). The average force delivered during the press of a sensor cell is approximately 2 N (SI text), this force causes a detectable $C \sim 1$ pF. As our goal was not to precisely measure the force a finger applies but to demonstrate the sensitivity to touch of the PHD, we used our own fingers instead of a machine; consequently there is variation in the measured capacitance between the peaks.

Additionally, using a pressurized air dispensing system, we actuated a single chamber of our pneumatic display while measuring the change in capacitance (Fig. B.3b,c). We applied incremental pressures of air to the chamber, we then released the pressure and allowed it to deflate and repeated this cycle (Fig. B.3c). We only tested up to 38 kPa, above that pressure we start to observe deformation of the hydrogel electrode layers. No discernible capacitance change was

observed until at least $P \sim 10$ kPa was delivered to the chamber (Fig. B.3b,c). Since we were inflating and deflating manually, the time for each actuation varied, thus the peak widths vary. The shapes of the peaks continue to evolve after initial pressurization due to the viscoelastic nature of the materials.

To demonstrate our printed sensor array's ability to encode and read haptic information, we programmed a five-digit sequence into the PHD (SI text). We pressed on the individual capacitive buttons in an arbitrary sequence, sending a signal to an off-board microcontroller's memory (Arduino Mega 2560). The microcontroller then played back the recorded sequence through pneumatic actuation of the individual chambers (Fig. B.4; supplemental video, SV1). We numbered the sensors one through four, and then punched in the code 2-4-3-2-1 (Fig. B.4a). The PHD then individually inflated each underlying chamber associated with the sensor input (Fig. B.4b). The PHD detected the ΔC of both the input stimulus (tactile sense) and output actuation (kinesthetic sense; Fig. B.4c). We note that the peaks from the input are sharp and output are broad due to the duration of the different events.

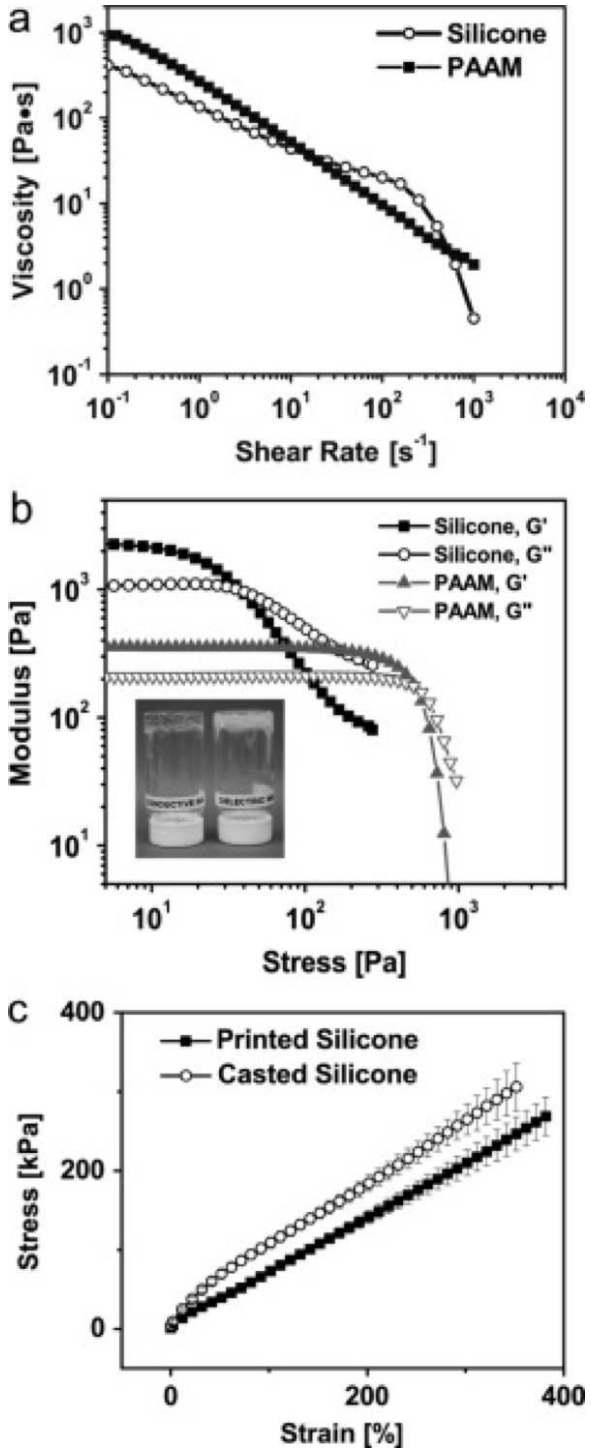

Figure B.2: **Rheological properties of the hydrogel sensor ink.** (A) Viscometry and (B) oscillatory rheology data for insulating silicone and conducting polyacrylamide (PAAM) inks; (inset) upturned vials of each ink demonstrate their elasticity. (C) Tensile data of 3D printed and cast silicone samples.

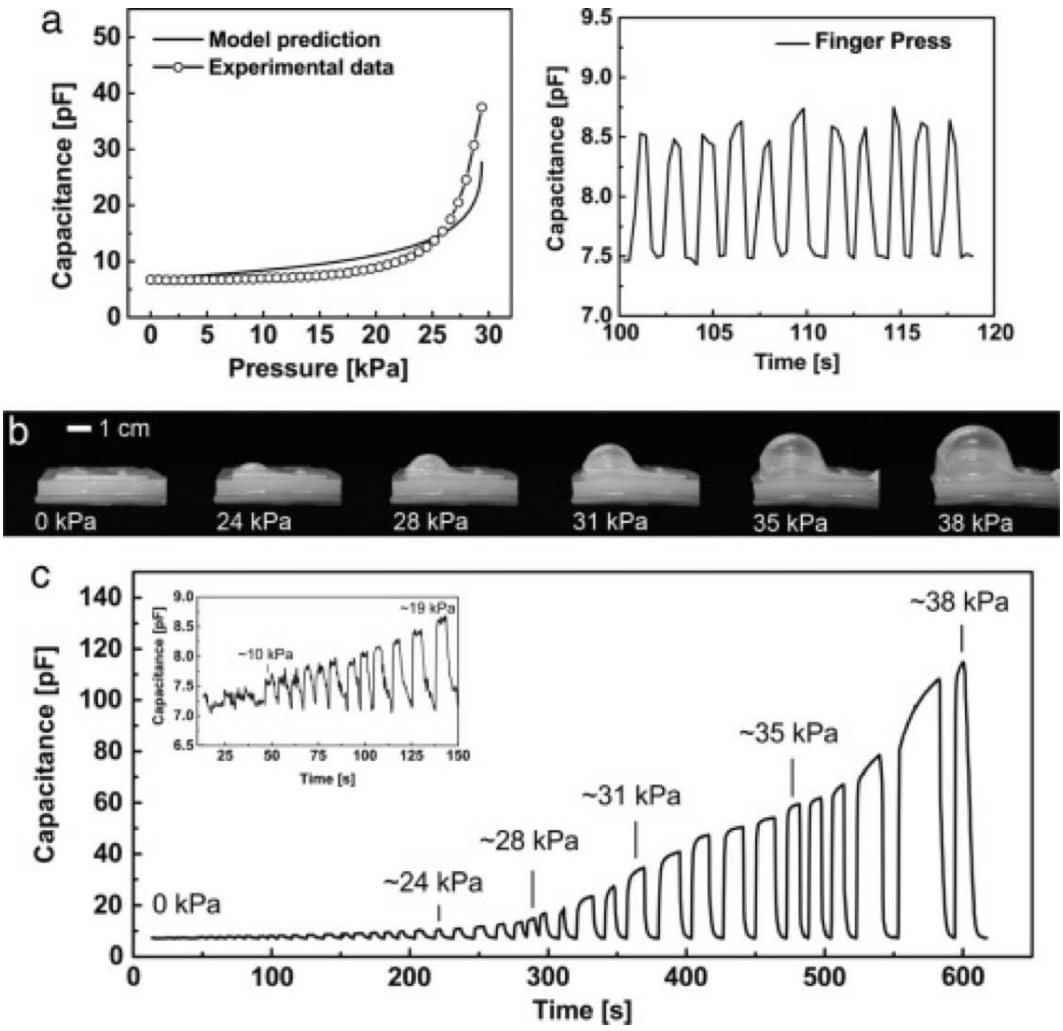

Figure B.3: **Rheological properties of the hydrogel ink.** (a) Left, the measured (circles) and theoretical (line) capacitance as a function of inflation pressure. Right, repeatability of capacitor to sense stimulus when pressed by a finger. (b) Left to right, images of actuation at different applied pressures. (c) Capacitance dependence on inflation and deflation of actuator at increasing pressures; (inset) lower capacitance range magnified.

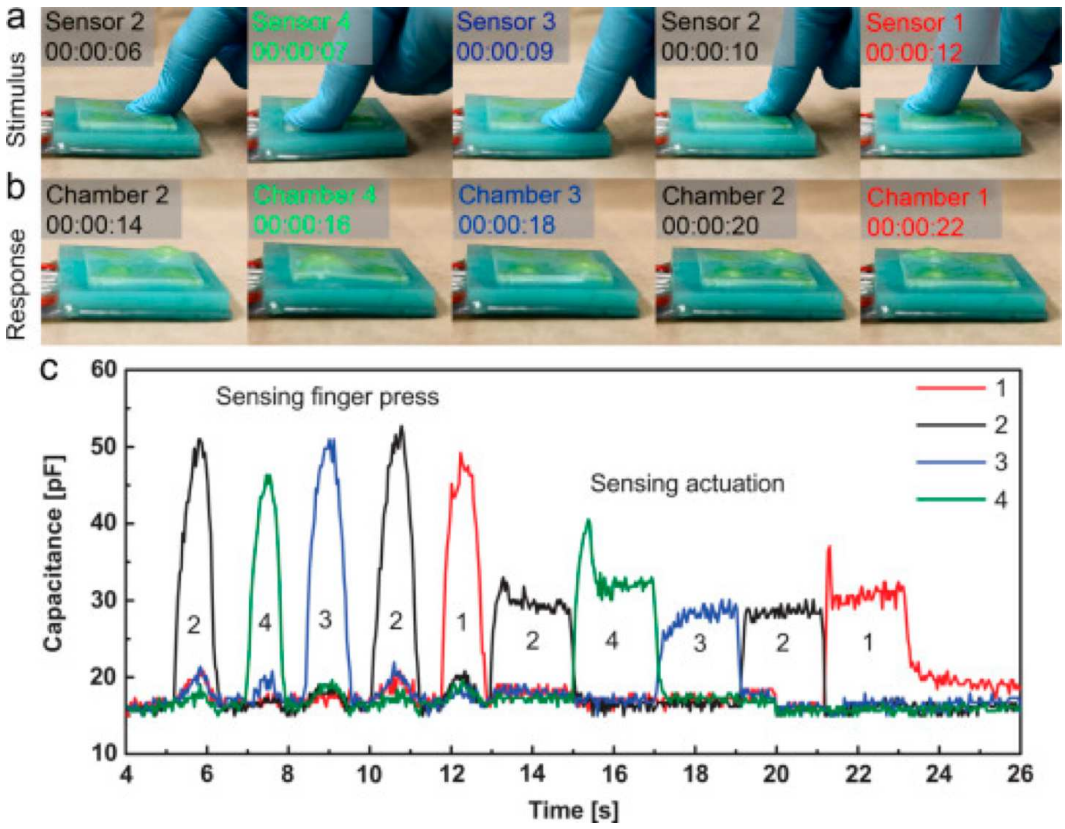

Figure B.4: **Capacitive response to touch.** (a) Left to right, digital images of inputting a code (2-4-3-2-1) using finger to push on the sensor. (b) Left to right, pneumatic haptic display playing back the same code (2-4-3-2-1). (c) Capacitance change of sensor as the code is being input, and then played back through pneumatic actuation. Please see SV1 for video of programming and display sequence.

Table B.1: Model parameters

Symbol	Meaning	Value
P	Internal Pressure	-
λ	Stretch	-
σ	Stress	-
r	Radius	-
t	Thickness	-
h	Height	-
r_0	Chamber radius	4.0 mm
t_0	Initial thickness	3.7 mm
E	Young's modulus	68.9 kPa
C	Capacitance	-
r_{C0}	Initial sensor radius	6.0 mm
t_c	Sensor thickness	-
t_{c0}	Initial Sensor thickness	0.33 mm
ϵ_r	Relative permittivity	2.2
ϵ_0	Dielectric constant	$8.854\times10^{-12} Fm^{-1}$

B.5 Conclusion

In summary, we have developed an inexpensive, hyperelastic, and printable skin for the sensory–motor coupling of soft machines. By tuning the rheological properties of elastomer precursors we formulated viscoelastic inks, which we patterned directly onto the actuators of our PHD. This capacitive skin enabled the PHD to detect a compressive force of ~2 N, and an internal pressurization

of as low as ~10 kPa. As far as we know this is the first demonstration of a completely soft, feedback controlled haptic interface. As the majority of the mating surface between the skin and actuators is silicone, the device exhibited excellent adhesion and no delamination occurred even when high pressures (up to ~65.5 kPa) were applied to the actuating chambers. At these pressures, however, the inextensible sealing layer delaminated from the bottom of the PHD; this issue is general to PneuNets operated at high pressure.

While the hydrogels used here have some amount of solvent and are thus somewhat sensitive to environmental conditions, solvent-free systems, such as the polyacrylic acid ones recently demonstrated [155], could be used to mitigate this issue. While this is a 2D array of capacitors, 3D systems are possible with more complicated CAD design. It is also possible to miniaturize these capacitors by increasing the dielectric constant of the insulating material through the addition of fillers and the use of smaller nozzle diameters for decreased layer thickness. With these two steps we can more accurately replicate the natural ability of biological skin to localize touch sensations. The reliable, low cost, and flexible design space using DIW of tactile and kinesthetic sensors will improve robotic technologies – which are normally confined to perform repetitive tasks in structured environments (i.e. mobile industry) – by allowing humans to work more closely with machines in applications such as search and rescue and domestic care. This same sensor technology could also improve the quality of life for amputees by enabling intuitive use and automatic adjustment of prosthetic devices.

B.6 Supplementary Information

Material System. The silicone ink was formed by mixing and degassing 60 wt% Nuvasil® Loctite 5039 and 40 wt% Wacker ® Semicosil 912 in a Thinky ARM-310 at 2000 rpm for 120s. The UV catalyst (Wacker ® Elastosil CAT UV) for Semicosil 912 was added at a 1:10 ratio prior to mixing. Due to the secondary moisture cure of Loctite 5039, this ink was used immediately. The polyacrylamide ink was formed by first mixing deionized water, ethylene glycol and acrylamide monomer (AAM) at room temperature. These constituents were magnetically stirred until the AAM was fully dissolved; at that point we slowly added polyacrylamide to the solution. After the solution was homogeneous, we added N,N'-methylenebisacrylamide, Darocure® 1173 photoinitiator, 1-decyl-3-methylimidazolium chloride ionic liquid, and Fluorescein O-acrylate. All chemicals were used as received.

Rheological, Mechanical, and Electrical Measurements. Oscillatory rheometry was performed on both ink solutions using a cone (25mm, °2) and plate geometry at a frequency of 1 Hz and an oscillatory stress from 0 to 900 Pa to determine the elastic modulus (G'), loss modulus (G''), and yield stress (σ_γ) of the printable ink. Viscometry was performed on both inks as well, from shear rates of 0 to 1000 s^{-1}. All data were taken using cone and plate geometry with 0.5 ml of material on a TA Instruments Discovery Hybrid Rheometer DHR3 rotational shear rheometer. We performed uniaxial tensile tests on a Z010 Zwick Roell using a 20 N load cell at a strain rate of 3.33 mm s^{-1}. We tested at least six repetitive samples of both printed and cast silicone. After printing and casting large rectangular geometries of silicone elastomer precursor, we used a razor blade to cut out six straight, rectangular test samples with approximate dimensions of 40×7×0.6 mm. We measured the electrical performance of the ionic liquid con-

taining hydrogel using a Cascade CP06 Four Point Probe with four in-line probe tips and a Keithley 2400 Source-Meter. We prepared two thin (25×25×1.3 mm) film specimens of the conducting hydrogel. The four-point probe system was configured for single resistance measurements by sourcing 0.001 A of current and measuring voltage. We measured voltage five times in three locations of each film.Using a probe spacing of s = 1.59 mm and an average film thickness of t = 1.3 mm, we calculated the thickness correction factor, a, for our measurements using the following equation [122, 123]:

$$a = \frac{1}{1 + \frac{0.52632}{\left(t/s\right)^{1.9}}} \quad for \quad t/s > 0.5 \tag{B.11}$$

We then calculated the conductivity by taking the inverse of the following general expression for resistivity:

$$\rho = sa2\pi\left(\frac{V}{I}\right) \tag{B.12}$$

We calculated a conductivity of $\sigma \sim 10.8$ mS m^{-1} for the ionic liquid containing hydrogel.

Direct-Write Assembly of Sensors. The ink was loaded into a syringe with an attached stainless steel dispensing tip in place. We created planar arrays of sensors by layering the polyacrylamide and silicone inks. Once the sensors were patterned, we printed an encapsulating layer of silicone ink. While patterning the ink materials, we exposed them to 5 mW cm^{-2} using a UV lamp (Omnicure ® S1500; Excelitas) with a wavelength range, λ = 320 - 500 nm. The part was fully cured after printing and not post-printing curing step was needed.

PHD Actuator Fabrication. The actuators of the PHD are composed of a highly

resilient silicone elastomer (Ecoflex 00-30; Smooth-On, Inc.), with an elastic modulus of ~ 40 kPa at 100% strain and ultimate strain of $\gamma^{ult}_{ecoflex}$ >900%. We fabricated these devices using soft lithography from 3D printed molds. We designed a mold for the pneumatic actuators and then fabricated them in Rigid Opaque Blue material (Figure B.8, VeroBlue RGD840; Stratasys, Inc.) using a 3D printer (Objet24; Stratasys, Inc.). We blended green pigment (Silc Pig ®; Smooth-On, Inc.) into a matrix of uncured Ecoflex 00-30, then degassed the polymeric melt and poured it into the mold. We cured the Ecoflex for 60 min at 80 °C. We removed this part from the mold and layered it onto an inextensible composite sheet of Ecoflex and carbon fiber veil (Fibre-Glast, Inc.). We glued the extensible layer to the inextensible one using a thin layer of Ecoflex precursor. Next, we inserted electrical wires (1 mm outer diameter) and pneumatic tubing (1 mm inner diameter) into their respective channels (Figure B.1a). Finally we filled the well surrounding the electrical wiring with the conductive polyacrylamide ink. This ensured excellent contact between the electronic (wires) and ionic (polyacrylamide hydrogel) conductors. This also allowed seamless electrical contact to the capacitive sensors, which would be printed on the surface of this Ecoflex part. We chose a haptic display design with four actuators because it yields 16 unique combinations with a simple on-off motif for tactile communication yet is also a compact design. This specific geometry considered hand and finger ergonomics, as well as integration of pneumatic feed tubes and electrical wiring.

PHD Controls. We connected the electrical wiring of our haptic device to the off-board microcontroller (AT Mega 2560): the ground plane of each sensor to the ground of the microcontroller and each of the four sensor channels to four separate digital input ports on the microcontroller (Figure B.9). The outputs of the four sensors were read and processed by the Arduino's Capacitive

Sensing Library. This library measures capacitance by counting the amount of time it takes for the digital pin to change states (HIGH to LOW, or LOW to HIGH voltage) and outputting the corresponding digital timestamp. This digital timestamp is proportional to the capacitance via the time constant $\tau = RC$, where R is resistance and C is capacitance. Since our capacitance measurements were derived from timestamps, it was necessary to calibrate the measurements. Though this method was not the most accurate capacitive measurement option, it allowed us to analyze the capacitance values of all four sensors simultaneously and in real-time. We wrote a simple program to continuously monitor the capacitance values of each of the sensors. When the minimum threshold value for capacitance (25 pF) was met by a sensor, we considered this a 'button-press' and the microcontroller stored that sensor's identification (ID; 1 through 4) into a First-In-First-Actuated (FIFA) queue of length five. After five unique button presses, our control algorithm switched from 'sensing' mode to 'actuation' mode. Using four separate digital output ports, we connected the microcontroller to four solenoid valves (Parker X-Valve). These valves controlled the pressure inside the four actuation chambers via the pneumatic tubing. The pressure in each chamber was increased by 35 kPa with a control signal of HIGH and reduced back to atmospheric pressure with a control signal of LOW. During 'actuation' mode, the microcontroller was set to transmit the HIGH signal on each of the output channels corresponding to the IDs stored in the FIFA queue (generated during 'sensing' mode). Each output signal of HIGH lasted for duration of 2 seconds before moving on to the next ID in the queue. Upon completion of the final actuation in the sequence, the microcontroller would revert back to 'sensing' mode to receive a new sequence of five button presses. The average response time of each of these chambers was approximately 120 ms. This value

is a combination of the minimum response time of the solenoid valves we used plus the average time it takes for the pressure of the chamber to increase to ~ 28 kPa.

Average Force of Finger Press. We pressed on a precision balance (Mettler Toledo MS403S) and recorded the amount of force reported. We repeated this ten times over four trials and then calculated the average applied force by the finger used in the experiments to be ~ 2 N.

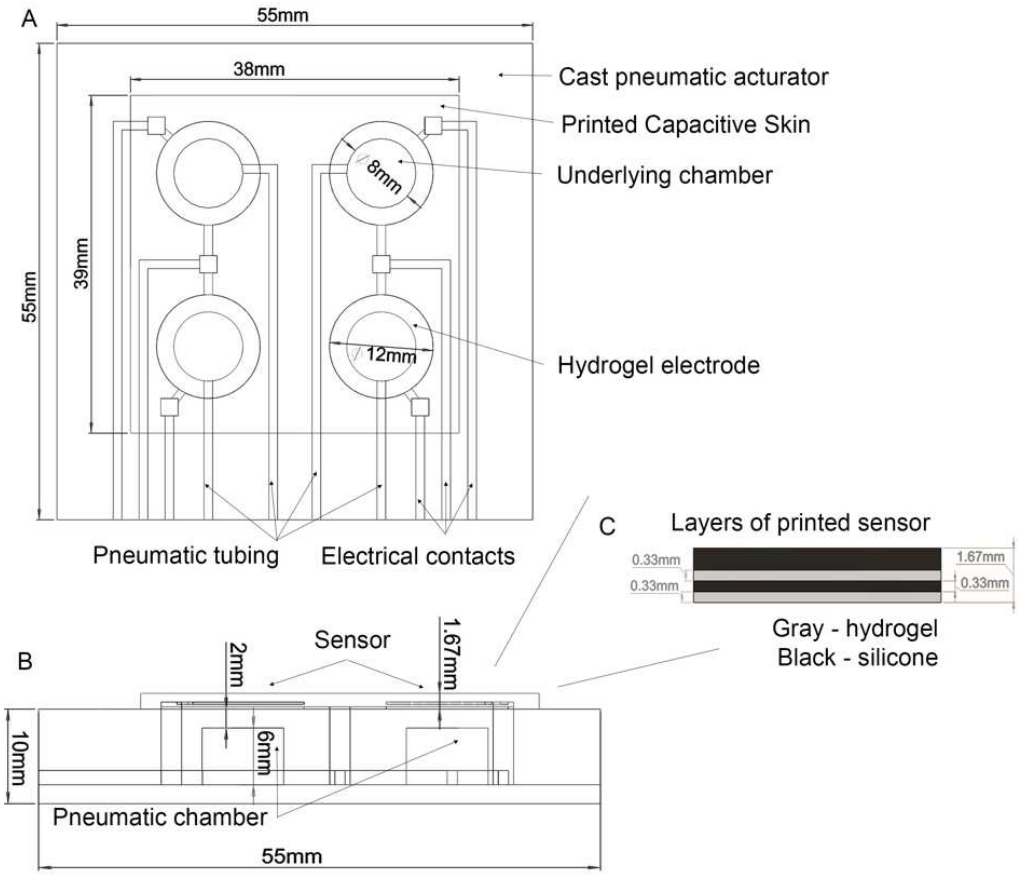

Figure B.5: **PHD Device Schematic.** (a) Top down schematic of PHD with overlaying capacitive skin. The four underlying pneumatic chambers are visible with the four overlaying sensors. Pneumatic and electrical lines are also shown. (b) Side view the PHD with overlaying capacitive skin. Two pneumatic chambers are shown with two overlaying sensors. (c) Expanded view of printed sensor, with printed electrodes in gray and printed insulator in black. The top layer of silicone is slightly thicker to ensure good encapsulation of sensors.

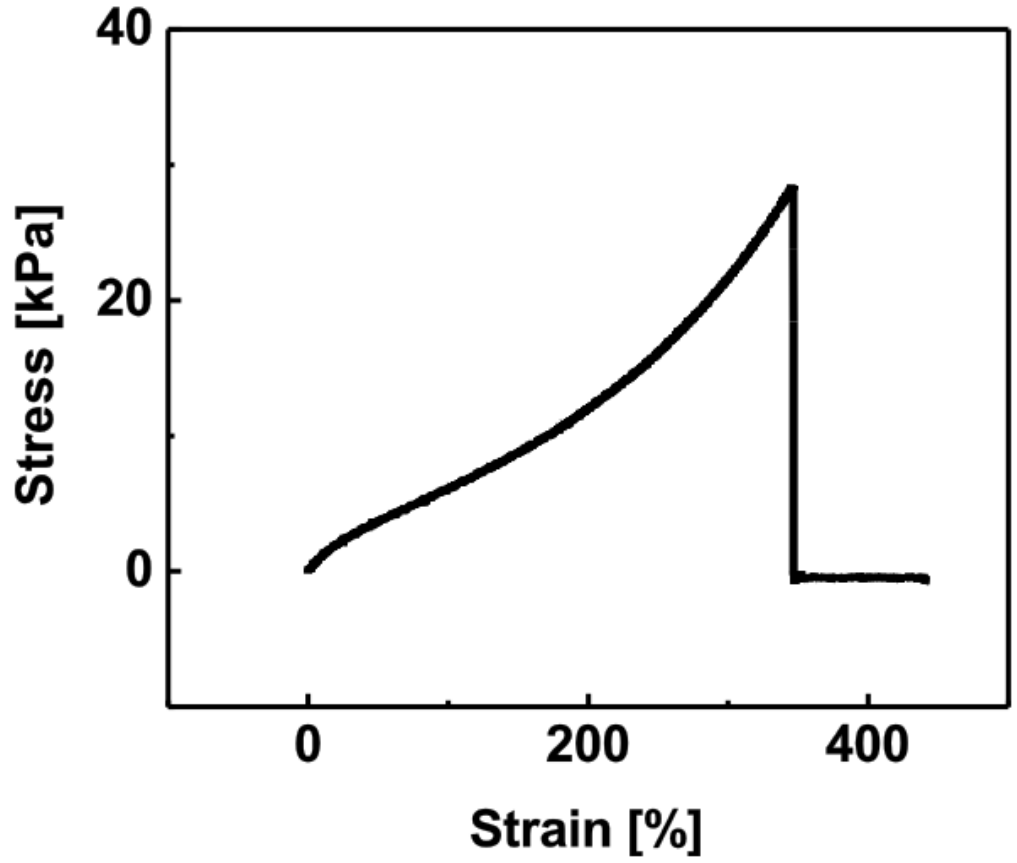

Figure B.6: **Uniaxial tensile test of conductive, polyacrylamide hydrogel.**

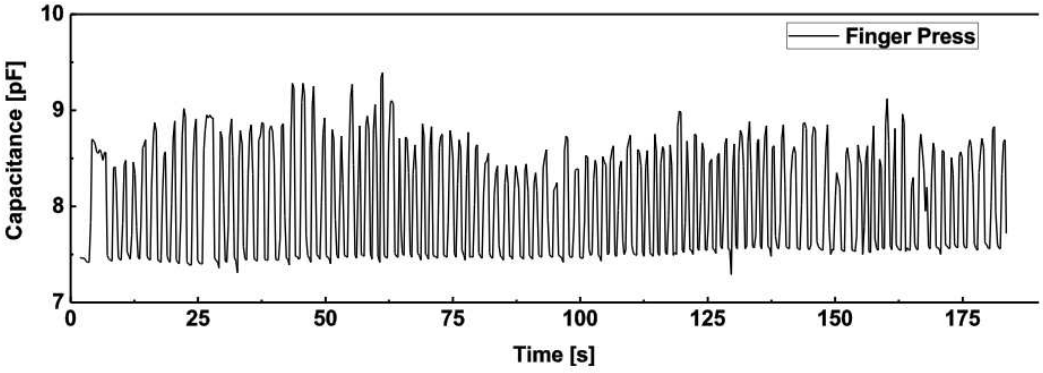

Figure B.7: **99 repetitive presses of sensor with finger.**

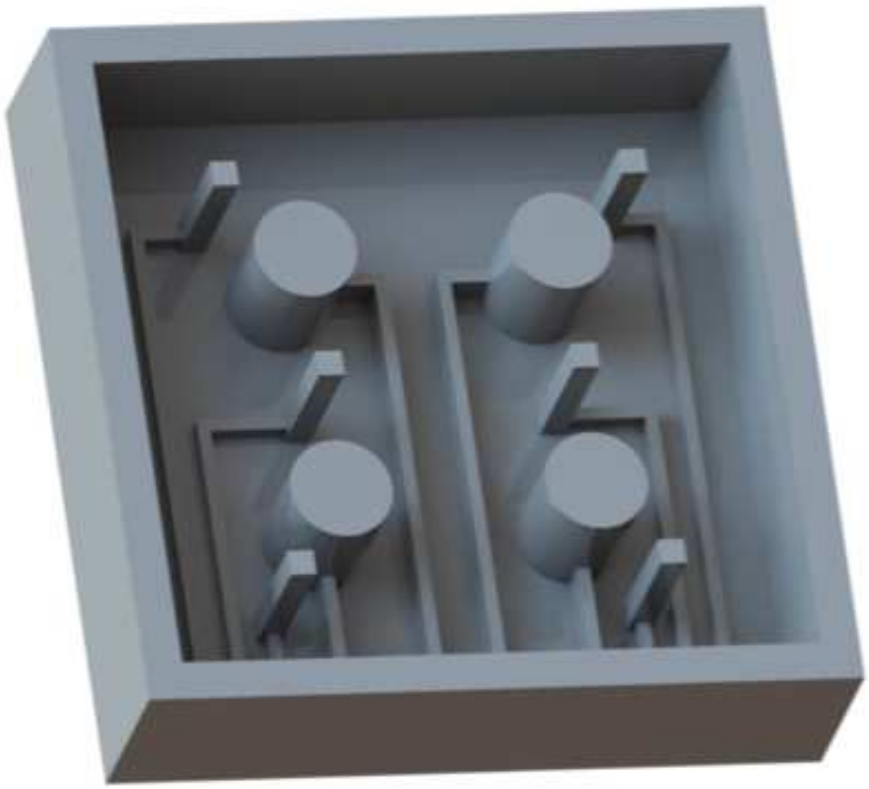

Figure B.8: **Soft lithographic mold for pneumatic haptic display.**

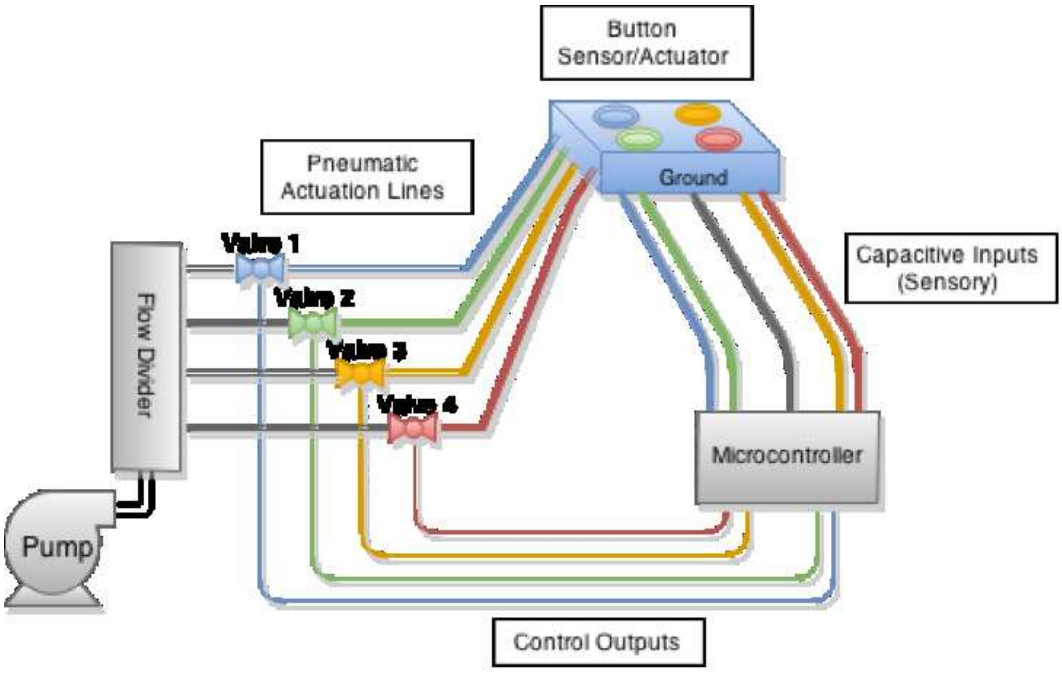

Figure B.9: **Offboard microcontroller configuration.**

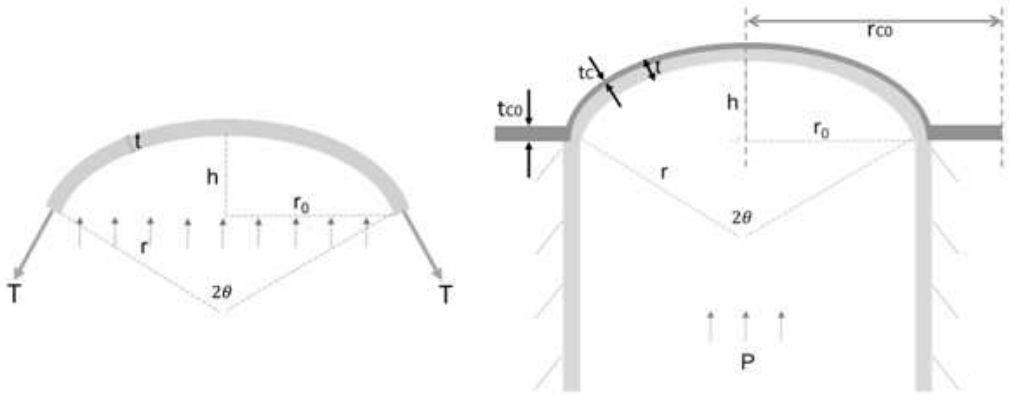

Figure B.10: **Free body diagram of actuator-sensor pair during pneumatic pressurization.**

REFERENCES

[122] F. Iida R. Pfeifer, M. Lungarella. *Commun. ACM*, 55:76, 2012.

[123] A.C. Guyton. *Textbook of Medical Physiology*, 1981.

[124] D.E. De Rossi F. Carpi G. Frediani, D. Mazzei. *Front. Bioeng. Biotechnol.*, 2: 31, 2014.

[125] N. Lu J.A. Rogers D.-H. Kim, R. Ghaffari. *Annu. Rev. Biomed. Eng.*, 14: 113–128, 2012.

[126] Zheng Wang L.F. Nicolini B. Mosadegh G.M. Whitesides C.J. Walsh P. Polygerinos, S. Lyne. *IEEE/RSJ International Conference on Intelligent Robots and Systems, IROS 2013, IEEE, 2013*, page 1512–1517, 2013.

[127] C.R. Fish L. Jin R.F. Shepherd R.M.D. Nunes Z. Suo G.M. Whitesides R.V. Martinez, J.L. Branch. *Adv. Mater.*, 25:205–212, 2012.

[128] R.F. Shepherd X. Chen G.M. Whitesides F. Ilievski, A.D. Mazzeo. *Angew. Chem. Int. Ed.*, 50:1890–1895, 2011.

[129] W. Choi S.A. Morin A.A. Stokes A.D. Mazzeo X. Chen M. Wang G.M. Whitesides R.F. Shepherd, F. Ilievski. *Proc. Natl. Acad. Sci.*, 108: 20400–20403, 2011.

[130] A. Elsamadisi R. Shepherd H. Zhao, Y. Li. *Extreme Mech. Lett.*, 3:89–104, 2015.

[131] R. Fuhrer R.N. Grass W.J. Stark C.M. Schumacher, M. Loepfe. *RSC Adv.*, 4:16039, 2014.

[132] B. Mosadegh K.C. Galloway M. Wehner M. Karpelson R.J. Wood G.M. Whitesides M.T. Tolley, R.F. Shepherd. *Soft Robot.*, 1:213–223, 2014.

[133] D. Rus A.D. Marchese, C.D. Onal. *Soft Robot.*, 1:75–87, 2014.

[134] C. Keplinger W. Sophia R.F. Shepherd U. Gupta J. Shim K. Bertoldi C.J. Walsh G.M. Whitesides B. Mosadegh, P. Polygerinos. *Adv. Funct. Mater.*, 24:2163–2170, 2014.

[135] M.T. Tolley D. Rus. *Nature*, 521:467–475, 2015.

[136] R.J. Wood Yong-Lae Park, Bor-Rong Chen. *IEEE Sens. J.*, 12:2711–2718, 2012.

[137] R.L. Truby Y. Mengüç D.B. Kolesky R.J. Wood J.A. Lewis J.T. Muth, D.M. Vogt. *Adv. Mater.*, 26:6307–6312, 2014.

[138] G.M. Whitesides Z. Suo J.-Y. Sun, C. Keplinger. *Adv. Mater.*, 26:7608–7614, 2014.

[139] D.M. Vogt Y. Mengüç A. Campo A.D. Valentine C.J. Walsh J.A. Lewis A. Frutiger, J.T. Muth. *Adv. Mater.*, 27:2440–2446, 2015.

[140] J.B.H. Tok Z. Bao M. Ramuz, B.C.K. Tee. *Adv. Mater.*, 24:3223–3227, 2012.

[141] C. Kim M. Hashimoto B.J. Wiley D. Ham G.M. Whitesides M. Kubo, X. Li. *Adv. Mater.*, 22:2749–2752, 2010.

[142] J.-H. So G. Lazzi M.D. Dickey M. Rashed Khan, G.J. Hayes. *Appl. Phys. Lett.*, 99:013501, 2011.

[143] S. Laflamme-G. Kofod M. Kollosche, H. Stoyanov. *J. Mater. Chem.*, 21: 8292–8294, 2011.

[144] S.W. Yelich W.Y. Du. *Sens. Transducers*, page 1–25, 2008.

[145] R.F. Shepherd J.E. Smay, G.M. Gratson. *Adv. Mater.*, 14:1279–1283, 2002.

[146] S.R. White-J.A. Lewis D. Therriault, R.F. Shepherd. *Adv. Mater.*, 17: 395–399, 2005.

[147] J. Yoshikawa-R.F. Shepherd B.Y. Ahn J.A. Lewis J.C. Conrad, S.R. Ferreira. *Curr. Opin. Colloid Interface Sci.*, 16:71–79, 2011.

[148] J.N. Hanson R.G. Nuzzo P. Wiltzius J.A. Lewis R.A. Barry III, R.F. Shepherd. *Adv. Mater.*, 21:2407–2410, 2009.

[149] R.F. Shepherd M.U. Gillette J.A. Lewis R.G. Nuzzo J.N. Hanson Shepherd, S.T. Parker. *Adv. Funct. Mater.*, 21:47–54, 2010.

[150] J.A. Lewis. *Adv. Funct. Mater.*, 16:2193–2204, 2006.

[151] J. Hitzbleck J. Krause T. Kridl S. Nowak E. Orselli X. Quan D. Schapeler W. Sutherland J. Wagner J. Biggs, K. Danielmeier. *Angew. Chem. Int. Ed.*, 52:9409–9421, 2013.

[152] Q. Pei P. Brochu. *Macromol. Rapid Commun.*, 31:10–36, 2010.

[153] C.C. Foo P. Rothemund G.M. Whitesides Z. Suo C. Keplinger, J.-Y. Sun. *Science*, 341:984–987, 2013.

[154] M.-C. Heuzey J. Bruneaux, D. Therriault. *J. Micromech. Microeng.*, 18: 115020, 2008.

[155] C.H. Yang J.H. Yang J. Zhou Y.M. Chen Z. Suo B. Chen, J.J. Lu. *Appl. Mater. Interfaces*, 6:7840–7845, 2014.